7-9-2008

Investigation of particle identification methods for the analysis of the photoproduction of neutral kaons on a liquid deuterium target

Brian Beckford
Florida International University

FLORIDA INTERNATIONAL UNIVERSITY

Miami, Florida

INVESTIGATION OF PARTICLE IDENTIFICATION METHODS FOR THE

ANALYSIS OF THE PHOTOPRODUCTION OF NEUTRAL KAONS ON A

LIQUID DEUTERIUM TARGET

A thesis submitted in partial fulfillment of the

requirements for the degree of

MASTER OF SCIENCE

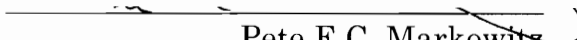in

PHYSICS

by

Brian Beckford

2008

To: Dean Kenneth Furton
   College of Arts and Sciences

This thesis, written by Brian Beckford, and entitled Investigation of Particle Identification Methods for the Analysis of the Photoproduction of Neutral Kaons on a Liquid Deuterium Target, having been approved in respect to the style and intellectual content, is referred to you for judgment.
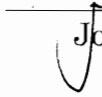
We have read this thesis and recommend that it be approved.

_____
Brian Raue

_____
Pete E.C. Markowitz

_____
Joerg Reinhold, Major Professor

Date of Defense: July 9, 2008

The thesis of Brian Beckford is approved.

_____
Dean Kenneth Furton
College of Arts and Sciences

_____
Dean George Walker
University Graduate School

Florida International University, 2008

DEDICATION

For my mother, brother, and all who search for his or her true self. The way is long and the road narrow, tread on

ACKNOWLEDGMENTS

I would like to express my everlasting appreciation and devotion to my mother, Millicent Beckford, who has been a constan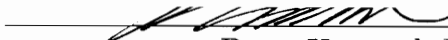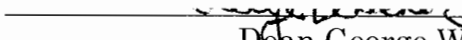t pillar of support through any endeavor I have chosen to pursue. I am the person I am today, only because of her patience and her strong will to forge me into the best possible person that I can be. If I am the sword, then she is the talented sword smith, who tirelessly hammers away.

Also, I thank my brother, who since the age of five, has taken the role of a father to me and has never wavered in his commitment to this role.

I have the highest thanks and admiration for Dr. Joerg Reinhold. He took a chance of inviting me into his lab and has taken an active role in the furthering of my education, by always being available, approachable and infinitely patient. He has pushed me to be self-sufficient and to constantly move forward. It is through witnessing his vigorous work ethic that I am constantly motivated. I thank him for his enduring confidence, re-assurance and allowing me the freedom to be who I am.

My sincere gratitude goes to the committee members for their guidance and support. You have been an inspiration in the decisions I have made about my academic pursuits.

I would like to express my gratefulness to the faculty and students of the Tohoku University experimental nuclear group, for the opportunity to

conduct research along with them as a group member and for igniting a deeper passion for science.

To Luis Lebolo, professors, and friends that helped me along my way, thank you all. Lastly, to my dear friend Alejandro de la Puente, for your infinite patience, for your daily guidance, for listening to my ramblings, for never stop believing in my potential, and for truly being a friend, you have my thanks.

ABSTRACT OF THE THESIS

INVESTIGATION OF PARTICLE IDENTIFICATION METHODS FOR THE

ANALYSIS OF THE PHOTOPRODUCTION OF NEUTRAL KAONS ON A

LIQUID DEUTERIUM TARGET

by

Brian Beckford

Florida International University, 2008

Miami, Florida

Professor Joerg Reinhold, Major Professor

The Photoproduction of neutral kaons off a deuteron target has been investigated at the Tohoku University Laboratory of Nuclear Science. The PID methods investigated incorporated a combination of momentum, velocity ($\beta=v/c$), and energy deposition per unit length (dE/dx) measurements. The analysis demonstrates that energy deposition and time of flight are exceedingly useful. A higher signal to background ratio was achieved for hard cuts in combination. A probabilistic likelihood estimation approach (LE) as a method for PID was also explored. The probability of a particle being correctly identified by this LE method and the preliminary results denote the need for highly precise limitations on the distributions from which the parameters would be extracted. It was confirmed that these PID are applicable approaches to properly identify pions for the analysis of this

experiment. However, the background evident in the mass spectra points to the need for a higher level of proton identification.

TABLE OF CONTENTS

LIST OF TABLES

LIST OF ACRONYMS

ACRONYM

TOF .... Time of Flight

NKS2 .... Neutral Kaon Spectrometer 2

PID .... Particle Identification

LE .... Likelihood Estimation

LNS .... Laboratory of Nuclear Science

CDC .... Cylindrical Drift Chamber

SDC .... Straw type Drift Chamber

OH .... Outer Hodoscope

IH .... Inner Hodoscope

EV .... Electron Veto

STB .... STretcher Booster ring

LINAC .... LINear ACcelerator

QED .... Quantum Electrodynamics

QCD .... Quantum Chromodynamics

1.   INTRODUCTION

1.1   Historical Background

As the understanding of the structure of matter progressed, it was soon realized that what was once believed to be fundamental bodies, as first proposed by Greek philosophers, was not truly so. These objects were found to have an internal structure composed of what was then named as protons, neutrons, and the electrons, the constituents of the atom. The proton and neutron are commonly referred to as nucleons. This lead to an attempt to relate what was known about planetary motion to the motion of these particles within the atom.

Classical physics was unable to fully describe their motion without pitfalls, which prompted the likes of Heisenberg, Dirac, and Schrödinger to formulate Quantum Mechanics as a theoretical solution to resolve the inconsistencies.   Richard Feynman furthered the understanding of the fundamental forces with the formulation of Quantum Electrodynamics (QED). The foundation provided in QED was refined to extend the concept of quantization, and thus was born Quantum Chromodynamics (QCD).

Scientists are always driven by questions, the next question that was asked was, what accounts for the nucleons being held together, and what underlying forces govern their interaction? These are some of the main inquires that are studied in the field of nuclear physics. The standard model

1

is the presently accepted theory that explains the observed behavior of all known particles.

1.2 The Standard Model and Quarks

Quantum Chromodynamics (QCD) is the currently accepted theory that describes the interactions of quarks and gluons, and should ultimately provide an understanding how fundamental particles interact. Physicist Murray Gell-Man first introduced quarks in 1964[1]. Richard Feynman furthered our understanding with the introduction of the parton model in 1968[2]. Partons can be thought of as Lorentz boosted quarks and gluons. The usefulness and success of the parton model is found in the primary difference between the nucleons and their constituents. The nucleons are considered to be non-relativistic, but are composed of relativistic point-like particles [3]. The model, more importantly provides unambiguous predictions.

Fundamental matter particles called fermions, which carry a spin of ½, include the quarks and leptons. They are grouped as shown in Table 1. These particles are considered to be point-like having no internal structure. Each particle q was found to also have an antiparticle with an opposite sign in their quantum numbers denoted as $\bar{q}$.

Table 1: Summary of quarks and leptons [4]

Quarks					
Color = (red, green, & blue) & Spin= ½					
Flavor	Mass (MeV)	Charge	Flavor	Mass (MeV)	Charge
u	3	+2/3	d	6	-1/3
c	125	+2/3	s	100	-1/3
t	1742	+2/3	b	4200	-1/3
Leptons (Spin =½)					
Flavor	Mass (MeV)	Charge	Flavor	Mass (MeV)	Charge
e	.510998	-1	ν_e	<.0001	0
μ	105.658	-1	ν_μ	<.2	0
τ	1776.99	-1	ν_τ	<.2	0

All matter formed from quarks is defined as hadrons and is held together by the strong force. Hadrons can be subdivided into either baryons or mesons. Baryons are formed by the combination of three quarks, resulting in a "white" or color neutral particle, due to the additional color property of quarks. Nucleons are the lowest mass baryons, where the proton is a

combination of (*uud*) and the neutron (*udd*). Quark and anti-quark pairs form mesons, which at the nuclear level is the mediator of the strong nuclear force. The lightest meson is the pion ($u\bar{d}$) [4].

1.3   Interactions

All interactions are thought of being mediated by a particle in the standard model. Classically, forces were propagated through a field. The standard model however, states that interactions are achieved via the exchange of particles defined as gauge bosons. There are four fundamental forces, but not simply four analogous force-carrying particles. There are eight generators of the strong nuclear force that correspond to eight gluons. The weak interaction is mediated by three distinct particles, and at present time there is no concise quantization of the gravitational force. The distinguishing properties of the gauge bosons, all of which have an integer spin of 1, are described in Table 2.

Table 2: Properties of Gauge Bosons [4]

Gauge Bosons (Spin=1)				
Force	Symbol	Range	Charge	Mass (MeV)
Strong	gluon	10^{-15}m	0	0
Weak	W^+, W^-, Z^0	10^{-18}m	+1 ,-1 ,0	804,804,912
Electromagnetic	γ	∞	0	0

1.4 Resonances

Each nucleon is a composite structure of quarks, which does not include a strange quark. Albeit, a strange quark may exist in the sea, the discussion in limited to valence quarks. This begs the question of how a particle containing a strange quark can be created from such a nucleon that does not contain one. Nucleons have a spectrum of excited states, defined as nucleon resonances. Looking at the decay products of the resonances allow for the separation of overlapping resonance states. An understanding of the properties of these resonances will provide information about how the quarks that make up these particles interact, and shed light on the nucleon internal structure. [5]. Accordingly, greater knowledge can be discerned about nucleon sub-structure through their resonances, which may be excited by a transfer of energy via an electromagnetic probe. As Table 1 illustrates, the lightest quarks are the *u, d,* and *s*. The introduction of an *s* quark into a nucleon results in *strange* matter, with exciting new properties. At present, all predicted resonances for nucleons, and hyperons, (a baryon with an *s* quark replacing a *u* or *d)*, are not fully understood, and not well defined by the use of non-perturbative Quantum Chromodynamics (nQCD). Well established predictions, are denoted by three and four stars, defined as being observed in at least two experiments [6], while one and two stars are not. In view of this fact, it is appealing to look carefully at non-strange resonances that result in strange decays.

2.   STRANGENESS PRODUCTION

2.1   Physics Motivation

A study into kaon photoproduction provides important information describing the strangeness production mechanism, the structure of hadrons, as well meson-baryon coupling constants. Investigation into strangeness production has been carried out since the late 1950's. More recently however, strangeness production by electromagnetic interaction is drawing strong interest because strangeness is recognized as a good probe to study the internal structure of baryons, as discussed by Bennhold for the case of photoproduction [5]. A weak coupling constant permits the use of a single channel analysis to sufficiently describe the process [7]. Many of the observables of the elementary kaon photoproduction process have been investigated on a proton target, but comparatively, there has not been much effort placed on exploring heavier or neutron targets [8]. The lack of experimental data regarding the photoproduction process on a neutron is due to the inability to prepare solitary a neutron target. Therefore, the deuteron is an ideal target for the study of the process on a neutron, predominantly due to its low binding energy of 2.225 MeV. The purpose of the research is to further understand and study experimentally the elementary process via the $d(\gamma, K^0) \Lambda p$ reaction. Primarily, due to the unique features of a neutron target [9]:

1. There is no charge involved in the reaction, thus the Born term in the t-channel does not contribute.

2. Due to the low energy, there are not many resonances that need to be included.

3. It is a mirror reaction to the $p\ (\gamma,\ K^+)\ \Lambda$ process.

    a. From the isospin symmetry

        i. $gK^+\Lambda_p = gK^0\Lambda_n$

    b. The coupling constant in the u-channel term changes sign.

        i. $gK^+\Sigma^0 p = {-}gK^0\Sigma^0 n$

This would allow for a comparison with the more understood K^+ photoproduction process. This comparison will hopefully lead to a deeper understanding of the elementary strangeness photoproduction process. An addition of strangeness presents a challenge to models in the low-energy regime as will be discussed in Section 2.2. The Tohoku University "strangeness group" is currently investigating the photoproduction process of neutral kaons by the Neutral Kaon Spectrometer 2 (NKS2) at their Laboratory for Nuclear Science (LNS). Investigation of the photoproduction process on a carbon target was first experimentally conducted at this facility [10].

2.2   Photoproduction Models

Theoretical models supply an approach to understanding the physics behind the decay of non-strange baryons. The Regge Model is implemented for high-energy incident photons (E_γ> 4 GeV), while the Chiral Perturbation theory is used up to the threshold region, for energies in the resonances region the isobar model is predominantly used [11]. Hadronic models are such that the hadrons themselves are viewed as elementary particles [12]. When viewed as such, the reaction may be sufficiently described by an isobar model or calculation. Isobar models used to describe the reactions in the region of low energy have been found to diverge with increasing energies, and do overlook some of the inner details of the strong force interaction because they are viewing nucleons, composite structures, not as such. [13] Nevertheless, they are applicable for lower threshold energies where interaction amplitudes may be computed. The isobar impulse approximation on a deuteron explains the reaction such that the photon interacts with only one nucleon, producing the strange baryon, leaving the other nucleon undisturbed. The proton in a reaction on the deuteron acts as a spectator to the process.

2.2.1 Feynman Diagrams

It is commonplace to use Feynman diagrams to depict the scattering of multiple particles or decays of a single particle as shown in Figure 2[4]. By convention, photons are symbolized as a wavy line, fermions as a solid line,

gluons by a curly line, and meson as a dashed line Vertices, the points of intersections, are the terms that are included in the transition matrix element and include information about the nature of the interactions. The propagator is a common term for the exchanged particle. The use of Feynman diagrams as a tool for the construction of elementary operators has been verified [14].

2.2.2 Kinematics

A reaction that involves two incoming particles interacting and then producing two outgoing particles, can be adequately described by the use of four momentum vectors , $P_A = (E_A, \vec{p}_A)$.

$$p_A, m_A \qquad p_C, m_C$$

$$p_B, m_B \qquad p_D, m_D$$
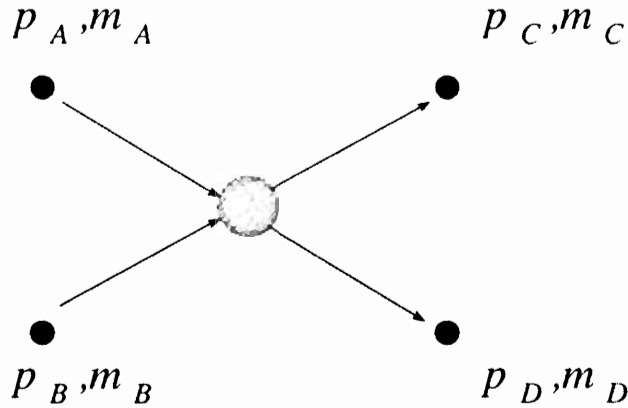
Figure 1: Generic process $AB \rightarrow CD$. Momentum and mass of ith particle are p_i and m_i

Where in terms of the production reaction discussed in this thesis, $d\ (\gamma, K^0)\ \Lambda p$.

$$A(\gamma) + B(N) \rightarrow C(K^0) + D(Y(\Sigma, \Lambda))$$
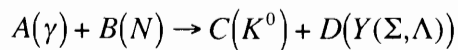
$A(\gamma)$	$B(N)$	$C(K)$	$D(Y)$
The incident photon	*The target Nucleon*	*The produced Kaon*	*The produced Hyperon.*

The process may occur via the *s, t,* or *u* channels, where *s, t,* and u are Mandelstam variables; Mandelstam variables are highly useful for many body final states formed from the scattering of two incoming and two outgoing particles, particularly due to being Lorentz invariant quantities [15]. In terms of four momentum vectors, where *A(γ)* and *B(N)* are known, the Mandelstam variables are calculated as:

$$s = (\gamma + N)^2 = (K + Y)^2 = W^2$$
The energy of the center of mass, where a nucleonic resonance is the propagator.

$$t = (\gamma - K)^2 = (N - Y)^2$$
The four momentum transfer via a kaon resonance

$$u = (\gamma - Y)^2 = (N - K)^2$$
The four-momentum transfer via hyperon resonance .

$$M_Y^2 = Y^2 = (\gamma + N - K)^2$$
The square of the missing mass of the photo-produced hyperon.

$$s + t + u = M_A^2 + M_B^2 + M_C^2 + M_D^2$$
Constant

2.3   Kaon Photoproduction Reaction Channels

The strangeness photoproduction process is a promising probe to study the creation of hypernuclei. Experiments conducted at lower energy reveal that

the elementary production process is closely related to the internal structure of the nucleus. Tree level, or first order, Feynman diagrams are implemented to convey the possible reaction mechanisms, and also for the calculation of the reaction amplitudes. A theoretical cross section can be found through the sum of the intermediate states depicted in the Feynman diagrams [16]. There are six known isospin channels of strangeness photoproduction as show in Table 3. The threshold energy is that of the incident photon beam and a fixed target. The use of Feynman diagrams provides a means to express the reaction in terms of the invariant Mandelstam variables, as represented in Figure 2. The hadronic vertices are denoted as solid black dots, while the electromagnetic vertices are denoted a cross, circumscribed in a circle.

Table 3: Kaon production channels and corresponding threshold energies.

Reaction channel	Threshold energy (MeV)
1. $\gamma + p \rightarrow K^+ + \Lambda$	911.1
2. $\gamma + p \rightarrow K^+ + \Sigma^0$	1046.1
3. $\gamma + p \rightarrow K^0 + \Sigma^+$	1047.5
4. $\gamma + n \rightarrow K^0 + \Lambda$	915.3
5. $\gamma + n \rightarrow K^0 + \Sigma^0$	1052.2
6. $\gamma + n \rightarrow K^+ + \Sigma^-$	1050.4
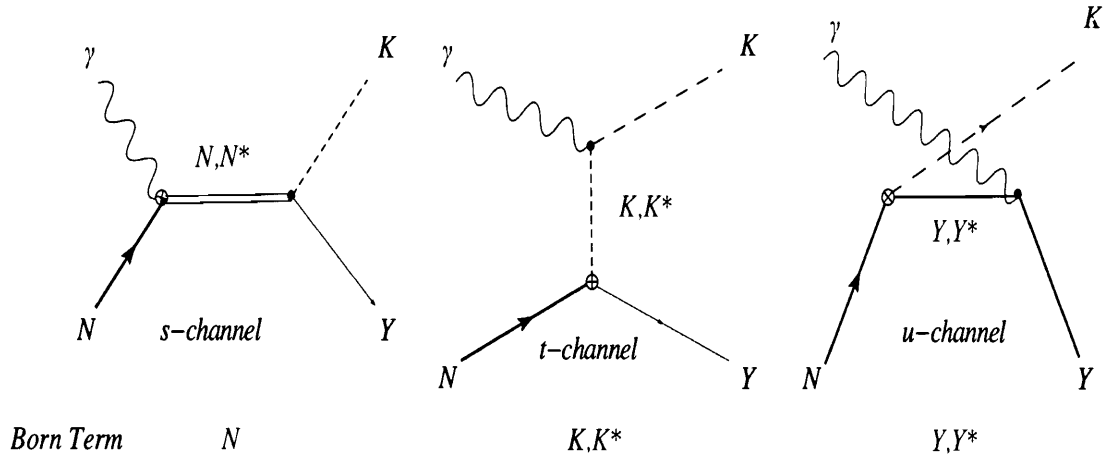
Figure 2: Kaon photoproduction diagrams.

Each diagram provides unique information regarding the dynamics of the process. Nucleon resonances can only be observed in the s-channel. The neutral kaon is an equal mixture of two states $K^0 = K_s^0 + K_L^0$, and thus not a unique eigenstate. The subscript L refers to the *long,* named so, because of its longer lifetime, that of $c\tau$=15.33 m, and S for the *short* with a lifetime of $c\tau$=2.68 cm. The focus of the experiment will be on the K^0 short, due to the $c\tau$ of the K^0 long and restrictions in detector size construction.

2.3.1 Cross Sections and Amplitudes

The experimental observable through which most of the physics is resolved lies in the calculation of the cross section, which for scattering experiments is a measurement of the probability of two particles colliding, and resulting in the desired reaction products. The total cross section includes the addition of both inelastic and elastic cross sections of the reaction. The differential cross section refers to the amount of reactions as seen by a detector covering a specific solid angle. The total cross is the integral over the entire solid angle and ranges of energies.

$$\sigma_{tot}(E) = \int\limits_{0}^{E'_{max}} \int\limits_{4\pi} \frac{d^2\sigma(E,E',\theta)}{d\Omega dE'} d\Omega dE' \tag{1}$$

The reaction amplitude is a direct relation to the probability of a process occurring. It is the transition matrix element between the initial and final state is M_{fi}.

$$M_{fi} = \left\langle \psi_f \left| H_{int} \right| \psi_i \right\rangle = \int \psi_f^{*} H_{int} \psi_i d\vec{r}^{\,3} \tag{2}$$

The reaction rate per target and beam particle is W, and should not to be confused with the square root of the energy available in the center of mass.

$$W = 2\pi \left| M_{fi} \right|^2 \cdot \rho(E'), \tag{3}$$

Here $\rho(E')$ is the density of final states in energy interval dE'. W can also expressed in terms derived from the geometric cross section.

$$W = \frac{\sigma \cdot v_a}{V} \tag{4}$$

Here, v_a is the beam particle velocity, and V is the volume of the beam particles. Therefore, the cross section for a known particle flux is σ.

$$\sigma = \frac{2\pi}{v_a} \left| M_{fi} \right|^2 \cdot \rho(E') \cdot V \tag{5}$$

The inclusive cross section for the $d\,(\gamma,K^0)\Lambda p$ reaction where the energies and momenta are measured in the lab frame, can be calculated as described in reference [11] as:

$$\frac{d^3\sigma}{d|\vec{p}_K|d\Omega_K} = \int \frac{m_{N'}\left(s - m_N^2\right)\vec{p}_K^2|\vec{p}_{N'}|}{4m_N E_\gamma E_K E_N|\vec{p}_\gamma - \vec{p}_K|} \frac{u_d\left(p_{N'}\right)^2}{\pi} \frac{d\sigma^e}{dt} d|\vec{p}_{N'}|d\Phi'_{N'} \tag{6}$$

In the above equation, $E_N = \sqrt{m_N^2 + \vec{p}_N^2}$ is used for the on-shell approximation, and $E_N = E_d - E_{N'} = E_K + E_\Lambda - E_\gamma$ for the off-shell approximation for the energy of the target nucleus, and $m_N = \sqrt{P^2(E,\vec{p})}$.
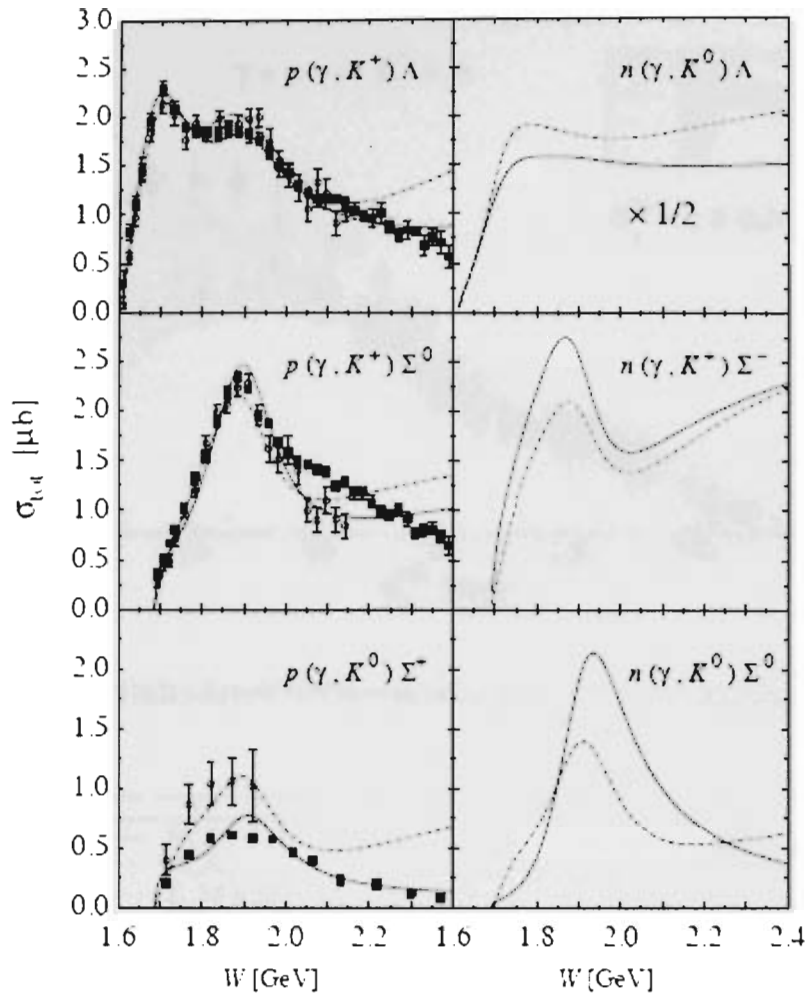
Figure 3: Total cross sections of kaon photoproduction. Dashed lines with Kaon-Maid calculations, and the solid line are SAPHIR data. [17]

Figures 3.a and 4.a display the experimentally measured cross section on a proton vs. W (GeV) and θ_{cm} respectively, and its comparison to the model predictions. Figure 4.b are the model predictions for the photoproduction process on a neutron, without a comparison as a consequence of the lack of experimental data.
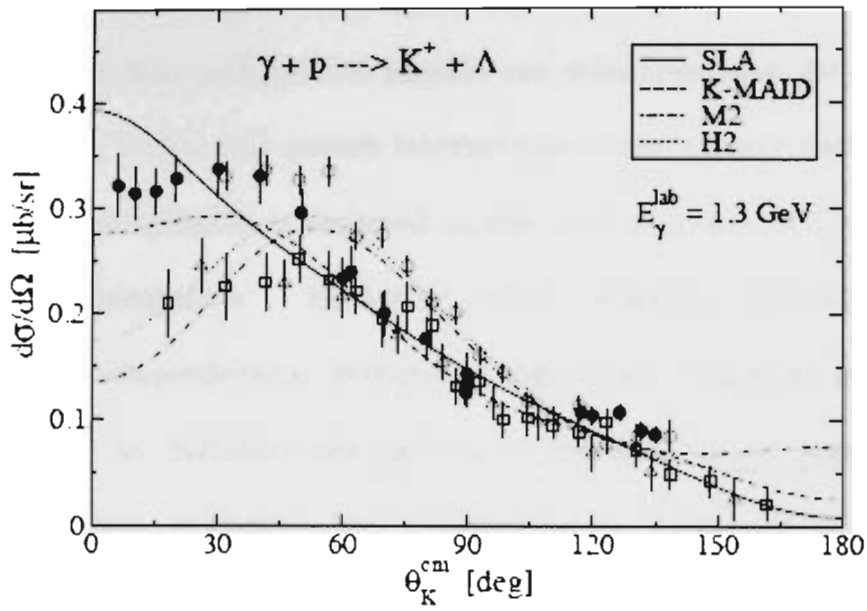
Figure 4.a: Calculated differential cross section on proton vs. θ_{cm}.
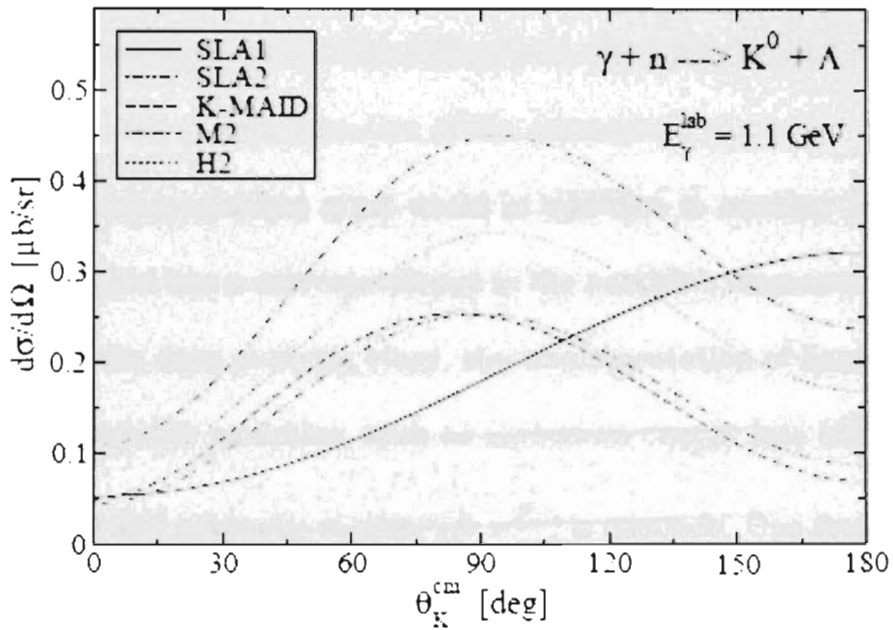
Figure 4.b: Models for E_γ= 1.1 GeV for photoproduction on neutron vs. θ_{cm}

[11].

3. EXPERIMENTAL RESEARCH PURPOSE

The fields of nuclear and particle physics are concerned with the structure of matter and the forces that govern interactions at the nuclear and sub-atomic level. Particular research is centered on the understanding of the production process of strangeness. Exploring exotic reaction channels, such as strangeness photoproduction, requires a high level of particle identification (PID), mainly to decipher the pertinent channels from more abundant ordinary reaction channels. The problem to be examined is the use of separate PID techniques and the determination of their limitations. Fundamentally, the property of PID techniques is the correct inferment of a particle's mass and charge from the physical measurements that can be accomplished experimentally. The difficulty in efficiently identifying hadrons lies in the fact that a determination of the momentum alone is not sufficient. A momentum measurement must occur in addition to another independent measurement that has a correspondence to the particle's momentum.

During the data analysis stage, the implementation of hard conditions (cuts) on measurable variables, such as ionization energy loss (*dE/dx*), time-of-flight (*TOF*) and magnetic rigidity ($\vec{B}r = \frac{p_\perp}{|q|}$) is common. One focus will be to demonstrate that a combination of ionization energy deposition and time of flight is a sufficient means of reducing the ambiguity of the unknown particle's identity [18]. The likelihood estimation (*LE*) technique for particle

identification is used in high-energy experiments, but it is not widely applied in medium energy nuclear physics experiments. An additional goal of the study is to compare the *LE* capabilities with those of traditional cuts, especially in the presence of partially overlapping distributions coming from different detector signals. The calculation of PID efficiency is more direct with the use of *LE*. These techniques will be used to identify particles that were produced in a neutral kaon photoproduction experiment. Efficiently extraction the underlying physics is dependent upon the identification mechanisms brought into play. [19]

3.1 PARTICLE IDENTIFICATION TECHNIQUES

3.1.1 Heavy Charged Particles Through Matter

Electromagnetic interactions are the most dominant and common of interactions that occur while a charged particle passes through matter. Two distinct events characterize the passage of charged particles, the first being the loss of energy by the particle, and the second being a deflection of the incident particle from its initial trajectory [20]. Of these, the inelastic collision of particles with the atomic electrons has the highest probability of taking place. The collision results in an energy transfer through the excitation and ionization of the atomic electrons. The average energy loss per unit path length is also referred to as the stopping power or dE/dx [21]. The most common techniques for the identification of hadrons, are through the

use of energy loss (dE/dx), time of flight, Cherenkov detectors, and lastly by transition radiation detectors,

3.1.2 Energy Deposition (dE/dx)

The method of particle identification by measuring the specific energy loss (dE/dx), has been successfully used for many years. The energy deposited is dependent upon the charge and velocity of the incoming particle, in conjunction with the absorbing material. Thus, prior knowledge of the mean energy loss for a specified absorber can allow for good particle identification and separations below minimum ionizing [22]. Average energy loss of a particle can be described by the Bethe-Bloch formula:

$$\frac{-dE}{dx} = 2\pi N_a r_e^2 m_e c^2 \rho \frac{Z}{A} \frac{z^2}{\beta^2} \left[\ln \left(\frac{2m_e \gamma^2 \upsilon^2 W_{max}}{I^2} \right) - 2\beta^2 \right] \tag{7}$$

This formula is traditionally implemented with the addition of the density effect δ and shell corrections C, resulting in the following:

$$\frac{-dE}{dx} = 2\pi N_a r_e^2 m_e c^2 \rho \frac{Z}{A} \frac{z^2}{\beta^2} \left[\ln \left(\frac{2m_e \gamma^2 \upsilon^2 W_{max}}{I^2} \right) - 2\beta^2 - \delta - 2\frac{C}{Z} \right] \tag{8}$$

where,

I	The mean excitation potential in eV
W_{max}	The maximum energy transfer to an electron in a single collision
N_a	6.022 x 10^{23} mol^{-1} is Avogadro's number
r_e	$e^2/4\pi\varepsilon_0 m_e c^2 = 2.817 x 10^{-15} m$, the classical electron radius.
$m_e c^2$	0.511 MeV is the electron rest mass energy
Z	The atomic number of the absorbing material
z	The charge of the incident particle.
A	The atomic mass of the absorbing material in g/mol
β	v/c, where v is the velocity of the particle
$\gamma = \dfrac{1}{\sqrt{1-\beta^2}}$	The Lorentz relativistic factor
δ	The density correction
C	The shell correction

The Bethe-Bloch formula accurately describes the average energy loss of charged particles as they pass through matter, but this is assuming a uniform loss in energy. The inclusion of the density correction is a result of polarization that may occur in the absorbing material [23]. In the non-relativistic region, dE/dx is proportional to $1/\beta^2$, where at $\beta=0.95$ particles

20

reach the minimum ionization point. A minimum ionizing particle has a dE/dx proportional to 2 MeVg⁻¹cm². In regards to relativistic particles, the deposited energy increases logarithmically after surpassing the minimum. Ionization energy loss approaches a gaussian distribution for thick absorbers, but with a decrease in absorber thickness the distribution acquires a tail. The fluctuation in energy loss for thin absorbers is sometimes called straggling, caused by the small number of collisions between atomic electrons and the transiting particle, with a large energy transfer. These fluctuations in energy loss follow the so-called Landau distribution [24]. The Landau distribution is an asymmetric distribution known for its tail. Accordingly, the mean ionization energy loss is not the same as the most probable energy loss value (MPV). [25]. Thus, the value of importance when attempting to fit histograms, is the MPV value, not the mean.

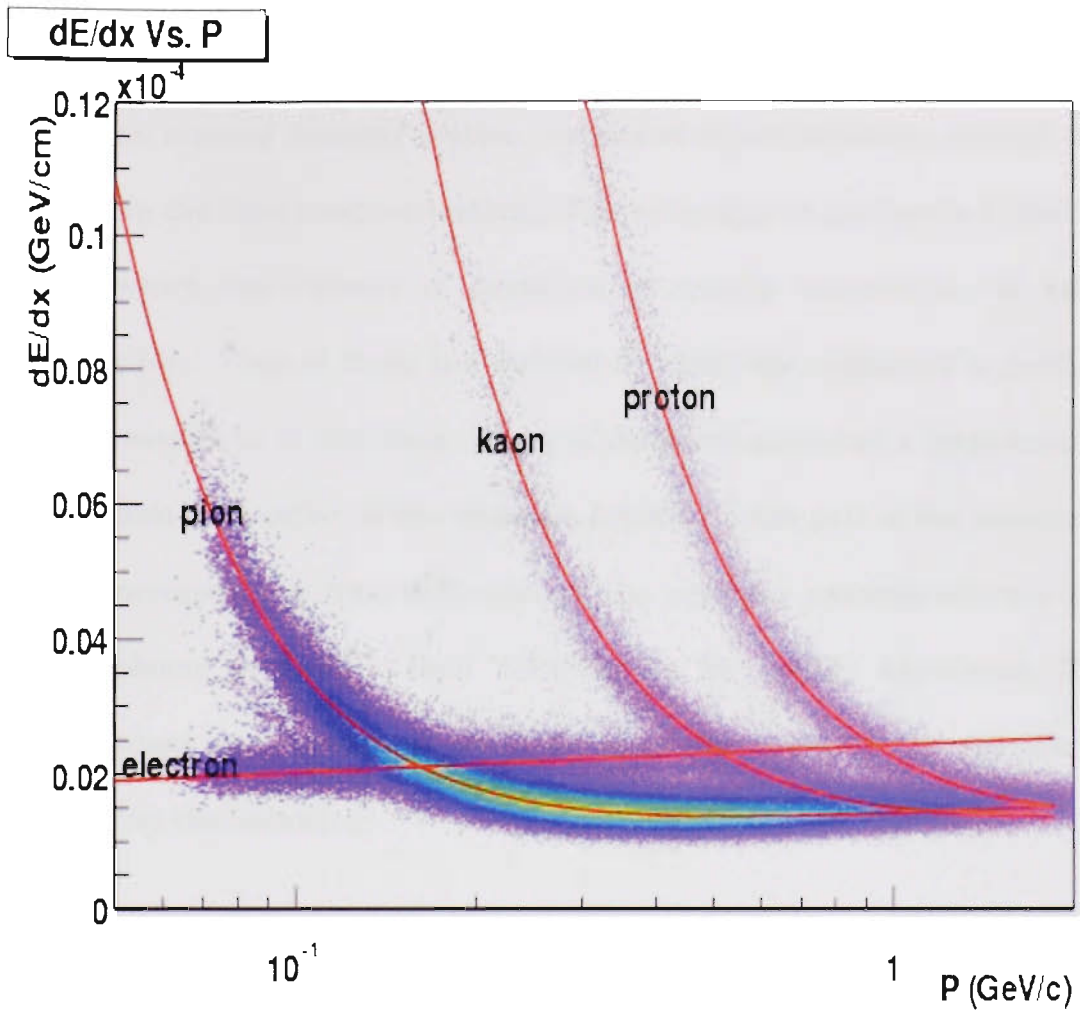
Figure 5: Mean energy losses of protons, pion, electrons, and kaons in argon
[26]

3.1.3 Time of Flight (T.O.F) Particle Identification

The most utilized detector for time of flight measurement is the plastic scintillation counter detector system. Details of the scintillation counter are discussed in the data analysis sections. This technique is applicable below 1.0 GeV, in which the velocity of particles, at specific momentum, is mass dependent [4]. Time of flight is a method in which the velocity of a particle can be measured as it traverses a pair of detectors placed at a large enough distance from each other. If the distance L between the pair of the detectors, and the corresponding time difference of the particles passage between the detector planes is known, then velocity can be readily calculated. The velocity, when ascertained, is $\beta = L/tc$, then the mass of the particle is calculated by the following:

$$p^2 = \left(m\gamma\beta\right)^2 \tag{9}$$

$$m^2 = \left(\frac{p}{\gamma\beta}\right)^2 = \left(\frac{p}{\beta}\right)^2 \cdot \frac{1-\beta^2}{1} = p^2 \cdot \left(\frac{1}{\beta^2}-1\right) \tag{10}$$

$$m = p\sqrt{\frac{t^2c^2}{L^2}-1}. \tag{11}$$

4.   EXPERIMENTAL METHOD

The lack of experimental data of photoproduction process on a neutron target, prompts the use of a deuteron to study photoproduction of a quasi-free neutron. Thus, the goal is to use experimental observables, such as cross sections, to verify theoretical model predictions such as isobar models that describe the production mechanism off a neutron [27]. The reaction to be studied is $\gamma + d \rightarrow K^0 + Y + N$, where d is the deuteron, Y is the produced hyperon (Λ or Σ), and N is the spectator nucleon.
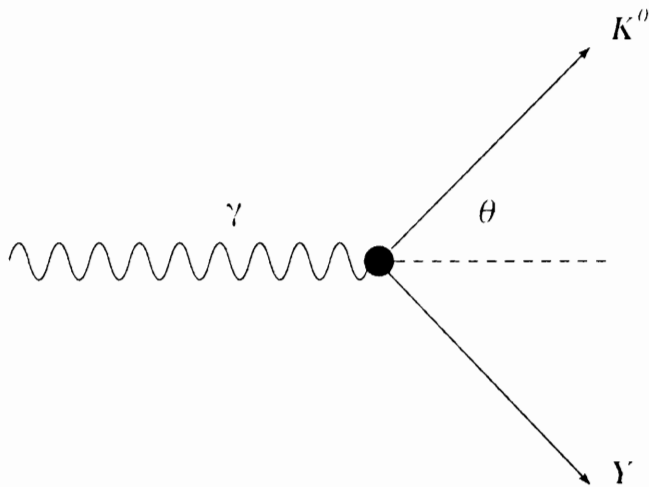

Figure 6: Kinematical diagram of kaon photoproduction in lab frame

Once electromagnetically produced, the K^0 subsequently decays into $\pi^+\pi^-$ with 68.95% probability or into $\pi^0\pi^0$ with a 31% probability.
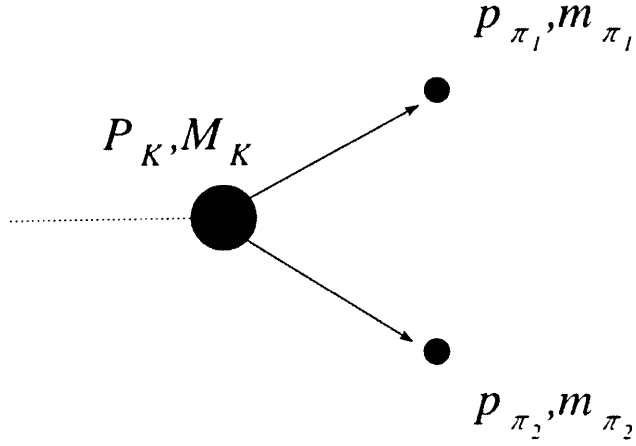
Figure 7: Two-body decay in decaying particle's center of mass frame.

The square of the invariant mass of the decay particle is calculated by,

$$M^2{}_{K^0} = M\left(\pi^+\pi^-\right)^2 = \left(\sqrt{\vec{p}_{\pi^+}{}^2 + m_{\pi^+}{}^2} + \sqrt{\vec{p}_{\pi^-}{}^2 + m_{\pi^-}{}^2}\right)^2 - \left(\vec{p}_{\pi^+} + \vec{p}_{\pi^-}\right)^2 . \quad (12)$$

The identification of kaons is difficult due to its short life times, and the rareness of its production in comparison to ordinary reactions. For that reason a good identification of the pions is necessary in order to re-construct the photo produced kaon and allow for an identification of the produced hyperon.

5. INSTRUMENTATION

5.1 The Neutral Kaon Spectrometer 2 (NKS2)

The NKS2 was assembled at the Laboratory of Nuclear Science of Tohoku University (LNS) in 2004, replacing an earlier version the Neutral Kaon Spectrometer (NKS). Its main purpose is to investigate the photoproduction process. It is predominately used in the identification of the K^0 through the decay channel $K^0 \rightarrow \pi^+\pi^-$.

Figure 8: Internal detector arrangement of NKS2 [27]
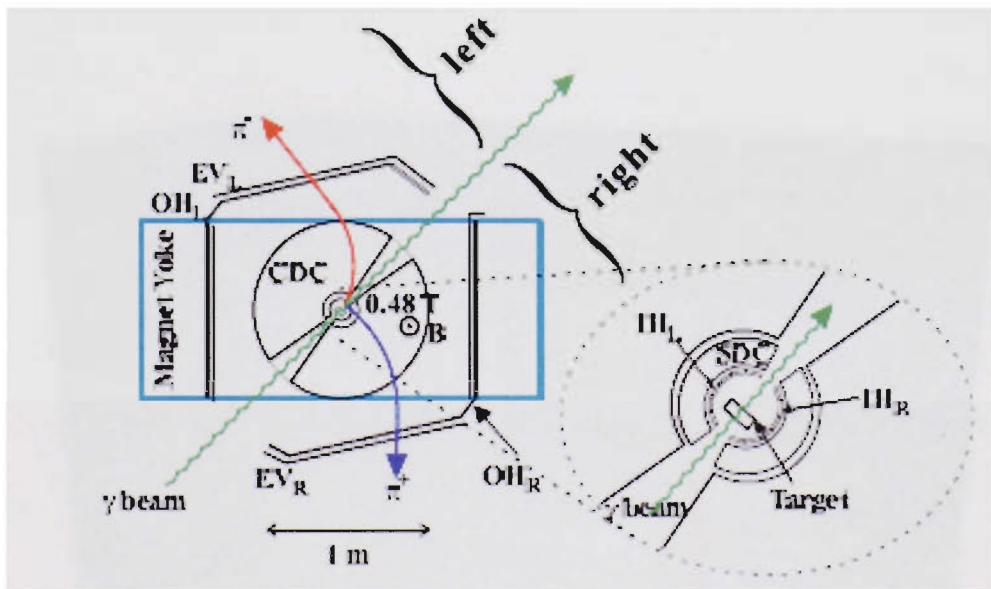
The NKS2 consists of an array of detectors centered on a target housed in a vacuum chamber. The target is surrounded by a plastic Inner Hodoscope (*IH*), which is the start trigger for the time of flight, placed within the Straw Drift chamber (*SDC*) and both are enclosed in a Cylindrical Drift Chamber (*CDC*). These detectors reside within the poles of a dipole magnet. An outer

plastic scintillator hodoscope *(OH)*, the stop trigger for time of flight, was then placed outside the drift chambers. Lastly, in order to improve trigger efficiency, and thus reduce the level of background as a result of pair production from the photon beam, a Lucite Cherenkov and scintillator combination Electron Veto *(EV)* detector was installed on a zero degree plane perpendicular to the beam line. The pair produced e^+e *that* may result photon beam, is only generated in the forward direction.
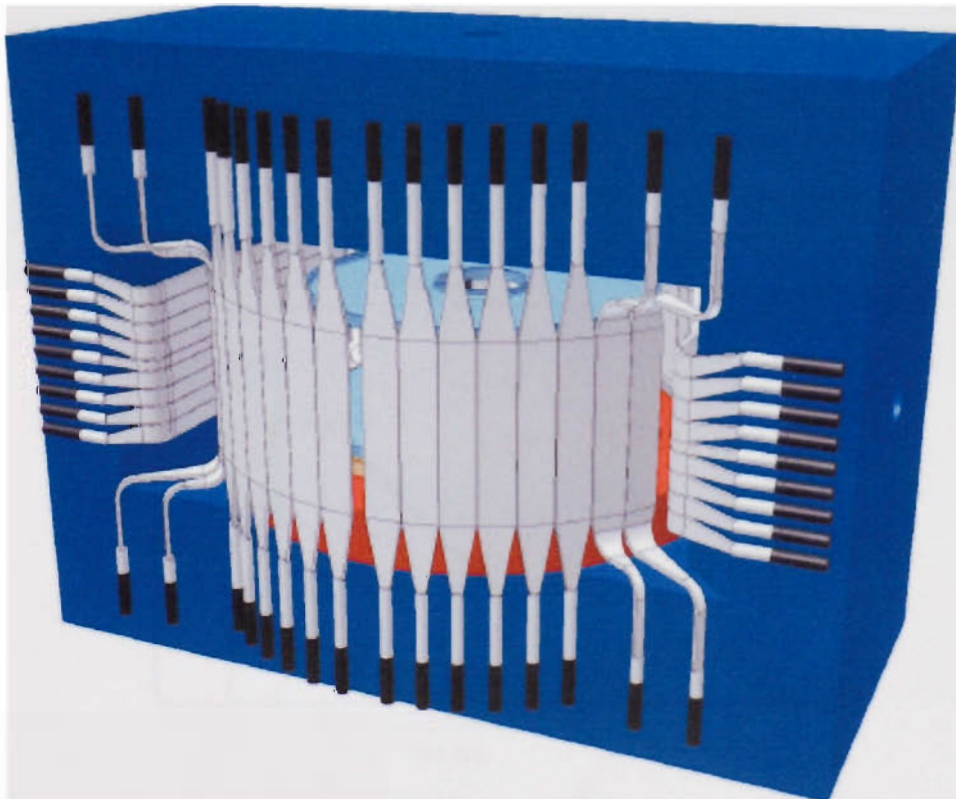

Figure 9: Neutral Kaon Spectrometer 2 (NKS2) fully assembled [27]

5.2   The Photon Beam

A carbon wire, 11 microns in diameter is inserted as a target for the electrons on the booster ring to generate the photon beam. The electrons are injected from a 200 MeV LINAC and accelerated to 1.2 GeV. High-energy electrons predominately lose energy in matter by bremsstrahlung, the electromagnetic radiation produced from an accelerating charged particle, at a rate nearly proportional to its energy [20]. This occurs due to scattering of electrons from the electric fields of the nuclei and dominates above a critical energy of 10 MeV. The photon beam is produced via bremsstrahlung interactions of the electron beam with the carbon wire.
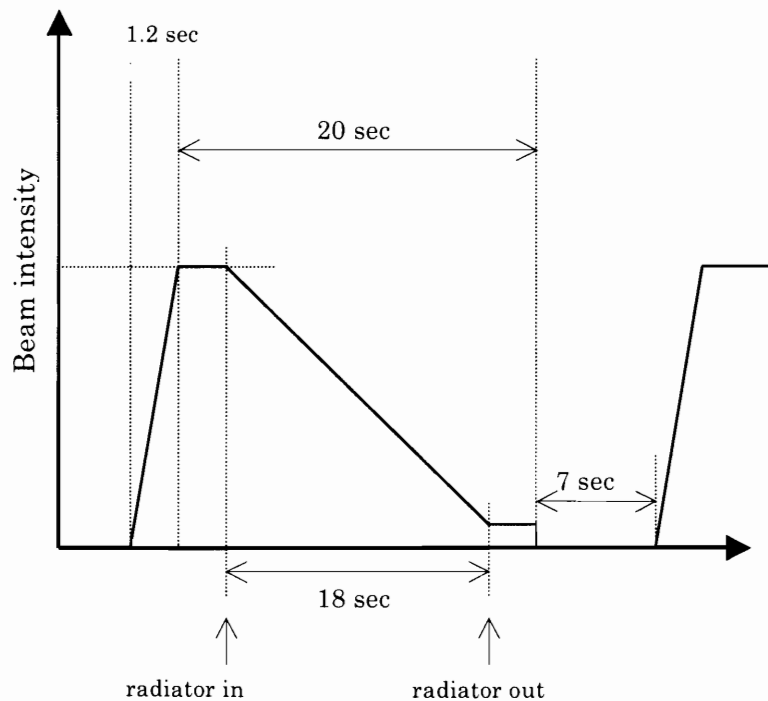

Figure 10. Radiator effect on beam intensity.

The approximate diameter of the photon beam downstream, from the carbon wire at the target location, is 3-5 mm [28]. The emitted photon enters into the *NKS2* and the recoiled electron is then tagged by the STB-Tagger system.
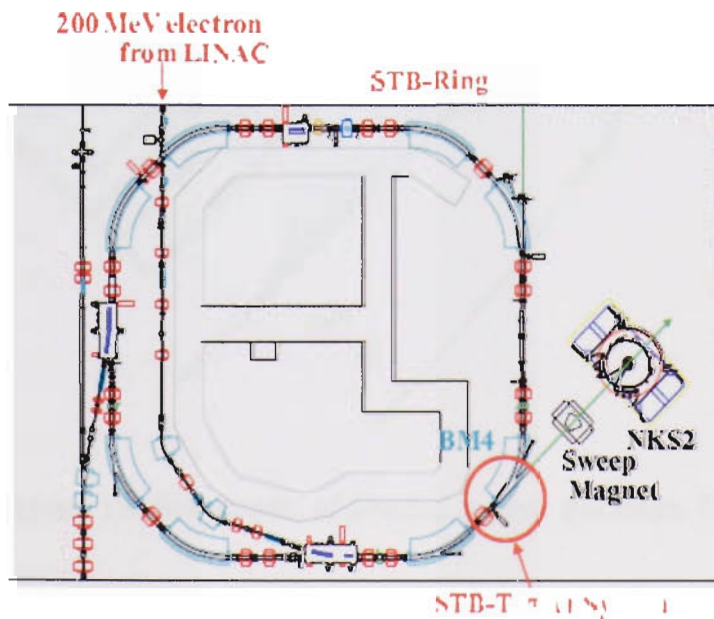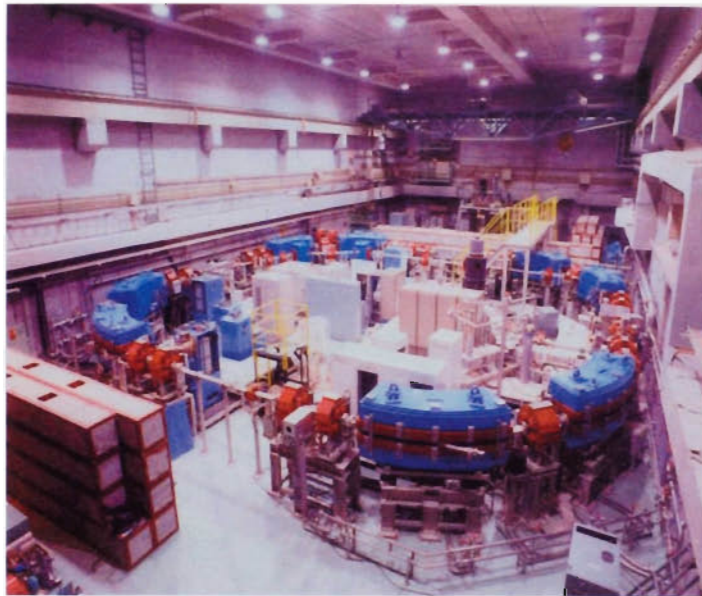

Figure 11.a&b: Laboratory of Nuclear Science (LNS) experimental Hall[29]

5.3. Photon Beam Tagging System

Scattered electrons are tagged by the STB-tagger system. The tagger detector package enabled the determination of the incident photon energy in addition to the number of photons reaching the deuterium target. The system is composed of two individual tagger systems defined as TagF and TagB as well as a magnet to be used for analysis. TagF is assembled from fifty finger segments of plastic scintillators, and TagB consists of twelve segments of plastic counters.

Figure 12: Schematic of photon tagger package. [28]

The tagger allows for tagging of photons over a range of 0.8- 1.1 GeV with an accuracy of ± 10 MeV on the produced photon beam [9].

5.3.1 Tagger Energy Calibration
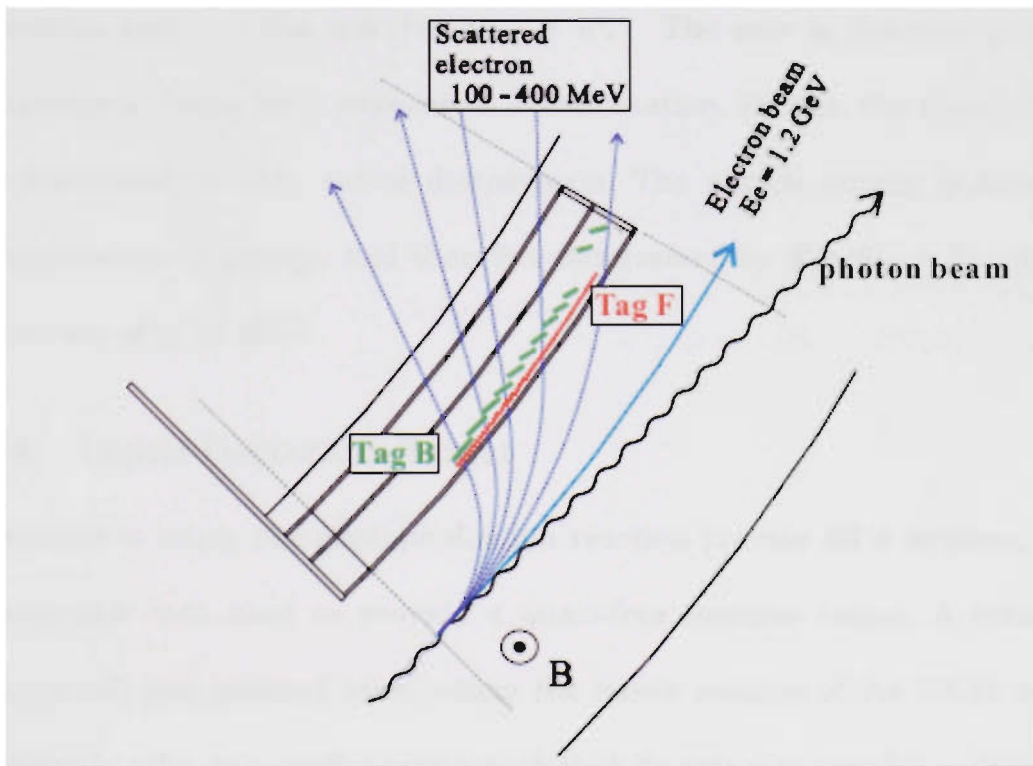
The calibration of the tagging system took place prior to and following the experimental run. A correct calibration of the tagging detectors results in a correlation between the tagger segment number and the energy of the photon incident on the target, thus, it provides useful information of the photon energy and the number of the photons. This was accomplished through the use of a sweeping magnet and drift chambers. The incoming photon is incident on a copper wire of approximately 0.9 mm, generating an electron-positron pair, via the reaction $\gamma \rightarrow e^- \ e^+$. The pair is detected in a drift chamber allowing for a momentum determination. Finally, the energy of each is calculated as they exited downstream. The photon energy is known by conservation of energy, and therefore determined by $E_\gamma = E_{e+} + E_{e-}$ with an accuracy of $\pm$ 10 MeV.

5.4   Liquid Deuterium Target

In order to study the photoproduction reaction process off a neutron, liquid deuterium was used to provide a quasi-free neutron target. A cylindrical target cell was inserted 15 mm from the center position of the NKS2 into the magnetic yoke, in a configuration such that its axis was parallel to that of the beam line [30]. The target cell was remotely monitored to ensure that it remained below its boiling point. During the experimental runs, the absolute

pressure of the target was (50 ± 1) kPa at an average density of 0.17 g/cm^3 [5].
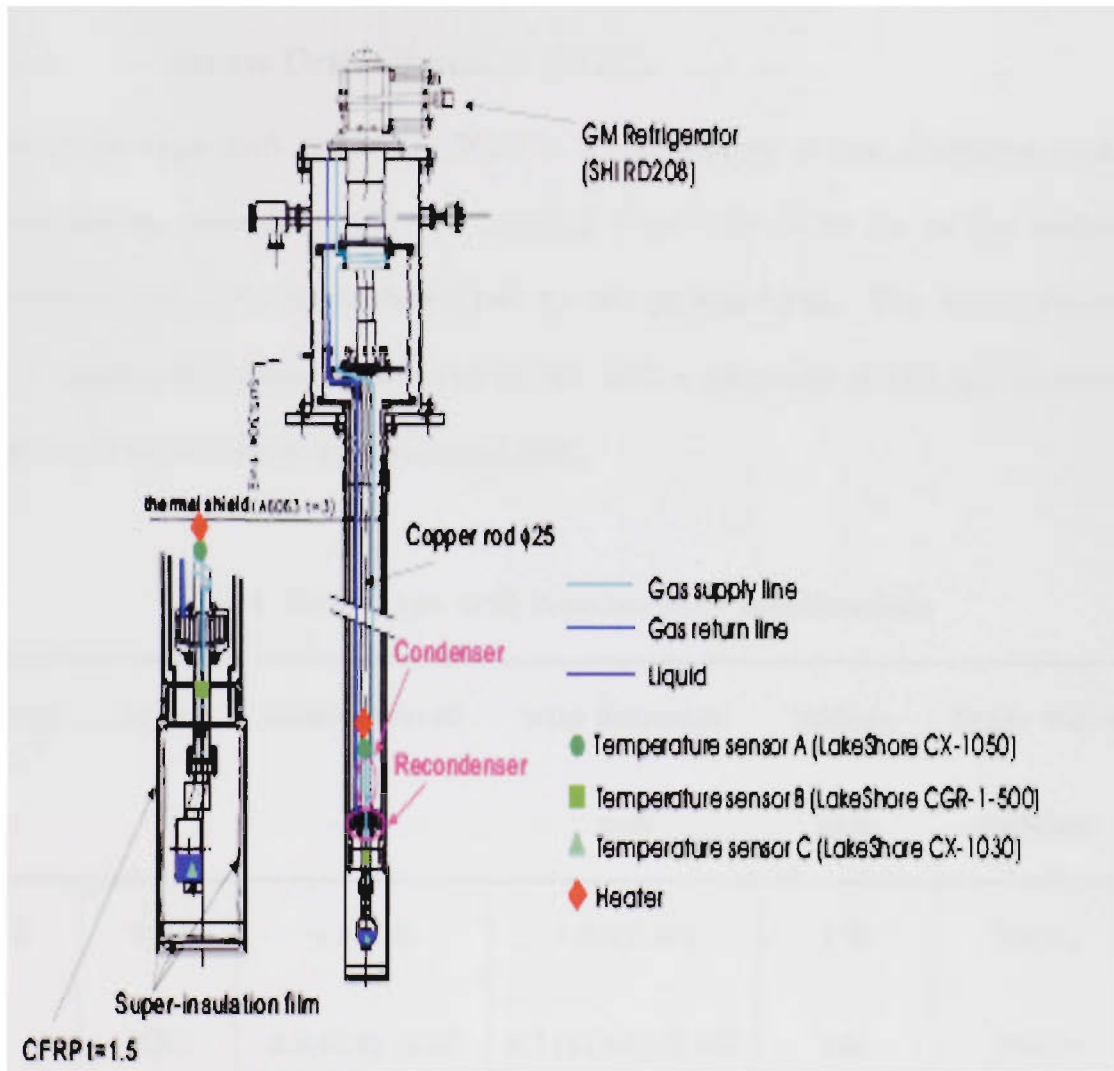

Figure 13: Schematic of liquid deuterium target. [31]

5.5 Tracking Drift Chambers

Drift chambers are extensively used in experiments because of the necessary tracking information that they provide. The NKS2 used a combination of a

honeycomb cylindrical drift chamber and a straw type drift chamber for tracking and vertex reconstruction purposes.

5.5.1 Straw Drift Chamber (SDC)

The straw type drift chamber (SDC) is a conjunction of two chambers with three layers, providing coverage ranging from 7.28-10.20 cm in the radial direction, and 10^0-170^0 with respect to the photon beam. The straw tubes were constructed from aluminized Mylar with a diameter of 180 millimeters Figure 11 shows the fully assembled SDC.

Table 4: Straw type drift chamber wire specifications

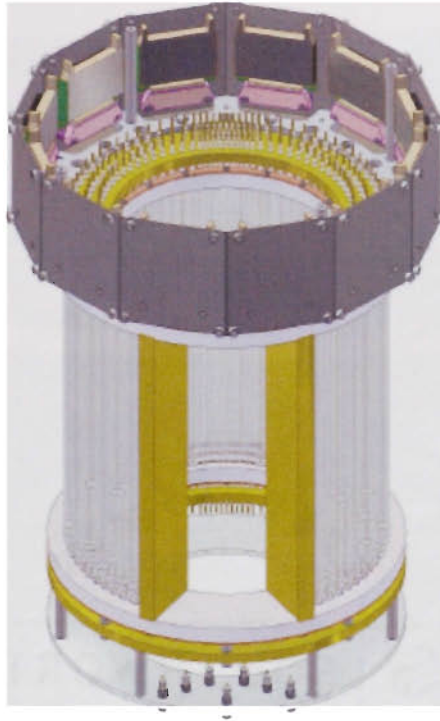| group	layer	angle covered	wire diameter	radius	sense wires
		deg	mm	mm	number
1	1(X)	4.8(2.4)	4.60(2.30)	110	56(11)
	2(X')	4.8,(3.6),{2.4}	5.11(3.85),{2.56}	122	56(11)
	3(X)	4.4(2.4)	5.67(2.83)	135.3	56(11)
				Total	202

Figure 14: Schematic view of Straw Type Drift Chamber (SDC)[27]

5.5.2 Cylindrical Honeycomb Drift Chamber (CDC)

The cylindrical honeycomb drift chamber with a total diameter of 160 cm consisted of ten layers. They were arranged such that there were five groups of 2 layers each. The angle of coverage was from 15^0-165^0 in the horizontal direction, with a radial coverage of 13.5-48-5 cm, with respect to the photon beam. Each sense wire was made from gold plated tungsten with a diameter of 30 microns. Conversely, each field wire was on the order of 100 microns thick. It allows for the tracking of the charged particles in three dimensions, and is a necessary detector to measure the pion decay from the neutral kaon.
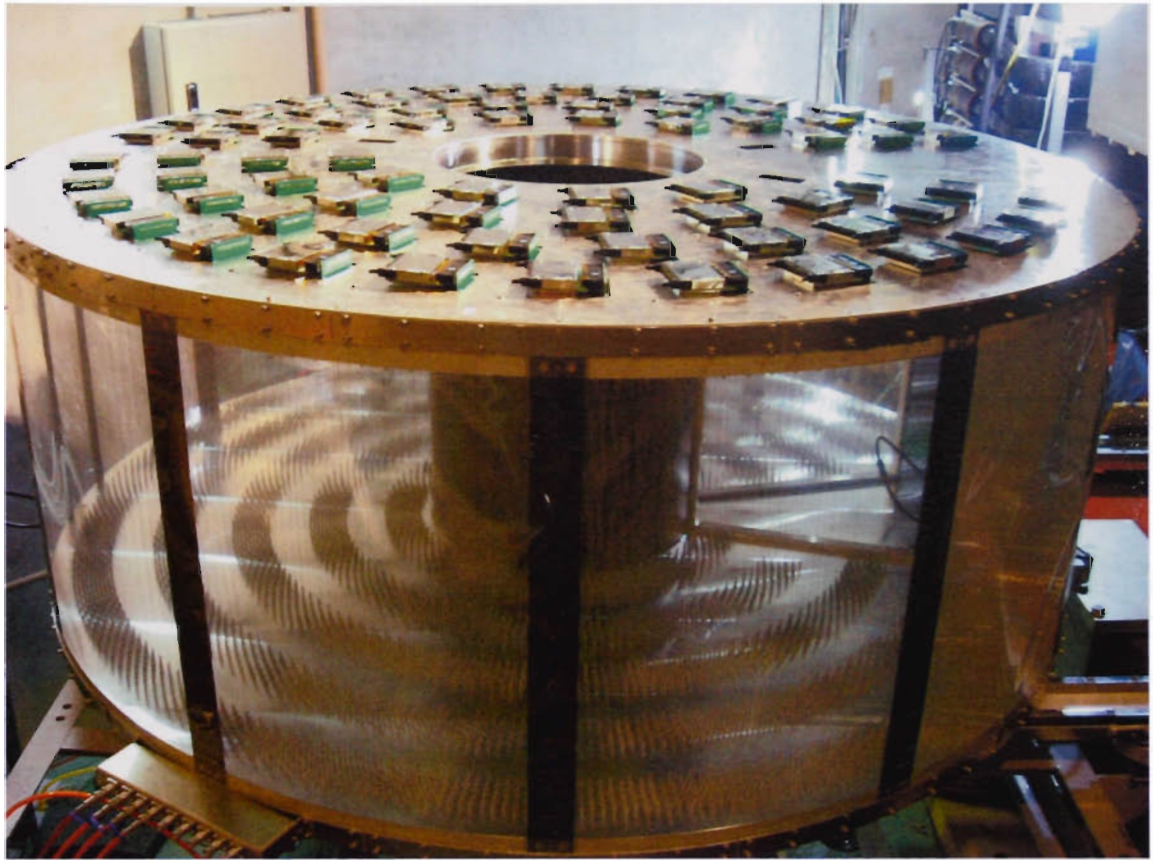
Figure 15: Cylindrical Honeycomb Drift Chamber (CDC) [29]

Table 5: Cylindrical type drift chamber wire specifications

group	layer	size	wire size	stereo angle	radius	sense wire number
		deg	mm	deg	mm	
1	1(X)	4.75	10.36		250	67
	2(X')	4.75	11.10		268	68
2	3(U)	3.50	11.30	6.21	370	89
	4(U')	3.50	11.84	6.52	388	90

group	layer	size	wire size	stereo angle	radius	sense wire
3	5(X)	2.70	11.54		490	119
	6(X')	2.70	11.96		508	120
4	7(V)	2.20	11.71	6.44	610	143
	8(V')	2.20	12.05	6.63	628	144
5	9(X)	1.85	11.78		730	175
	10(X')	1.85	12.07		748	176
					Total	1191

5.6. Hodoscope Counters

5.6.1 Inner Hodoscopes (IH)

The inner plastic scintillation hodoscope was essential for providing time of flight information and was also implemented as an initial trigger. It is composed of 16 plastic bars, with seven arranged on each side of the beam line as shown in Figure 14. The inner radius of the plastic segments was 58 mm and the outer 63 mm. The signals generated by photomultipliers were split into two, one was routed to a constant fraction discriminator for trigger logic, and the other to the ADC. The time of flight information obtained in conjunction with the OH, along with the energy calibration is discussed in the analysis section.
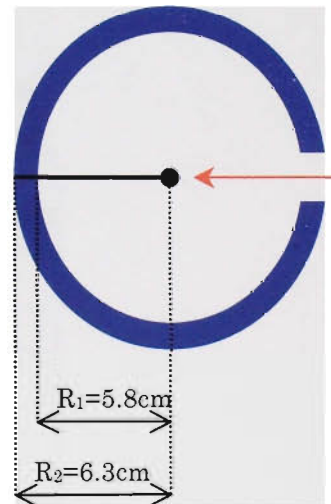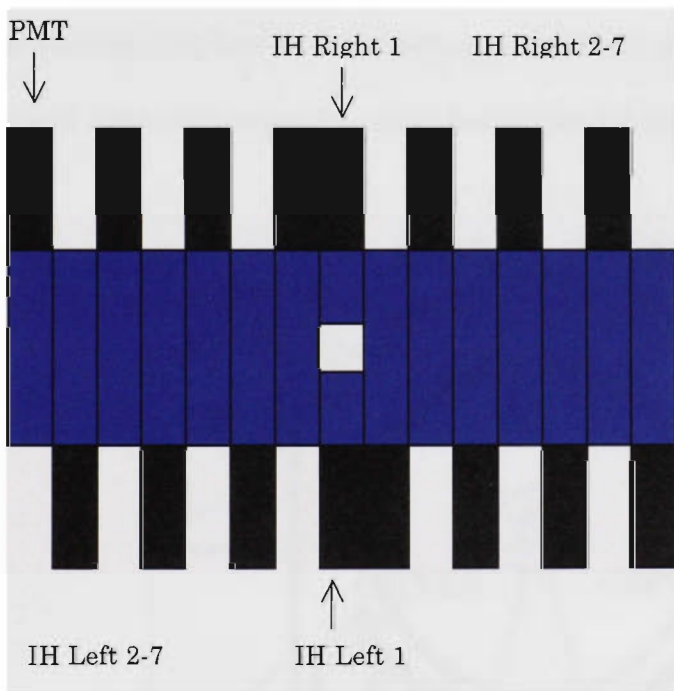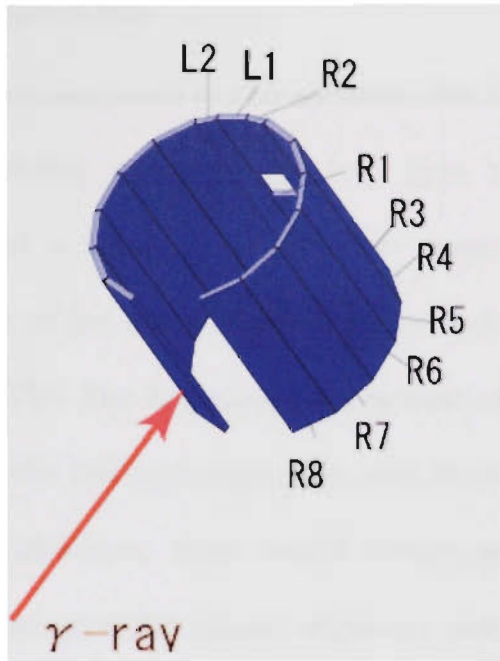
Figure 16: Photomultiplier arrangement for IH

5.6.2 Outer Hodoscope (OH)

The outer hodoscope was composed of two sections, one being vertical and the other horizontal, providing coverage for two pion events. The vertical component consisted of a total of twenty four segments, having twelve arranged on either side of the beam, defined as outer hodoscope vertical left (OHVL) and right (OHVR). The horizontal component of the outer hodoscope had nine segments for the left and right side, and since they were arranged parallel to the beam direction, they would detect particles with a high curvature. OHV 8-12 and all OHH plastic segments were affixed light guides in order to transport the signals outside of the magnetic dipole region because of a photomultiplier's performance sensitivity to strong magnetic fields. The vertical segments were 60 cm in height and 4 cm in width thickness.
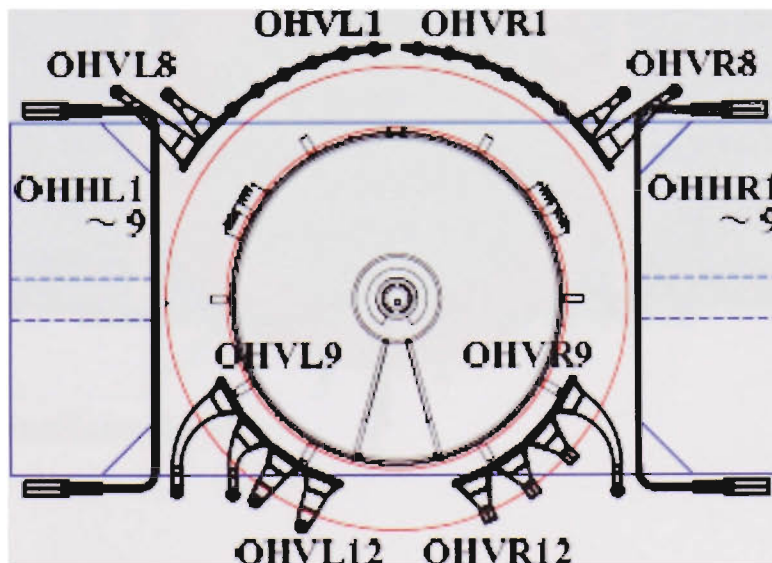

Figure 17: NKS2 with the Outer Hodoscope installed. [27]

5.7   Electron Veto Counter (EV)

The photon beam will contribute a lot of background via the pair production process. In an attempt to reduce this, an electron veto counter was constructed and placed on a zero degree plane perpendicular to the beam line. The detector was composed of Lucite Cherenkov (EVL) and scintillator (EVS) counter. In addition, the electron veto counter played an important role as part of the main trigger logic, as discussed in Section 5.8.
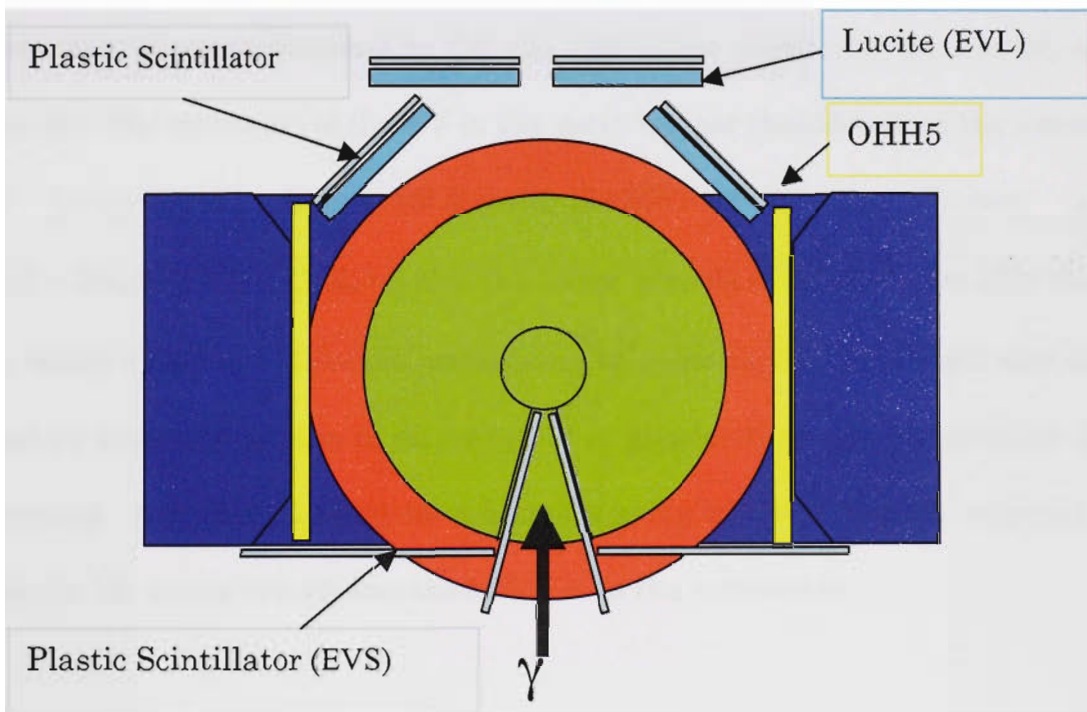
Figure 18: Electron Veto detector placement.

5.8 Triggered Event

A trigger is usually a set of detectors that works in combination to indicate when an event of significance has taken place. The trigger determines when the signals of the detector package should be recorded. An ideal trigger would eliminate the recording of events not of interest, and increase the retrieval of events that may contain information regarding the physics to be explored. The main trigger (*MT*) for the experiment was $MT = Beam \otimes Right \otimes Left$. *Beam* was equivalent to a photon being generated and tagged with an over a range of 0.8<$E\gamma$<1.1 GeV, and a two-particle event passing through the *IH*. *Right* $\otimes$ *Left* involved a hit such that there was a two-particle event detected in *IH*, the *OH* either vertical or horizontal, and the *EV*. The inclusion of the *EV* in the main trigger should reduce the amount of background. $Right = IHR \otimes OHRU \otimes OHRD \otimes EVR$, the former, and $Left = IHL \otimes OHLU \otimes OHLD \otimes EVL$ the latter. Events of interests are only those in which there is a detected coincidence of pions hitting both right and left, and an incoming photon of an energy at or greater than the threshold for the reaction. A triggered event for a kaon decaying into two pions is depicted in Figure 19, where the photon beam line is in the *x* direction.
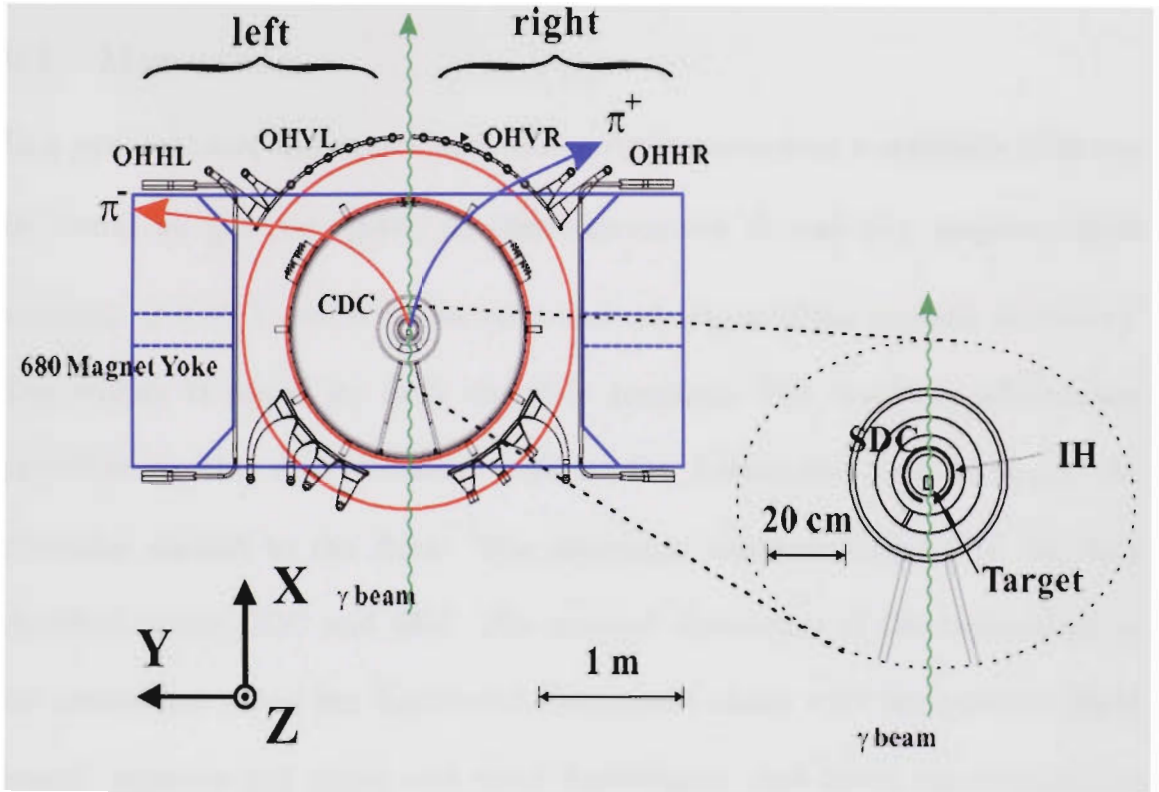
Figure 19: Triggered Event. [27]

6. DATA ANAYISIS

6.1. Momentum

In a general case, the momentum of a particle traversing a magnetic field can be found as $|\vec{p}| = \gamma m v = |q\vec{B}R|$, in this experiment B was the magnetic field strength of 0.43 T and R is the radius of curvature of the particle trajectory. The radius is found by drift chamber tracking. The tracking information provided by the drift chamber was in the horizontal direction (p_h), the direction normal to the field. The curvature was calculated from the hits detected in the CDC and SDC. The vertical component of the momentum is an estimation using the horizontal component along with the particle flight length between the inner and outer hodoscopes, and lastly the vertical hit position on the outer hodoscopes counter, Z_{OH}. A 4th order Runge-Kutta fit method was employed in determination of the Flight Length (*FL*) [28], and the vertical momentum component is subsequently arrived at as

$$p_v = \frac{Z_{OH}}{FL} \cdot p_h \; .$$
(13)

Hence, the particle momentum was calculated by

$$|p| = \sqrt{p_h^2 + p_v^2} \; .$$
(14)

6.2   Energy Deposition *(dE/dx)*

6.2.1 Scintillation and Photomultiplier (PMT)

The plastic scintillation detector is probably the most highly used type of detector for particle detection. A plastic scintillator detector, in simplest terms, is a piece of plastic that has been glued to the glass face of a PMT by some type of optical cement or grease. It allows for the extraction of information regarding the incident radiation or particle by emitting a small flash of light upon interaction. The light is a product of excited atoms being de-excited and releasing the excitation energy. High response photomultipliers were attached to only one end of the plastic scintillators that formed the inner hodoscopes but to both ends of the light guides affixed to the outer hodoscope scintillators.

The PMT works from the principle of Einstein's photoelectric effect; PMTs are sensitive enough to detect single photons. Light that reaches the face of a PMT will enter through a glass window. Upon entry of the PMT's face the photons will then "knock" out an electron via the photoelectric effect. The PMT is held at a high voltage, which, in turn causes the photoelectrons emitted at the cathode to be accelerated to the first dynode and "knock" out more electrons. This process will be repeated through the remaining dynode stages resulting in an avalanche of electrons at the anode. The voltage between each dynode is regulated through a resistor chain that ends at the

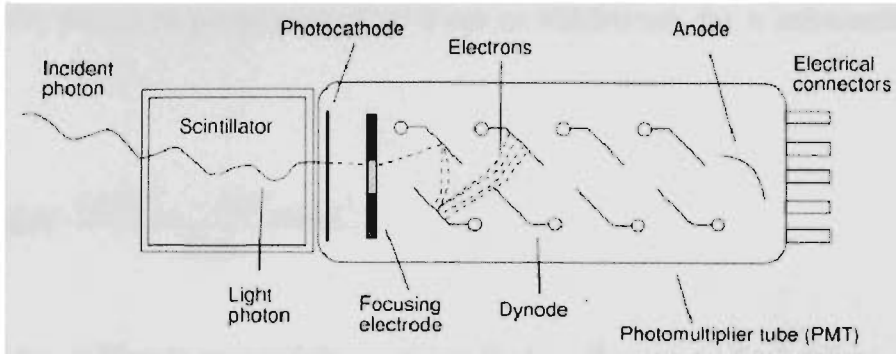anode, which will collect the resulting avalanche of electrons and convert these electrons into a signal.

Figure 20: The internal schematic of a PMT. [33]

6.2.2 Calibration

A calibration of both the inner and outer hodoscopes was done for each photomultiplier. Each detector assembly undergoes the calibration procedure to obtain the necessary parameters, to ensure the detectors' correct behavior. The technique involved properly identifying the pedestal and the first peak. The pedestal is the ADC response in the absence of any signals. This is an offset value that is determined and then subtracted off to obtain the corrected value of the signal corresponding to the energy deposited. The following peak is associated with that of a minimum ionizing particle. The shape of the peak follows a Landau distribution as was earlier discussed in Section 3.1.2. The gain is defined as the measured number of ADC channels associated with the difference between the pedestal and the first peak. Once the calibration was properly obtained for each PMT in the hodoscopes configuration, then the

energy deposited can be obtained. The correct energy deposition in the Outer Hodoscopes is calibrated with knowledge of the plastic's mean stopping power of 4 MeV, which is proportional to 2 cm in thickness, for a minimum ionizing pion.

$$\Delta E = 4\text{MeV} \cdot \frac{(ADC_{raw} - ADC_{Pedestal})}{Gain} \qquad (15)$$

This same calibration procedure is applied to the inner hodoscope, where the plastic bars were 0.5 cm in thickness. The expectation in an energy deposition is in the range of 1 MeV, for a minimum ionizing pion, to approximately 11 MeV, and possibly higher for low momentum protons. A simultaneous determination of momentum p and ΔE allows for an identification of the particle.
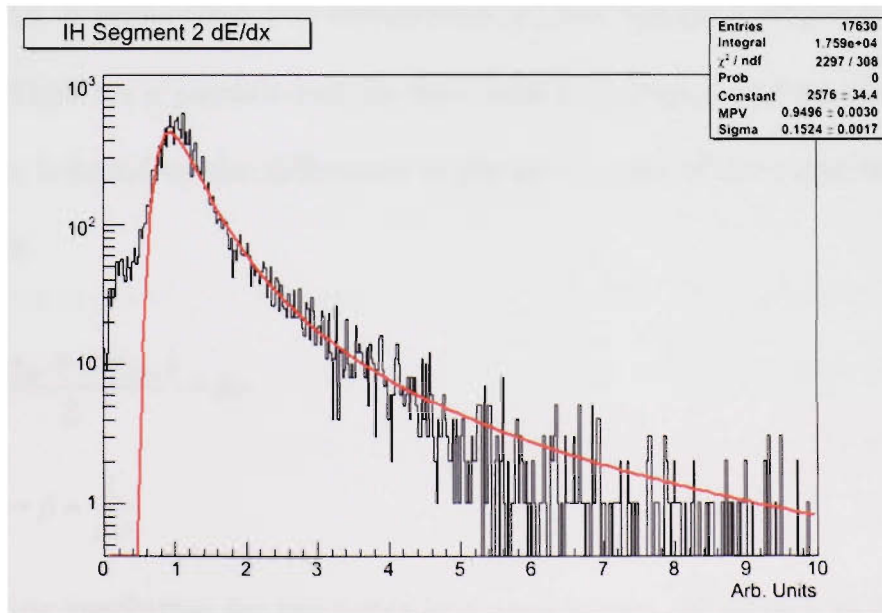

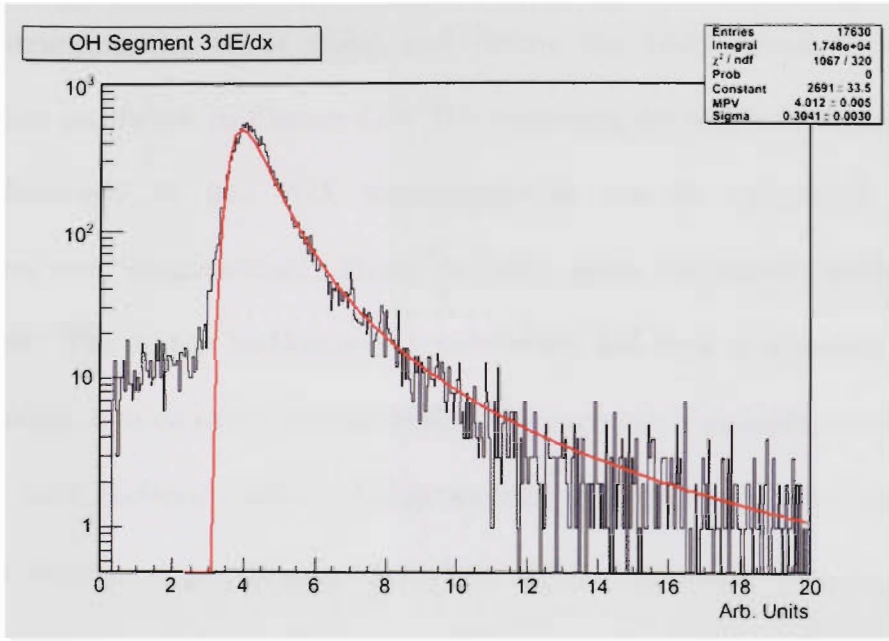Figure 21a: Calibrated energy deposit of pions for segment IH-3

45

Figure 21b: Calibrated energy deposit of pions for segment OH-3.

6.3. Time of Flight (*TOF*)

Time of flight measurements allow for a particle's mass to be determined by knowledge of flight time, the momentum $|\vec{p}|$, and the path length L [19]. The time of flight for a particle exiting the inner hodoscopes and passing through the outer is found by the difference of the mean time of the outer with that of the inner:

$$\Delta t = \frac{(t_{OH_{up}} + t_{OH_{dwn}})}{2} - t_{IH} \tag{16}$$

$$\Delta t = \frac{L}{\beta c} \rightarrow \beta = \frac{L}{\Delta t c} \tag{17}$$

The timing resolution for the outer hodoscopes was calculated by finding the offset values of the TDC distribution, for the each PMT attached to a bar,

then subtracting the offset time, and fitting the final result to a normal distribution as shown in Figure 22.b The standard deviation is the resolution of the detectors in ns. TOF measurements can be enhanced, if some corrections are implemented. These include, most commonly, pulse height corrections. The inner hodoscope signals were fed into a constant fraction discriminator as a counter to time-walk. The correction procedure was to plot the ADC information, resolve the mean and pedestal value for each PMT. This was discussed previously in section 6.2.2. Following this, a plot was generated of the pedestal subtracted ADC versus that of the TDC. This plot was then fitted to determine the corrected time from the fitting parameters p_1, p_2, and p_3. The corrected time is found by subtracting t' from the raw TDC, where

$$t' = \frac{p_1}{\left| ADC - p_2 \right|} - p_3.$$ (18)

The time difference (ΔT_{LR}) between the IH left and IH right is related to the coincidence of a two-pion event. The resolution, which is simply a detectors' ability to differentiate between signals arising from different particles hitting the detectors in small time differences, was determined to be 359 ps for ΔT_{LR}.
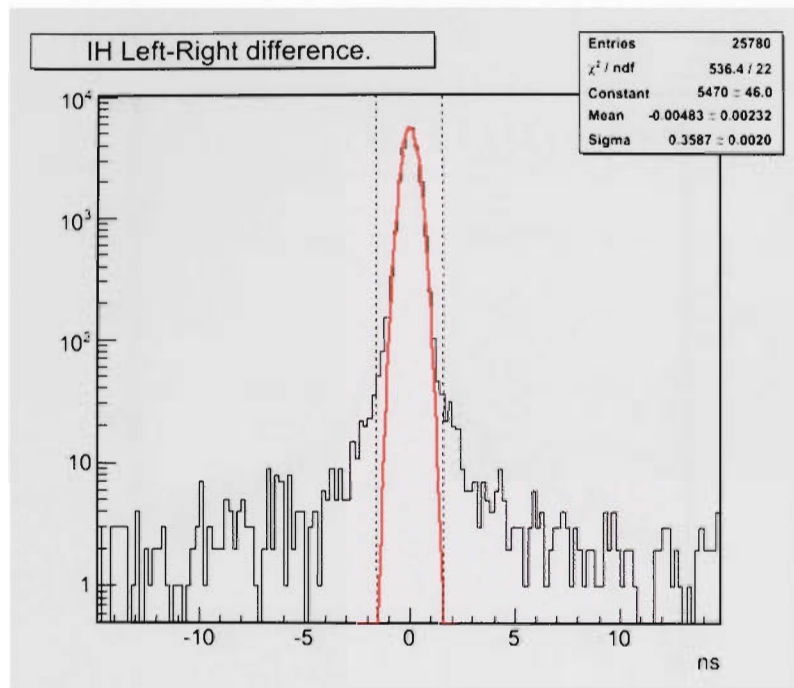
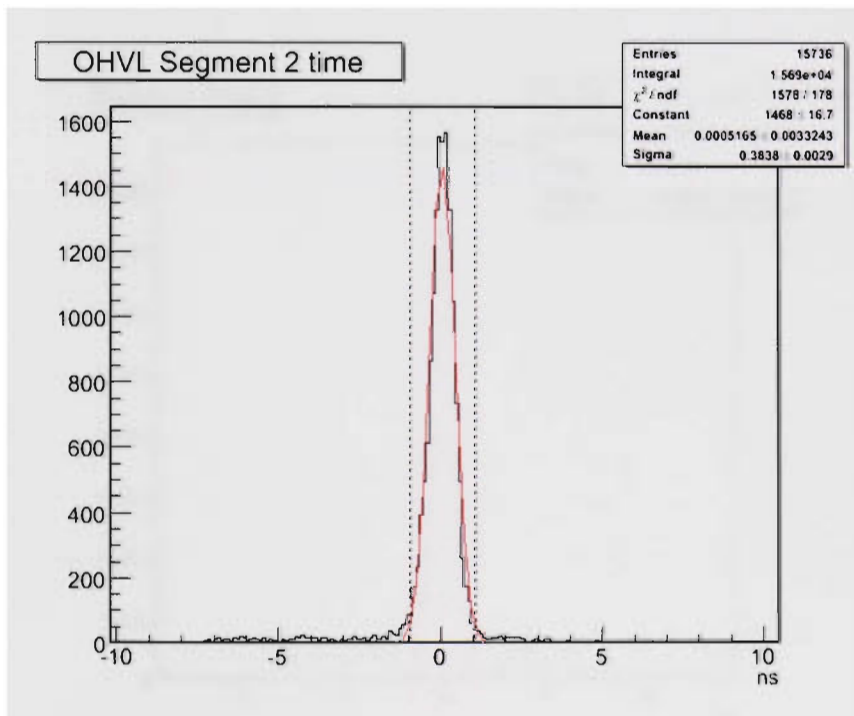Figure 22.a: IH ΔT_{LR} time resolution of segment 2R & 2L

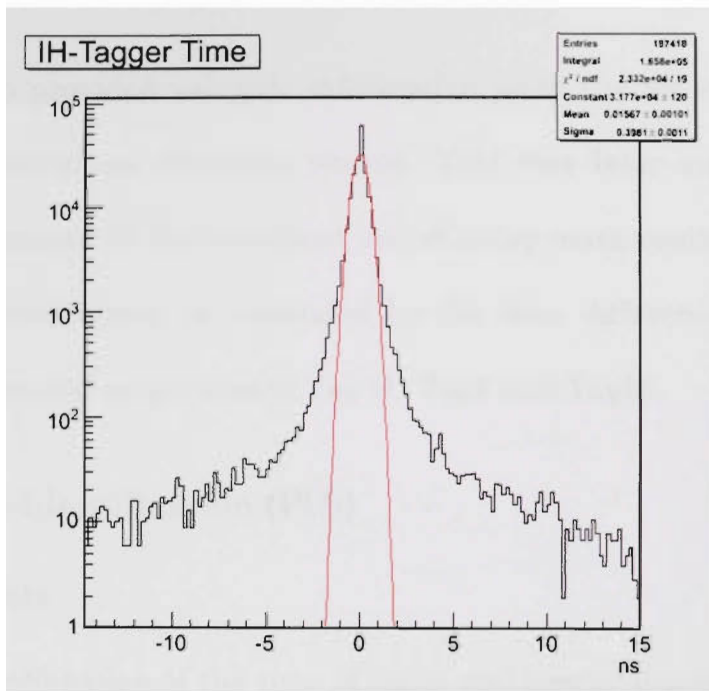Figure 22.b: Time resolution of 384 ps for OHVL segment 2.

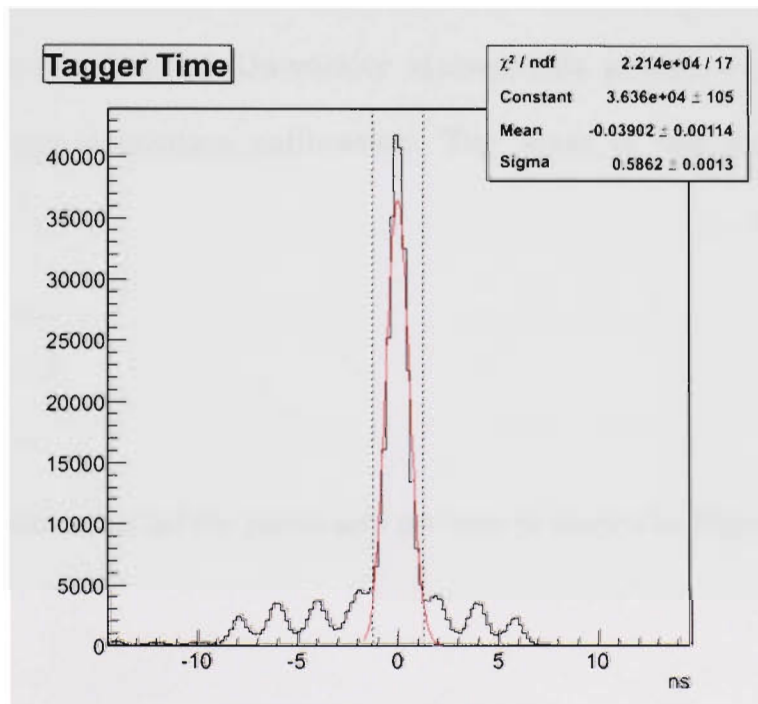Figure 22.c Timing resolution of IH-Tag H (B&F) of 399 ps

Figure 22.d Tagger time acceptance resolution.

The tagger also provided valuable information as to the coincidence of pion events with that of an incoming photon. This was later employed as an additional parameter in the invariant and missing mass reconstruction. The tagger timing coincidence is calculated by the time difference between the inner hodoscopes and mean time of Tag H (TagF and TagB).

6.4   Particle Identification (PID)

6.4.1 Hard Cuts

Following the calibration of the time of flight and energy deposition data, the appropriate cuts were determined to optimize the correct identification and separation of the protons from pions. The time of flight calibrations were conducted by the Tohoku University strangeness group, we performed a separate energy deposition calibration. The mass of the particle can be calculated as

$$m_{\pi,p} = |p|\sqrt{\frac{1}{\beta^2} - 1}. \tag{19}$$

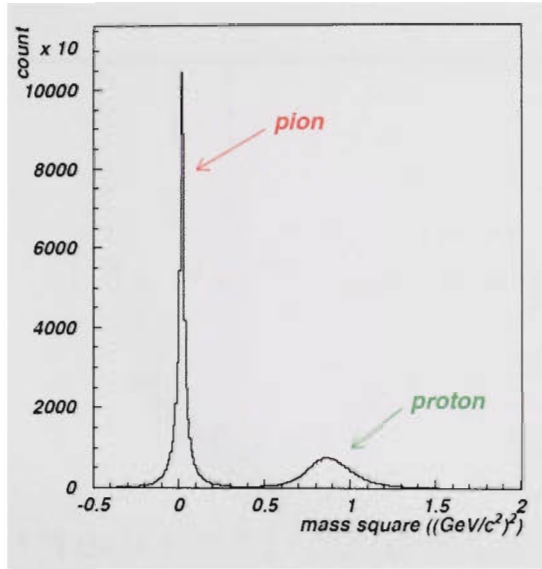A generic spectrum of m² for pions and protons is shown in Figure 23.

Figure 23: M² spectrum

Firstly, a hard cut was determined for energy deposition. The procedure involved plotting dE/dx vs. momentum as in Figure 24.a, then a small momentum region was selected, as the appropriate hard cut area, to separate pions from protons, see Figure 24.b Next, a "light" wide mass cut was determined; this was equivalent to making a hard cut on the momentum, for a fixed β, from the relation $m = |p|\sqrt{\dfrac{1}{\beta^2} - 1}$. Hard cuts were placed on velocity β from looking at a plot of momentum versus inverse beta and by the use of,

$$\beta = \frac{p}{E} = \frac{p}{\sqrt{m^2 + p^2}} \tag{20}$$

The cut on the range of β, a narrow mass cut, is used to extract a pion mass range of 0.1- 0.6 GeV/c² and 0.6-1.5 GeV/c² for the proton. Lastly, a flight time below 5.5 ns was used for pion identification.

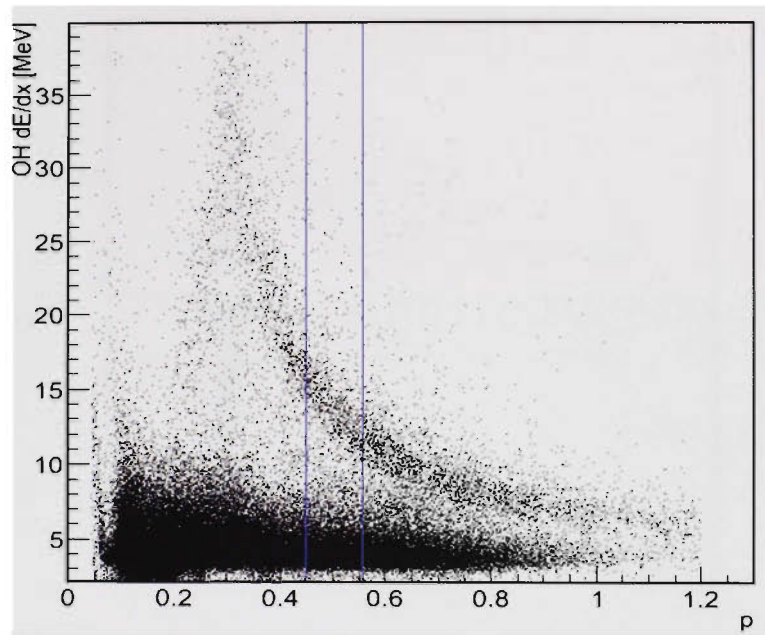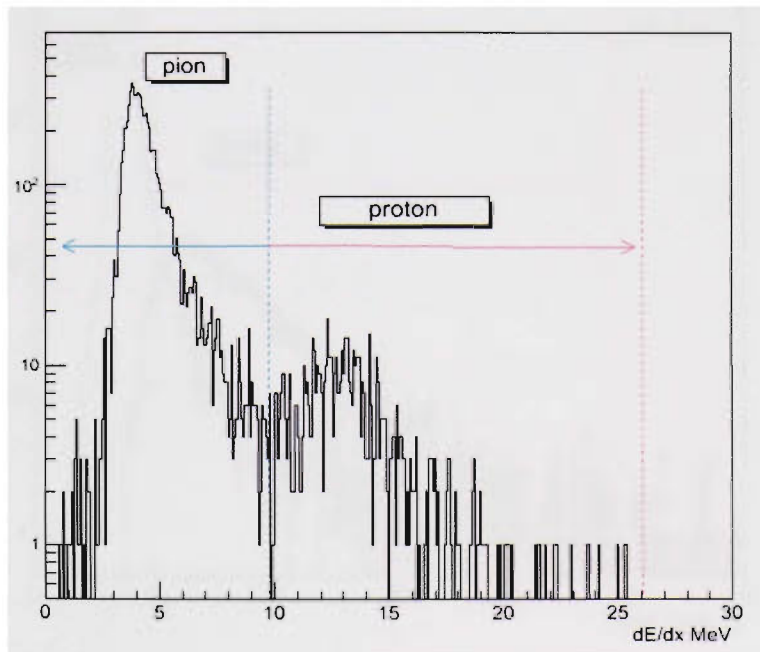Figure 24.a: dE/dx cut for $.45 < |p| < .55$ MeV

Figure 24.b: Momentum range $0.45 < |p| < 0.55$ MeV for dE/dx cut.
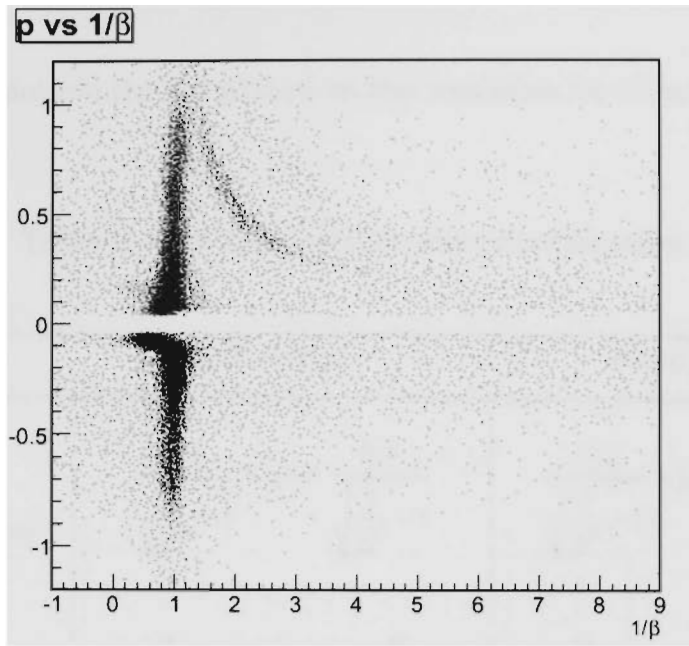
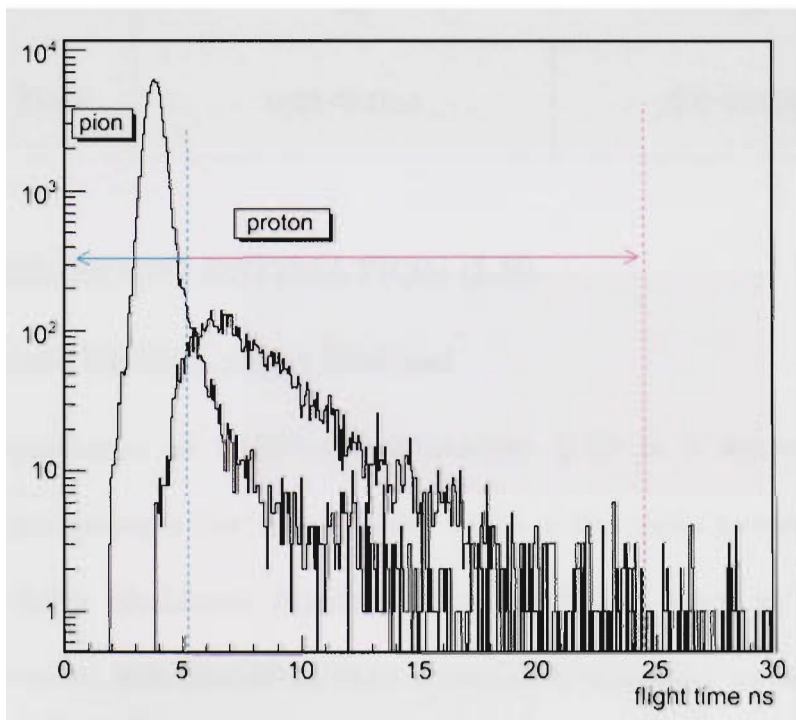Figure 25: Momentum (p) times charge vs. inverse speed ($1/\beta$)

Figure 26: Flight time cut for pion proton separation cut

Table 6 list in details the cut placed on the variables for either proton or pion selections.

Table 6: Listing of cuts for pion identification

Variable	Pion Cut	Proton Cut.
p (Wide mass cut)	$\dfrac{0.1}{\sqrt{\dfrac{1}{\beta^2}-1}} < \left| p \right| \le \dfrac{0.5}{\sqrt{\dfrac{1}{\beta^2}-1}}$	$\dfrac{0.6}{\sqrt{\dfrac{1}{\beta^2}-1}} < \left| p \right| \le \dfrac{1.1}{\sqrt{\dfrac{1}{\beta^2}-1}}$
β (Narrow mass cut)	$\dfrac{p}{\sqrt{0.6^2+p^2}} \le \beta \le \dfrac{p}{\sqrt{0.01^2+p^2}}$	$\dfrac{p}{\sqrt{1.5^2+p^2}} \le \beta \le \dfrac{p}{\sqrt{0.6^2+p^2}}$
dE/dx	$0.0\ \text{MeV} < \dfrac{dE}{dx} \le 10\text{MeV}$	$10\ \text{MeV} < \dfrac{dE}{dx} \le 25\ \text{MeV}$
Flight Time	$0 < ft < 5.0\text{ns}$	$5.0 < ft < 20\text{ns}$

6.5   LIKELIHOOD ESTIMATION (LE)

6.5.1 Particle Identification Method

The implementation of likelihood estimation (LE) is a known statistical method to approximate the "most likely" value of the input parameters, using the probabilistic likelihood function. The method is used to identify, for individual events, the likelihood that a particle's identity corresponds to the known probability distribution. This is especially useful, in the case of an event that cannot be identified by a simple cut. The generation of the

probability distribution will follow the hard *PID* cuts, at the loss of statistics. After the creation of the probability density function, the hard cut conditions may simply be discarded. At this stage LE technique can be employed.

The Gaussian distribution is named in honor of Johan Carl Friedrich Gauss (1777-1855) and is also referred to as the normal distribution, known for its bell shape. This distribution follows

$$P_{\mu,\sigma}(x) = \frac{1}{\sigma\sqrt{2\pi}} \exp\left[-\frac{(x_i - \mu)^2}{2\sigma^2}\right]. \tag{21}$$

where σ, the width, is the standard deviation for the distribution, and an indication of the precision of a measurement. In essence, a smaller sigma indicates a more highly peaked distribution [34]. This distribution is a function that approximates the exact binomial distribution of events [34]. The Gaussian probability distribution is applied to many fields of scientific research.

The traditional hard cut technique at this point would be to plot the energy deposition, time of flight distribution, and momentum distribution and then make a hard cut, possibly at the mid-point of the overlap of the distribution corresponding to different particles. Or, if there is an emphasis on correctly identifying one particle of interest, which in the case of this experiment, is the pion, one could make at minimum a one or two sigma cut.

This, however, will allow for the contamination of background resulting from the inclusion of the other particle or the loss of valuable statistics.

The proposed statistical solution would be to replace the conventional PID approaches by the use of Likelihood Estimation (LE). The LE method is applicable at this point as a result of the known theoretical distributions, either being Gaussian or Landau, for a sample of independent events, achieved after hard cuts [20]. It works under the principle that if the theoretical normal distributions are known, then so is the mean and sigma. This is significantly different than the Maximum Likelihood Method, in which one attempts to estimate both the standard deviation, and true value X, found at the maximum. Here, one attempts to determine the probability that a set of values $x_1, x_2, x_i \ldots x_N$ belongs to known distributions of which the mean and sigma are known. For a gaussian distribution the likelihood function is

$$L(TOF \mid \pi) = \frac{1}{\sigma_\pi \sqrt{2\pi}} \exp\left[-\frac{(x_i - \mu_\pi)^2}{2\sigma_\pi^2} \right]. \tag{22}$$

Therefore, after application of the hard cuts, the generated distributions can be fitted and the mean and standard deviation arrived upon for each type of particle. The technique will be to calculate the probability for the same event that corresponds to both the dE/dx and TOF distributions. Hence, one can compute the probability of the particle's identity, by finding the probability

for each $x_1, x_2, x_i .....x_N$, of it being a pion or proton for the energy deposition distribution and simultaneously determining the probability for the same x_i of it being a pion or proton for the time of flight distribution. Thus, the total likelihoods are givens as products:

$$L(\pi) = L(dE \mid \pi) \cdot L(TOF \mid \pi)$$ (23)

and for the proton the likelihood is:

$$L(p) = L(dE \mid p) \cdot L(TOF \mid p)$$ (24)

These are normalized to one by

$$N_{L(\pi)} = \frac{L(\pi)}{L(p) + L(\pi)}.$$ (25)

The particle identity is then assigned based of the resulting highest likelihood. This was used as the lone identification cut when later reconstructing the invariant and missing mass of the reaction, in an attempt to compare the statistics versus the conventional hard cuts. To illustrate the technique, in Figures 27.a, 27.b, and 28 a single event is shown in red with corresponding value in dE/dx of the OH, and IH, and time of flight distribution. The goal is to correctly identify, with the highest probability, as to which particle type the event should be assigned . The pink and turquoise

dashed lines depict the typical hard cut regions. In Section 8 a comparison of PID cuts will be further discussed.
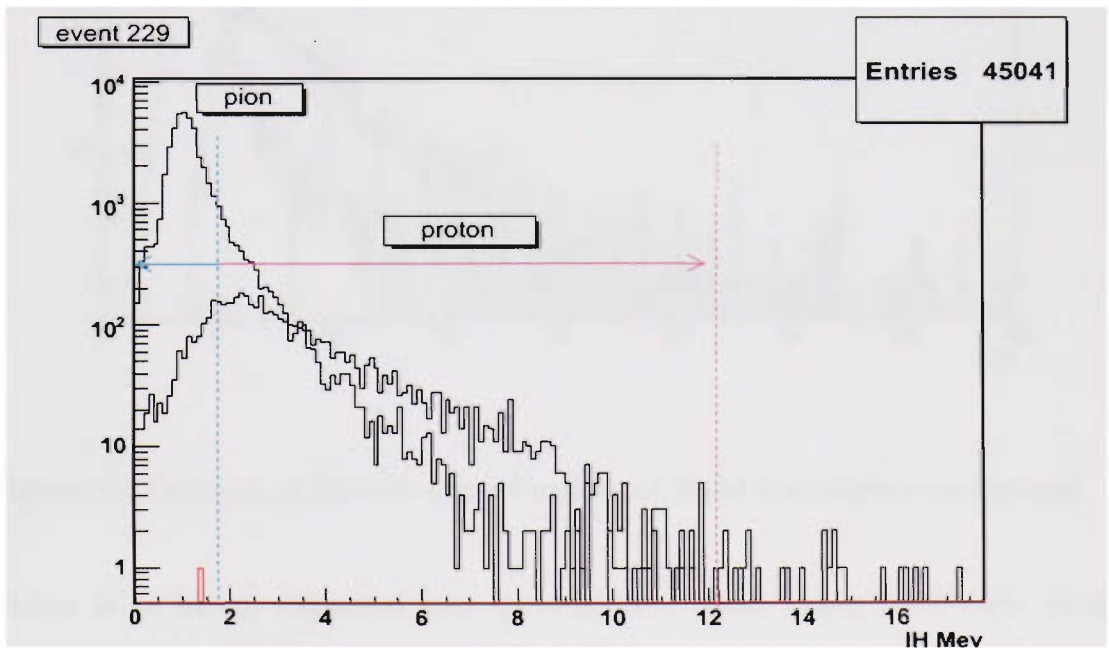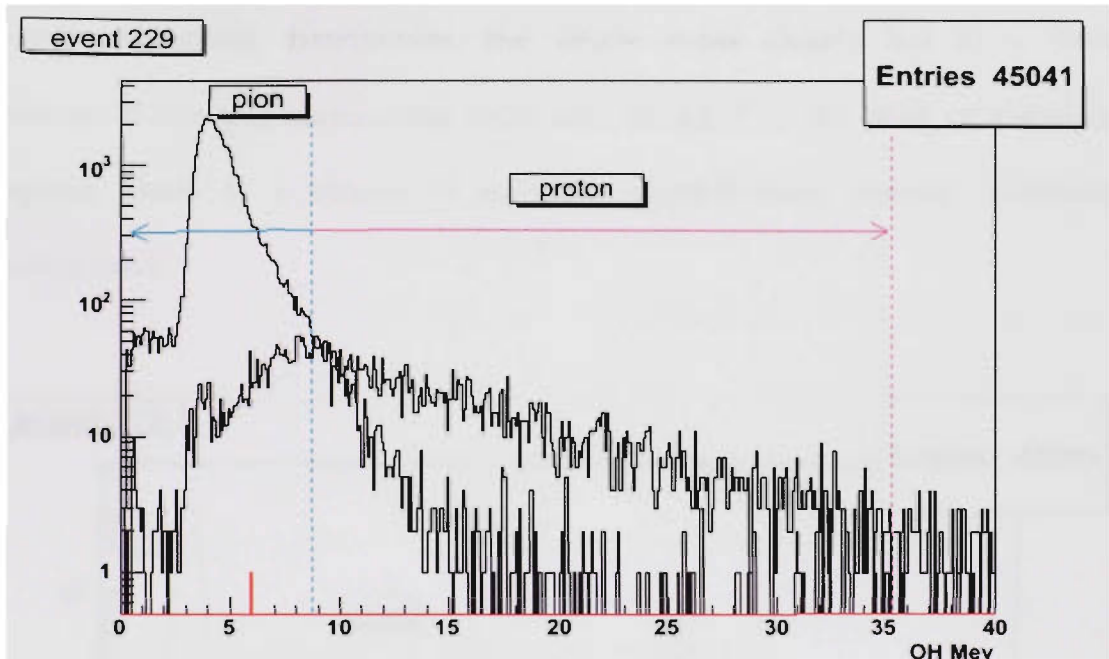
Figures 27.a and 27.b: Overlap of distributions for energy depositions for single event in red.

Figures 27.a, 27.b, and 28 help to clarify the reason for the interest in the use of likelihood as an alternative PID method. In both time of flight and energy deposition distribution, the single event clearly lies in a direct overlap, if one implements the hard cuts depicted in the pink or turquoise regions, there is a chance of incorrect identification directly increasing background.
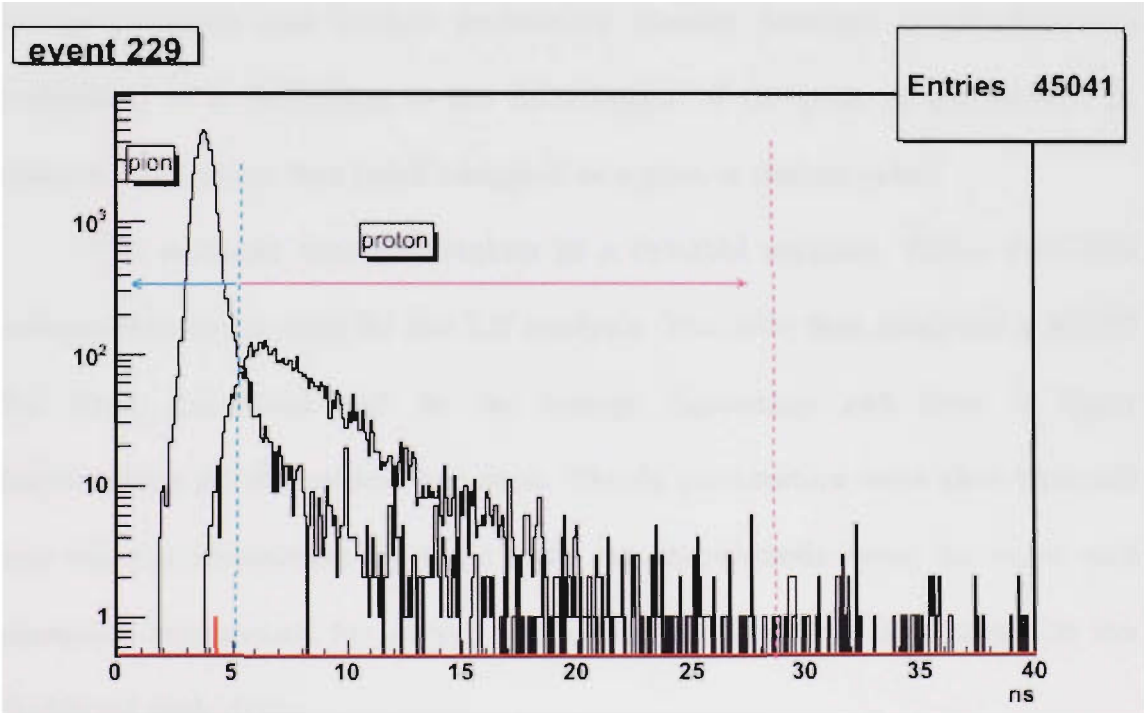

Figure 28. Overlap of distributions for time of flight for single event in red.

There is to be an expected loss in statistics when using hard cuts. If the individual event in red truly belongs to the pion distribution, but is discarded due to the hard cut, then the physics of interest is lost.

6.5.2 Likelihood Estimation Code

The goal of likelihood estimation method for particle identification, is to correctly determine a particle's identity with a significant increase in statistics. As such, a code was written to verify the usefulness of the technique. The mean and standard deviations were determined by fitting the distributions yielded as a result of flight time and dE/dx hard cuts. This is a necessary step in the method. For each event number, the x_i were evaluated by the gaussian and landau probability density function to calculate the probability of it belonging to the distribution of the pion or the proton. In essence, each event was itself assigned as a pion or proton event.

The analysis was undertaken in a two-fold manner. There were two independent codes used for the LE analysis. The code first analyzed a ROOT file, then generated and fit the energy deposition and time of flight distributions for the proton and pion. The fit parameters were then inserted into the complementary analysis code, which proceeds event by event and generates histograms for energy deposition and time of flight based on the likelihood probability.

A secondary code was written to perform the same procedure. Upon event identification by the second likelihood code, an additional leaf in the ROOT tree file was created where the assigned identity of each event was filled, on which a cut could be specified as 1=pion and 2=proton. The energy deposition and time of flight distributions were then generated by placing a

cut on the newly created ROOT leaf, and also by the use of the conventional beta cut outlined in Section 6.4.1. The analysis was performed only on the yield of identified pion events. Alternatively, the probability value of each event could be filled into a probability distribution, and then the appropriate cut placed on said distribution. The preliminary results of this method as compared to the results obtained by conventional hard cuts as are discussed in Section 8.

7. RESULTS

7.1. Invariant Mass Reconstruction

In production experiments some of the particles of interest created have short lifetimes. As such, it may not be possible to identify these particles directly. Instead they are indentified by the particles they decay into. The use of the four-momentum vector approach as a kinematical description of neutral kaon's decay yields:

$$M_{K^0} = M\left(\pi^+\pi^-\right) = \sqrt{\left(\sqrt{\vec{p}_{\pi^+}^{\,2} + m_{\pi^+}^{\,2}} + \sqrt{\vec{p}_{\pi^-}^{\,2} + m_{\pi^-}^{\,2}}\right)^2 - \left(\vec{p}_{\pi^+} + \vec{p}_{\pi^-}\right)^2} \quad (26)$$

The method of pion identification follows the conditions in Table 4 of section 6.4.1. In addition to the use of one of these PID cuts, there were additional constraints established to generate the neutral kaon mass spectrum. These cuts are outlined in Table 7. The generation point for the kaon is depicted in Figure 29, where X_{VT} and Y_{VT} are the chosen coordinate system due to the offset in target position, which defines the center of the target as the origin [28]. The generation point is defined as g_x and g_y, measured from the target's origin and calculated as,

$$dlen = \frac{\vec{p}_K \cdot \vec{VT}}{p_K} \quad (27)$$

$$\vec{g} = \vec{VT} - dlen \cdot \frac{\vec{P}_K}{P_K} \quad (28)$$

$$R_{adius} = \sqrt{X_{VT}^2 + Y_{VT}^2} \quad (29)$$

The cuts in Table 7 allowed for the extraction of the K^0 invariant mass.

Table 7: List of cuts used to extract invariant mass.

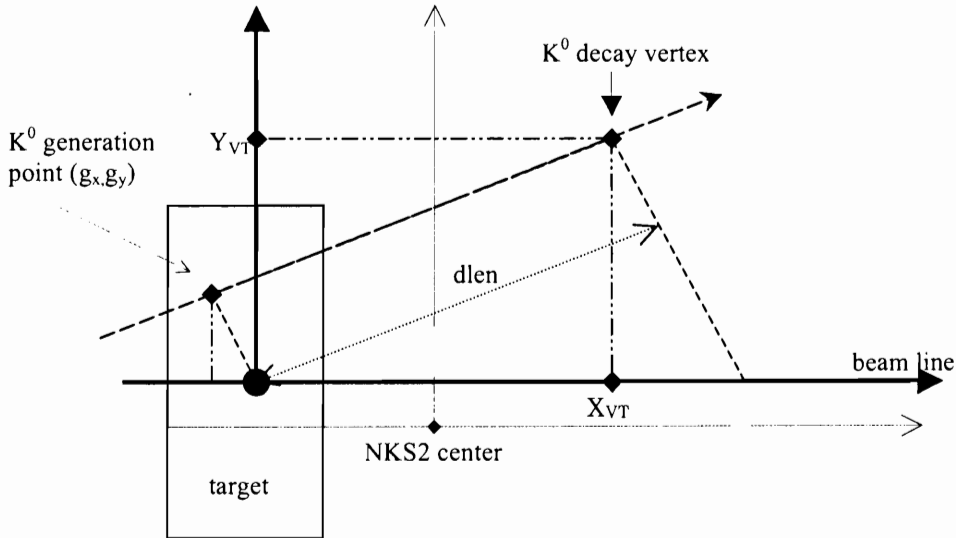| Variable	Hard Cut
Inside Vacuum chamber	Radius< 5.5 cm
Electron Veto	$-.9 < \cos\theta < .8$
Tagger Coincidence Time	$IH_{time}\text{-}Tag_{time} < 2ns$
Decay Volume Outside Target	$1.5cm < \|(X_{VT}\text{-}t_x), 3.0cm < \|(Y_{VT}\text{-}t_y)\|$
dlen	$5.5 > dlen > .8$ cm
Generation point.	$\|g_y\| < 1.8$ cm $\|g_x\| < 3$ cm

Figure 29: Schematic of K^0 generation point.

In the area of the target, there are many reactions occurring, resulting in the creation of particles that may not be of interest. The extraction of the kaon

was achieved by placing limitation on the pions that were selected for the kaon's reconstruction. The chance of pion and ρ production, the creation of nucleon resonances, along with other processes of non-interest, is distinctively high, thus only pions from vertices outside the target were selected. Figure 30 is a schematic of the target and decay regions inside the vacuum chamber; Figure 31 left is the $\pi+\pi$- invariant mass spectrum with and without region cuts in blue and black, respectively. The right shows the $\pi+\pi$- invariant mass with decay volume region cuts on a broad background, there is a narrow distribution located at 0.5 GeV/c^2 is associated with kaons.
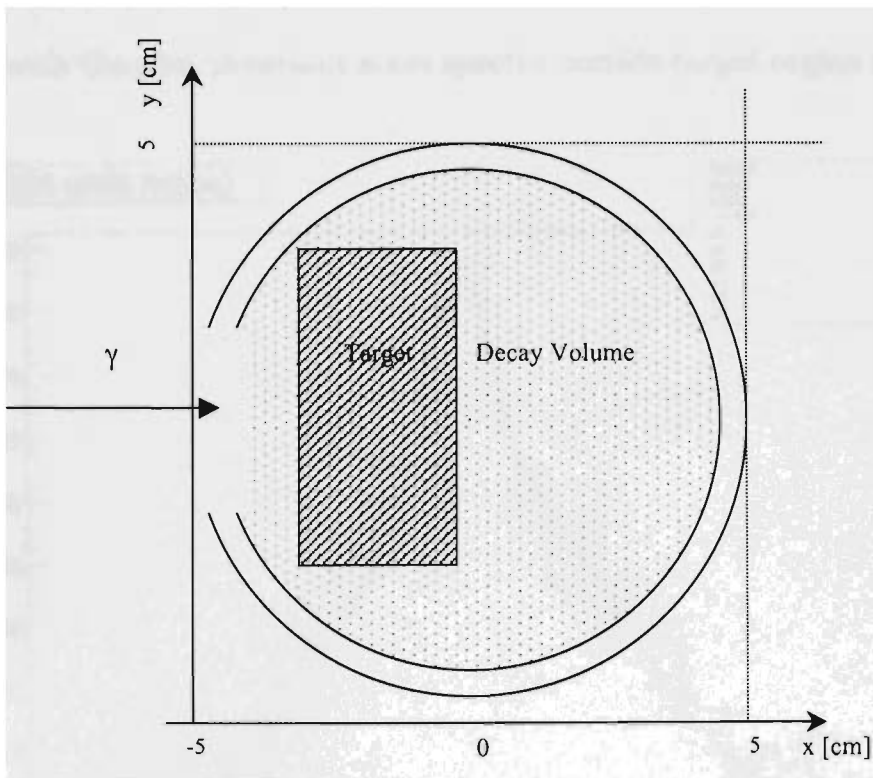

Figure 30: Decay Volume and Target area inside vacuum chamber.

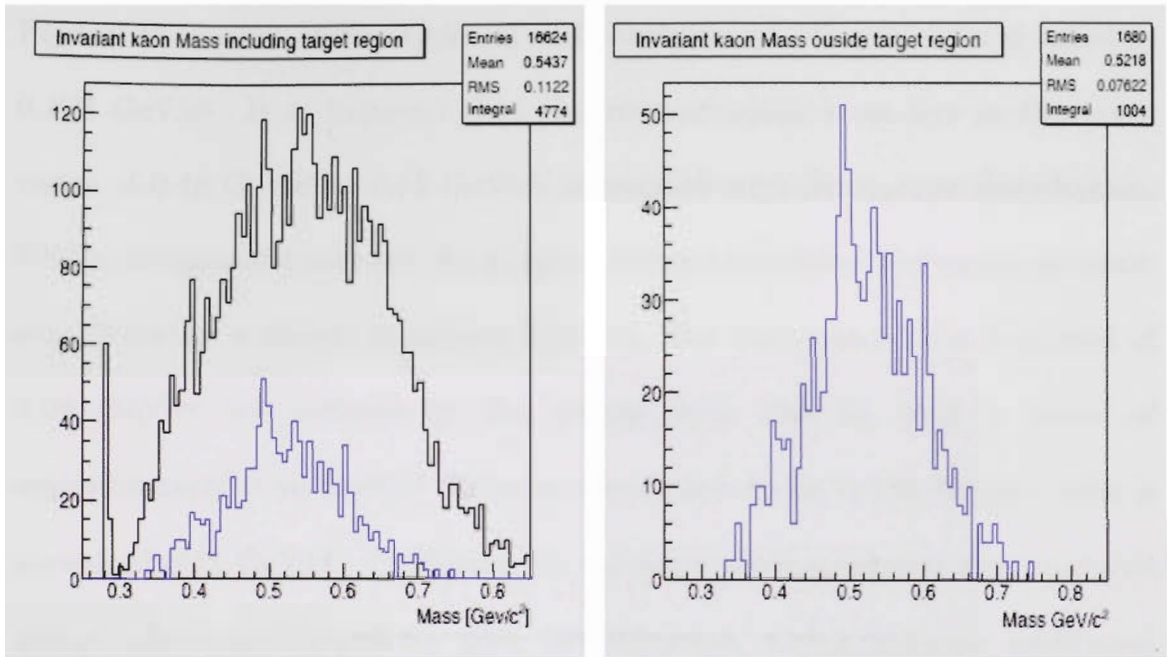Figure 31: The π+π- invariant mass spectrum including target region in black, with the π+π- invariant mass spectra outside target region in blue.
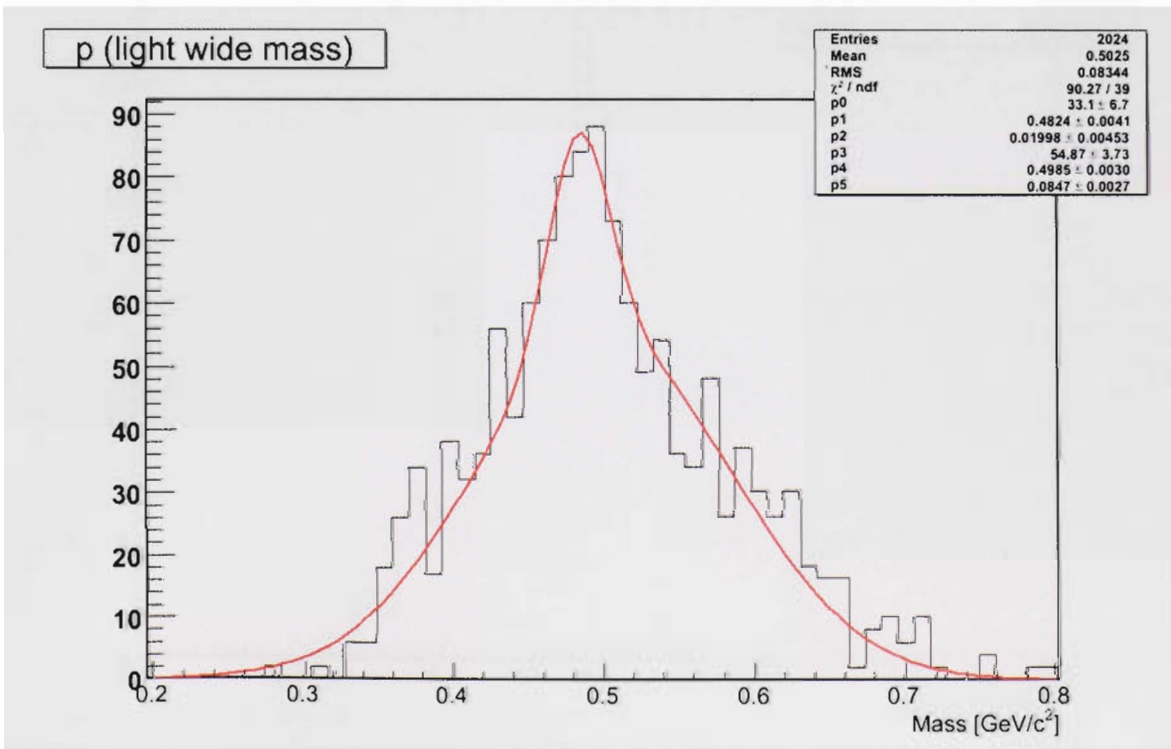

Figure 32: K^0 invariant mass generated from a momentum (wide mass) cut.

Figure 32 clearly shows there is still background. The true kaon mass is 0.497 GeV/c². It is believed that the reconstructed kaon lies in the mass range of 0.48 GeV/c² to 0.52 GeV/c², associated with the narrow distribution. This assumption motivated the adopted fitting procedure. The mass spectrum was fitted by a double gaussian function. The background has a spread of 0.08 GeV/c², as defined by the sigma from the fit, and a mean of approximately 0.50 GeV/c². Here it was found to be 0.483 GeV/c², with a spread of 0.02 GeV/c². In Figure 33, the kaon mass spectrum was produced using only a *dE/dx* cut for pion identification, which removed additional background and statistics as shown.
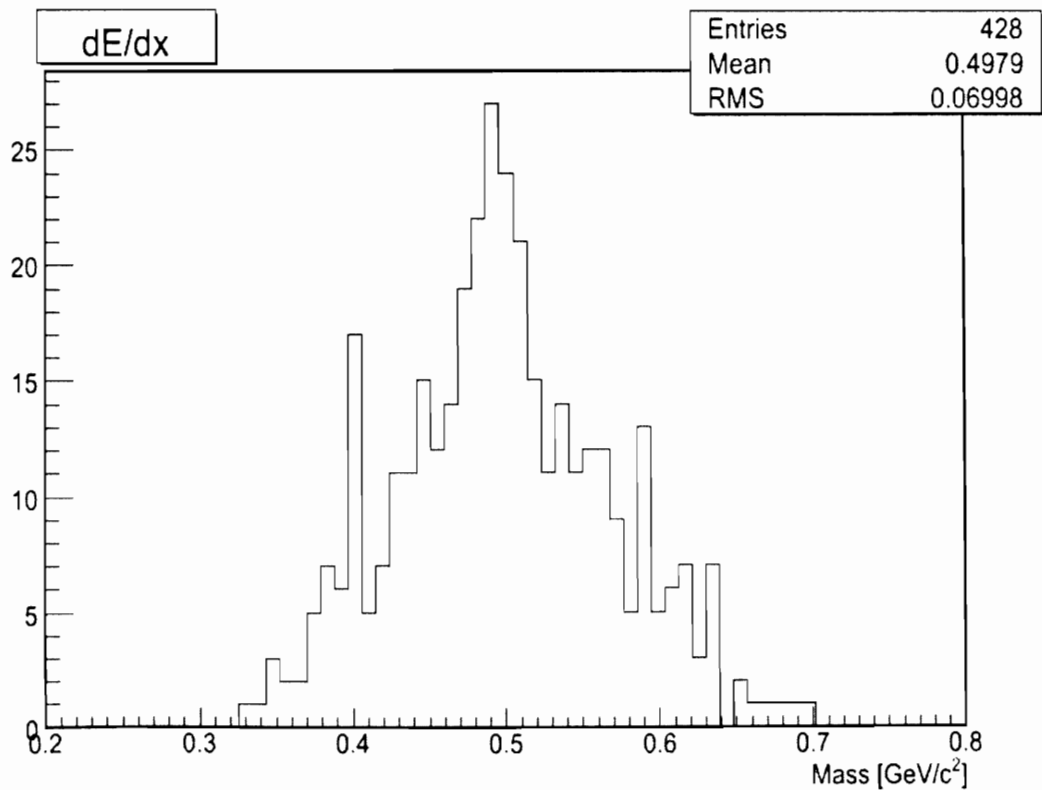

Figure 33: *K⁰* invariant mass with energy deposition cut applied.

The investigation into the PID efficiency was correlated to counts of the mass spectrum. As stated previously and shown in Figure 30, not all events that are in the kaon mass spectrum are believed to really be kaons, but for this analysis, all events will be taken into consideration. The analysis of individual runs was completed with difficulty as a result of the low statistics. A second analysis was undertaken linking runs in groups of the same kinematical origin. A brief investigation of the photon energy effect on kaon events was also undertaken. Figure 34 shows the $\pi^+\pi^-$ invariant mass spectrum for different incoming photon energy. The ranges in $E\gamma$ were $E\gamma_1$: $0.9 < E\gamma < 1.1$, $E\gamma_2$: $1.0 < E\gamma < 1.1$, $E\gamma_3$: $0.9 < E\gamma < 1.0$ and $E\gamma_4$: $0.8 < E\gamma < 0.95$ GeV.
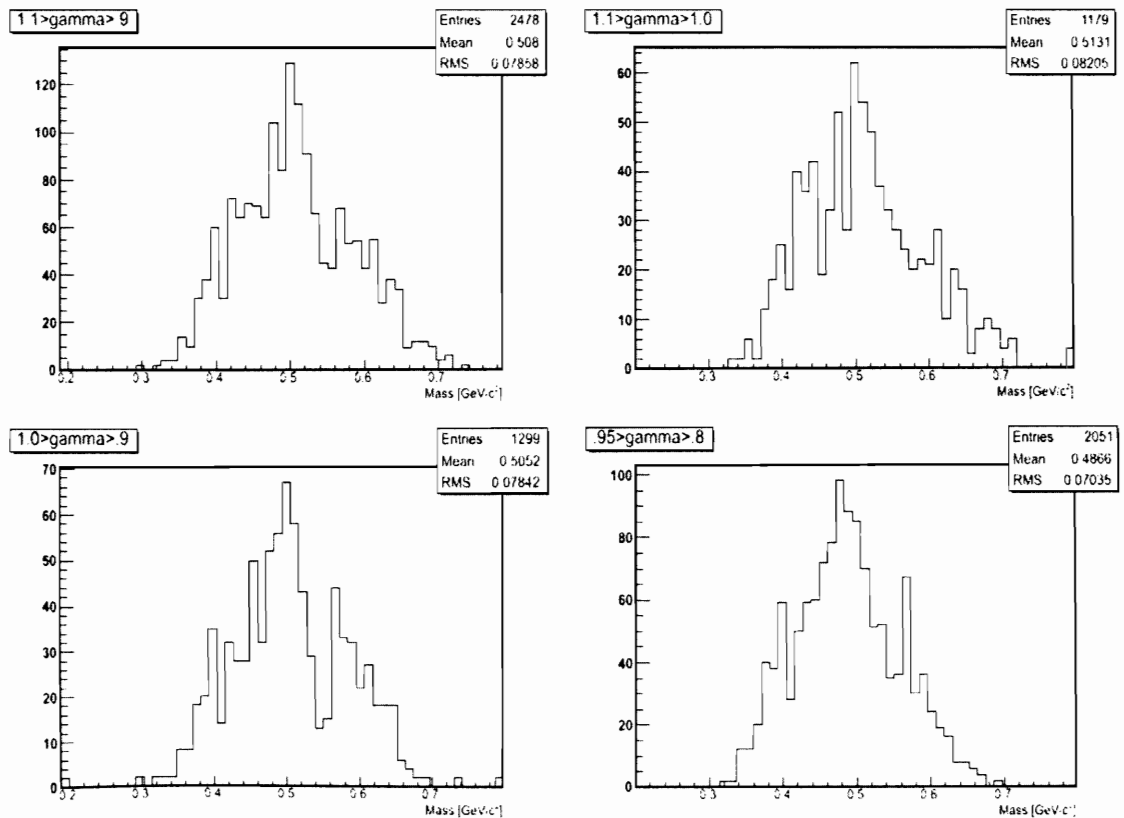

Figure 34: $\pi^+\pi^-$ invariant mass spectrum for different photon beam energy.

7.2 Missing Mass

The reconstruction of the missing mass measured from the $d(\gamma, K^0)\Lambda p$ reaction is expected to be that of a two body final state, where the proton is a spectator particle in the kaon production reaction. As was detailed earlier in the kinematics section, the use of four-momentum vectors is used in the calculations. In four momentum notation the reaction can be written as:

$$\gamma + D = K^0 + X. \tag{30}$$

Thus, the square of four momentum of the unobserved final states is

$$X^2 = M_x^2 = \left(\gamma + D - K^0\right)^2 \tag{31}$$

when expressed in terms of measured quantities,

$$M^2_{(p+\Lambda)} = M_x^2 = \left(E_\gamma + M_d - E_{K^0}\right)^2 - \left(\vec{p}_\gamma - \vec{p}_{K^0}\right)^2 \tag{32}$$

The neutral lambda should be produced along with a neutral kaon. Figure 35 is the missing mass of just an individual run. The lambda's mass is 1115.68 MeV/c^2, and has a lifetime of approximately $c\tau$ = 7.89 cm. The threshold of missing mass for a final state consisting of a proton and a lambda should be at 2.05 GeV/c^2. However, the missing mass spectrums were found to have a threshold of approximately 1.9 GeV/c^2. The reconstructed kaon mass was approximately 0.482 GeV/c^2 with a spread in the distribution on the order of 20 MeV, indicating a lack of precise momentum calibrations.
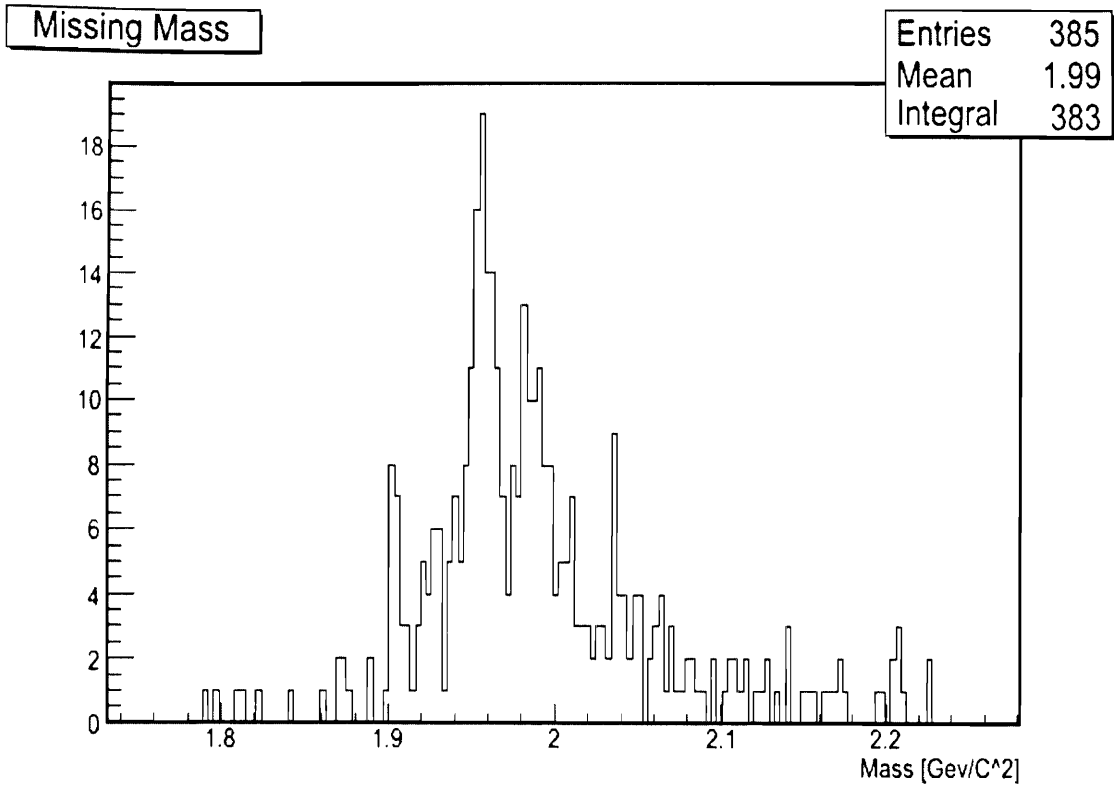
Figure 35: Missing mass for an individual run

The kaon momentum was used in the missing mass calculation as shown in Equation 32. Thus, the spread and imperfect momentum calibration was most likely propagated into missing mass calculation, in order to account for the loss of roughly 100 MeV. A cut on the reconstructed kaon mass, 0.48 GeV/c^2 to 0.50 GeV/c^2, was also included, however as in Figure 30, there remains a large background. As was previously discussed in the analysis of the neutral kaon invariant mass, the statistics were extremely low when conducting the analysis on an individual run, especially as a consequence of the many hard condition limitations enacted to resolve the kaon, and the

additional cut now placed on the kaon mass to reduce propagating background in the calculated Λp missing mass. The low yield in the analysis of a single run was the same for the final state proton and lambda missing mass. Figure 36 illustrates a clearer missing mass when obtained from grouped runs.
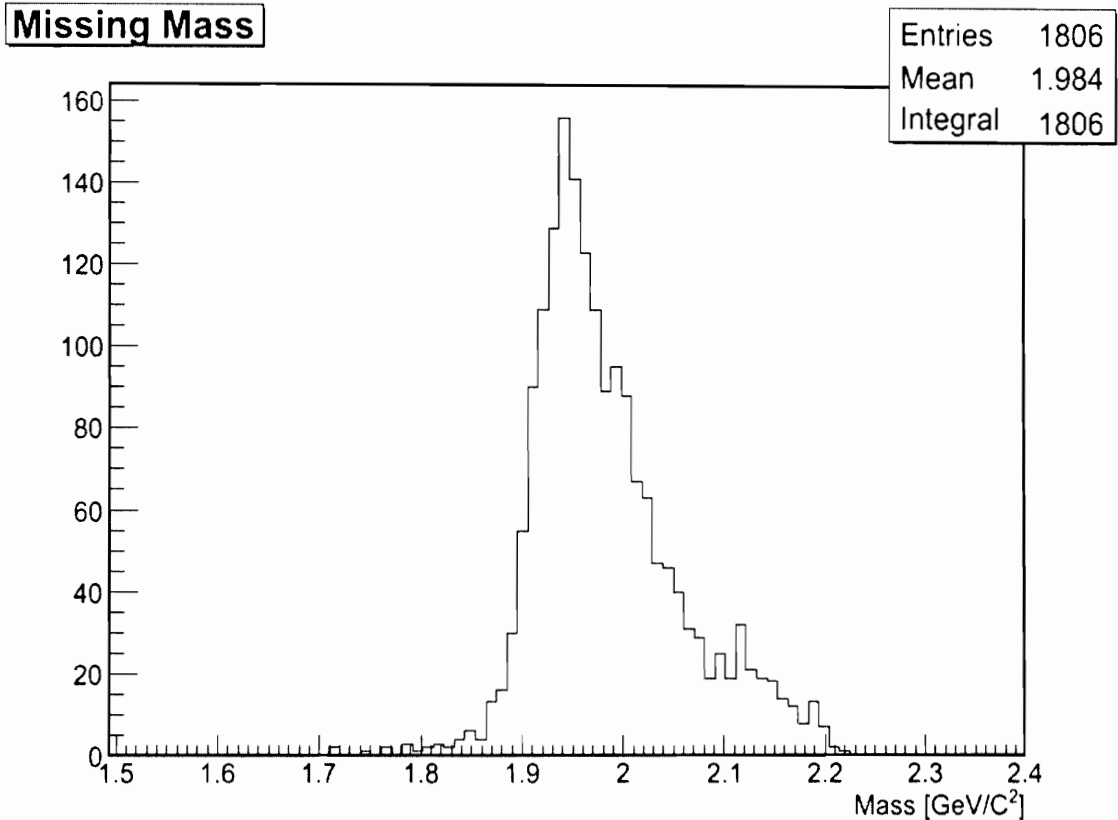

Figure 36: Proton and lambda missing mass for grouped runs with a wide mass cut on momentum, and a narrow cut on the reconstructed kaon mass.

8.   DISCUSSION and CONCLUSIONS

8.1   Traditional PID

Each method of particle identification has been demonstrated to be successful. A further goal was to compare their varied strengths. The approach was to compare the kaon event yield for each PID approach. The PIDs (1-4) are a light (wide mass) cut, a beta (narrow mass) cut, a dE/dx cut, and a combination of dE/dx and flight time cut, respectively, and were outlined in Table 6. The invariant mass was reconstructed for each run by applying the cuts discussed in section 7.1 while changing only the approach used for pion selection. At first, an analysis was completed on individual runs, but the hard cuts led to very little statistics such that fitting became moot. To increase the rationality of the comparison method, groups of runs of the same kinematical specifications were analyzed. The statistics available for the reconstruction of the kaon mass was evaluated for different PID methods. Figure 37 shows the generated mass spectrums that were produced for a specific PID method. As in Figure 32, the distributions were fitted with a double gaussian in order to extract the individual strengths for the kaon and background distributions. The total double gaussian fit is displayed in red, the background distribution follows the dashed green fit, and the kaon strength is shown in solid black. The kaon strength is shown with the background subtracted.

p (light wide mass)
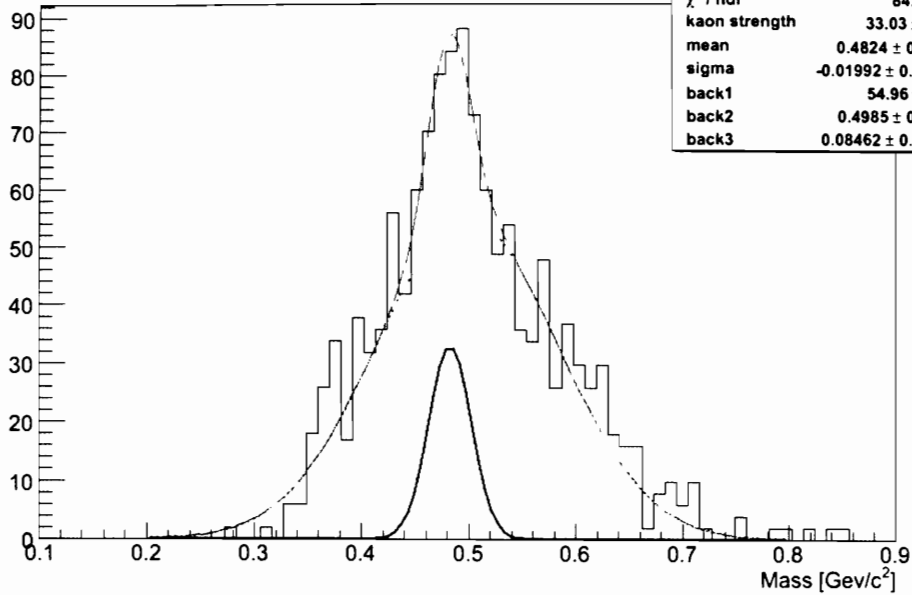
Entries	2024
Overflow	722
χ^2 / ndf	84.4 / 36
kaon strength	33.03 ± 6.67
mean	0.4824 ± 0.0042
sigma	-0.01992 ± 0.00451
back1	54.96 ± 3.71
back2	0.4985 ± 0.0030
back3	0.08462 ± 0.00271

β (narrow mass) cut
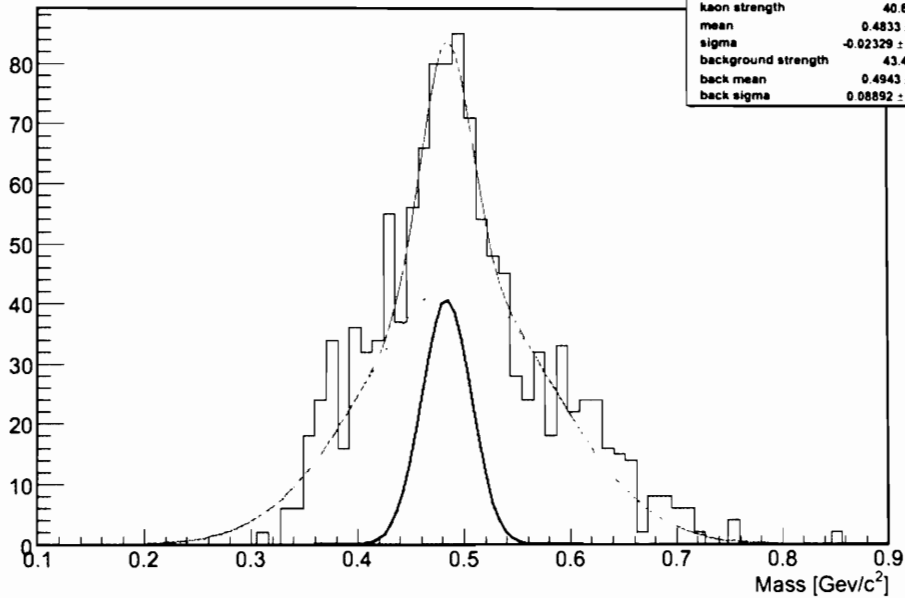
Entries	1869
Overflow	696
χ^2 / ndf	80.42 / 33
kaon strength	40.69 ± 6.17
mean	0.4833 ± 0.0035
sigma	-0.02329 ± 0.00438
background strength	43.45 ± 3.97
back mean	0.4943 ± 0.0036
back sigma	0.08892 ± 0.00379

Figures 37.a & 37.b: Kaon mass reconstructed by indicated PID method, with background shown in green and kaon strength shown in black.
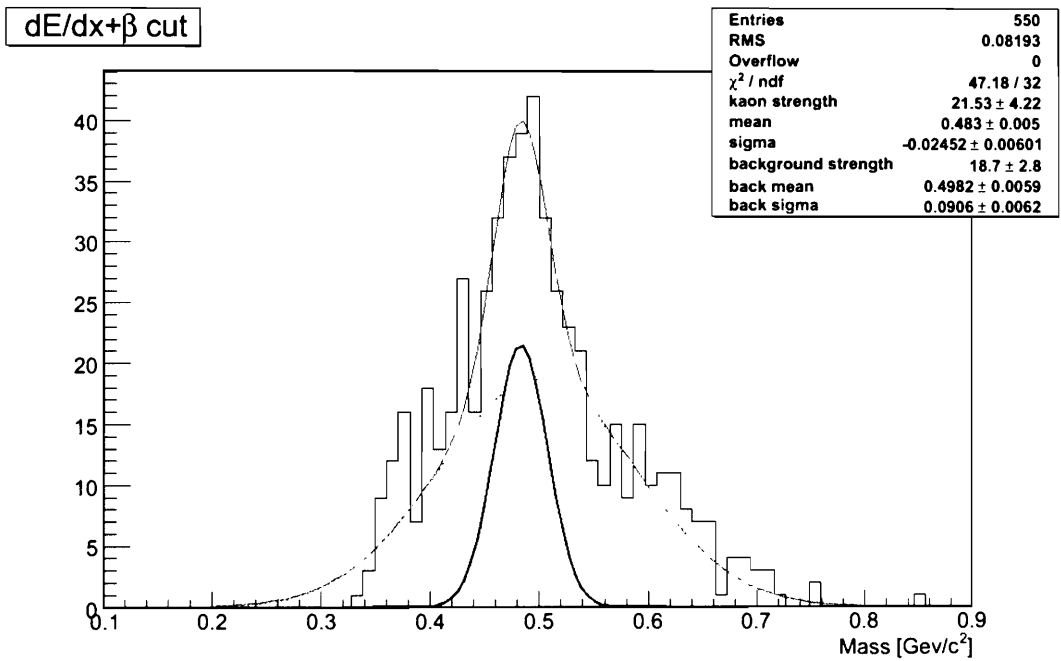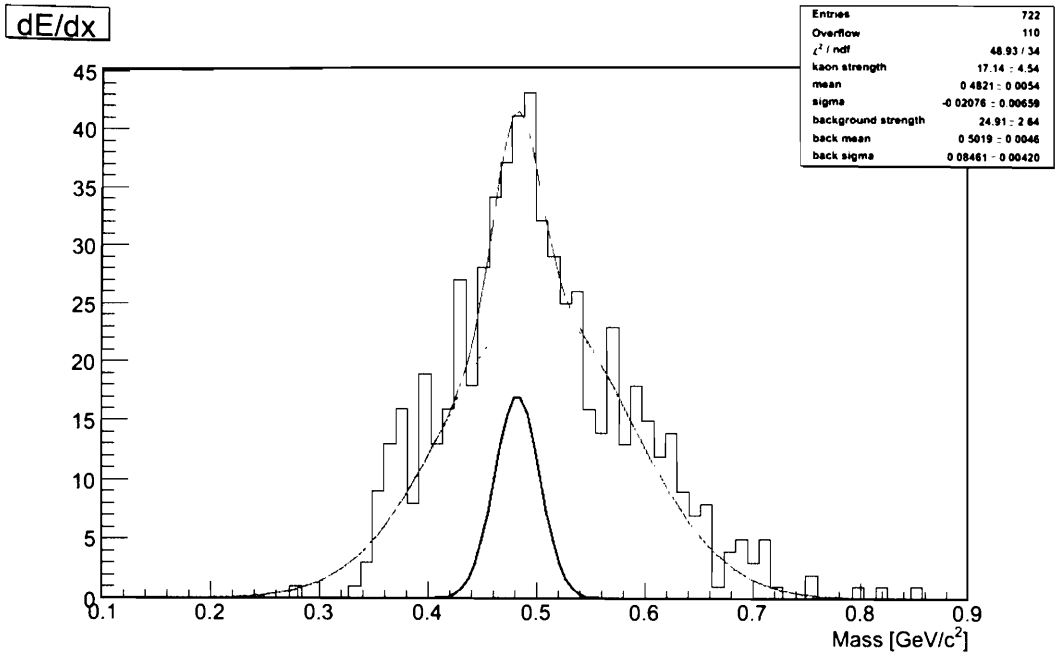
Figures 37.c: & 37.d: Kaon mass reconstructed by indicated PID method, with background shown in green and kaon strength shown in black.

Figure 38 illustrates the strength of each as a measure of the statistics available. The plot shows for each method of identification total number of events as a plotted point. The error on the value is simply the square root of the counts.
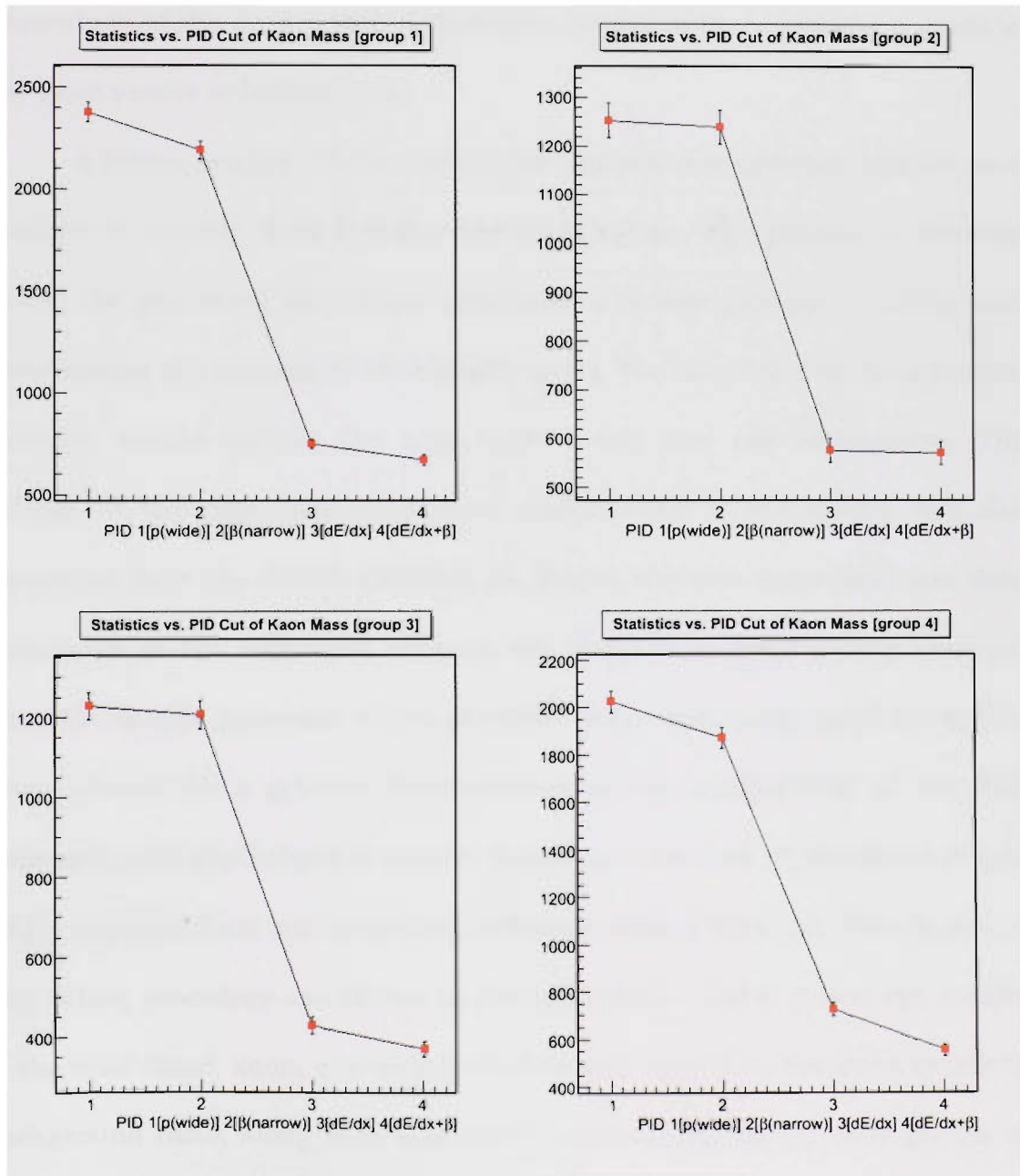

Figure 38: Counts vs PID method for generated $\pi^+\pi^-$ invariant mass.

The least statistical loss occurs with the application of only PID (1). The dE/dx cut and combination cut, PID (3) and (4), result the greatest loss amount of available statistics. This evidently shows the great deal of events that were also discarded. It is not clearly evident however as to the percentage of the events that were purely background, prompting a study of the kaon events to background.

A futher analysis of calculating the signal to background ratio for each method of particle identification was undertaken. The procedure involved fitting the generated kaon mass spectra by a double gaussian function, and determining the integral of total fitted events. The use of the double gaussian function should include the true kaon events and the background. The integral of the estimated background countribution in the spectra was also generated from the double gaussian fit. Hence, the true kaon yield was then calculated as the difference between the integral of fitted events obtained from the double gaussian, which provided kaon and background strengths. This allowed for a greater determination of the applicability of the PID approach, and also helped to resolve issues as to the loss of important events which resulted from the statistical reduction from a hard cut. The details of this fitting procedure are shown in the appendices. Table 8 lists the results of the total fitted, kaon, and background events, as well as the kaon events to background ratio, along with associated uncertainties for the four groups of runs analyzed.

Table 8: Sigal to background ratio.

| PID Cut Method	Total Fit Events	Background Events	Kaon Events	Signal / Background
group 1				
p (wide mass)	751.059 $\pm$ 27.405	661.559 $\pm$ 25.7207	89.500 $\pm$ 9.461	0.135 $\pm$ 0.015
β (narrow)	749.010 $\pm$ 27.368	651.976 $\pm$ 25.533	97.033 $\pm$ 9.851	0.148 $\pm$ 0.016
dE/dx	341.526 $\pm$ 18.480	294.008 $\pm$ 17.1466	47.518 $\pm$ 6.893	0.161 $\pm$ 0.025
$\beta + dE/dx$	336.42 1$\pm$ 18.341	283.515 $\pm$ 16.837	52.906 $\pm$ 7.273	0.186 $\pm$ 0.027
group 2				
p (wide mass)	1401.225 $\pm$ 37.432	1370.564 $\pm$ 37.0211	30.657 $\pm$ 5.536	0.023 $\pm$ 0.004
β(narrow)	1255.170 $\pm$ 35.428	1216.911 $\pm$ 34.884	38.259 $\pm$ 6.185	0.031 $\pm$ 0.005
dE/dx	653.677 $\pm$ 25.567	640.842 $\pm$ 25.314	12.834 $\pm$ 3.582	0.019 $\pm$ 0.005
$\beta + dE/dx$	586.706 $\pm$ 24.222	565.943 $\pm$ 23.789	20.762 $\pm$ 4.556	0.036 $\pm$ 0.008
group 3				
p (wide mass)	1547.453 $\pm$ 39.337	1508.693 $\pm$ 38.841	77.683 $\pm$ 8.813	0.025 $\pm$ 0.006
β(narrow)	1412.100 $\pm$ 37.577	1363.750 $\pm$ 36.928	73.857 $\pm$ 8.594	0.034 $\pm$ 0.006
dE/dx	713.601 $\pm$ 26.713	684.024 $\pm$ 26.153	52.307 $\pm$ 7.232	0.042 $\pm$ 0.011
$\beta + dE/dx$	649.626 $\pm$ 25.487	621.807 $\pm$ 24.936	49.872 $\pm$ 7.062	0.044 $\pm$ 0.011
group 4				
p (wide mass)	1196.791 $\pm$ 34.594	1072.572 $\pm$ 32.750	98.250 $\pm$ 9.912	0.108 $\pm$ 0.009
β(narrow)	1092.831 $\pm$ 33.058	901.383 $\pm$ 30.023	90.069 $\pm$ 9.490	0.186 $\pm$ 0.011
dE/dx	571.305 $\pm$ 23.901	498.365 $\pm$ 22.324	66.972 $\pm$ 8.183	0.134 $\pm$ 0.017
$\beta + dE/dx$	519.863 $\pm$ 22.800	410.266 $\pm$ 20.255	60.765 $\pm$ 7.795	0.227 $\pm$ 0.020
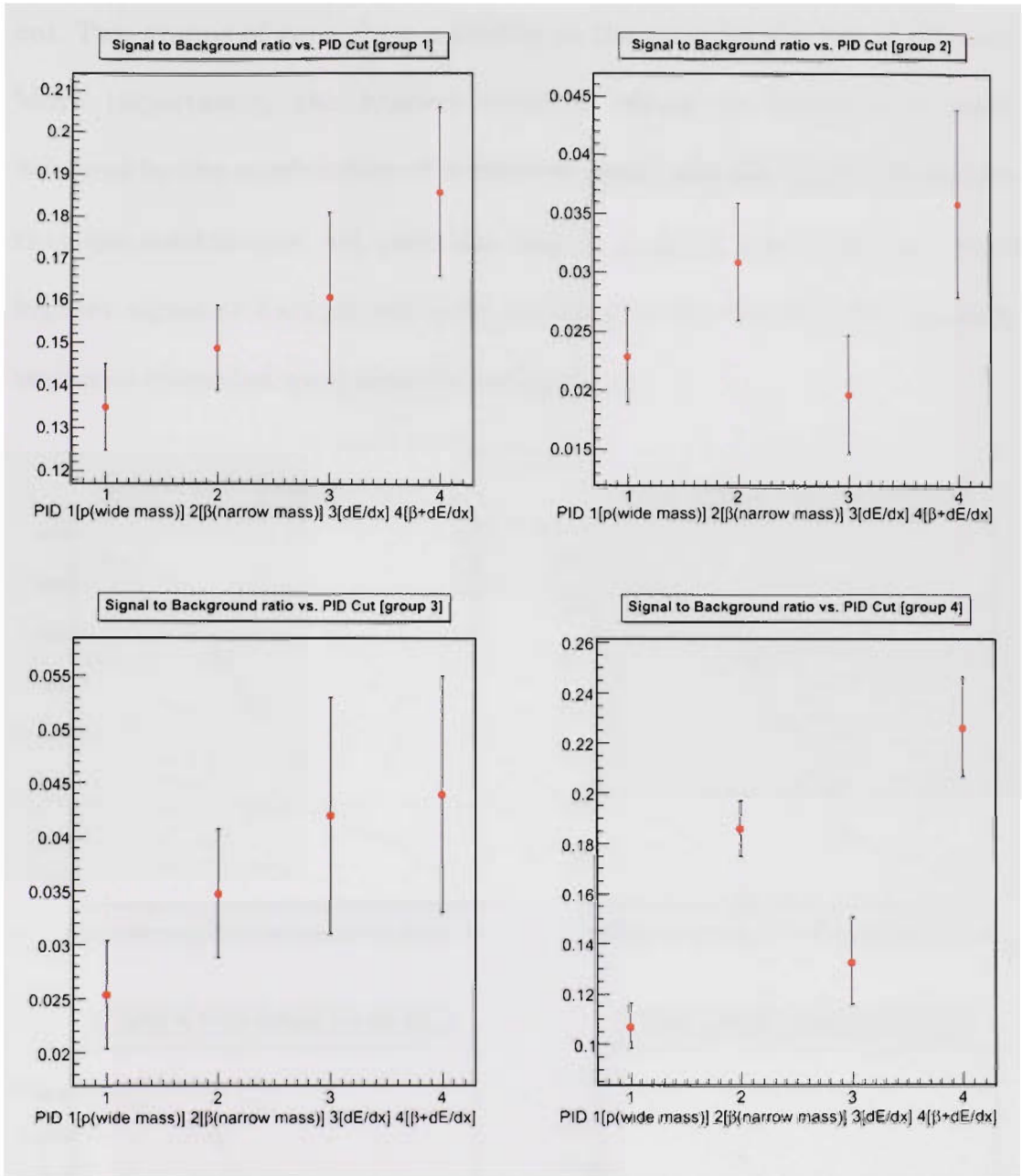
Figure 39: Signal to background ratio for indicated PID.

The signal to background ratio shown in Figure 39 corresponds directly to the groups of runs shown in Figure 38, and follows from Table 8. In all cases, the narrow mass cut, equivalent to a cut on β (narrow mass), has a larger signal to background ratio than the use of only a cut on momentum, or wide mass

cut. Two groups of runs show a decline in the ratio for the use of dE/dx cut. More importantly, the highest obtained signal to background ratio is achieved by the combination of β (narrow mass) and dE/dx cut. It was found that the combination did yield the overall greatest statictical loss, but the highest signal to background ratio, pointing to the fact that the majority of statistics discarded were actually background.
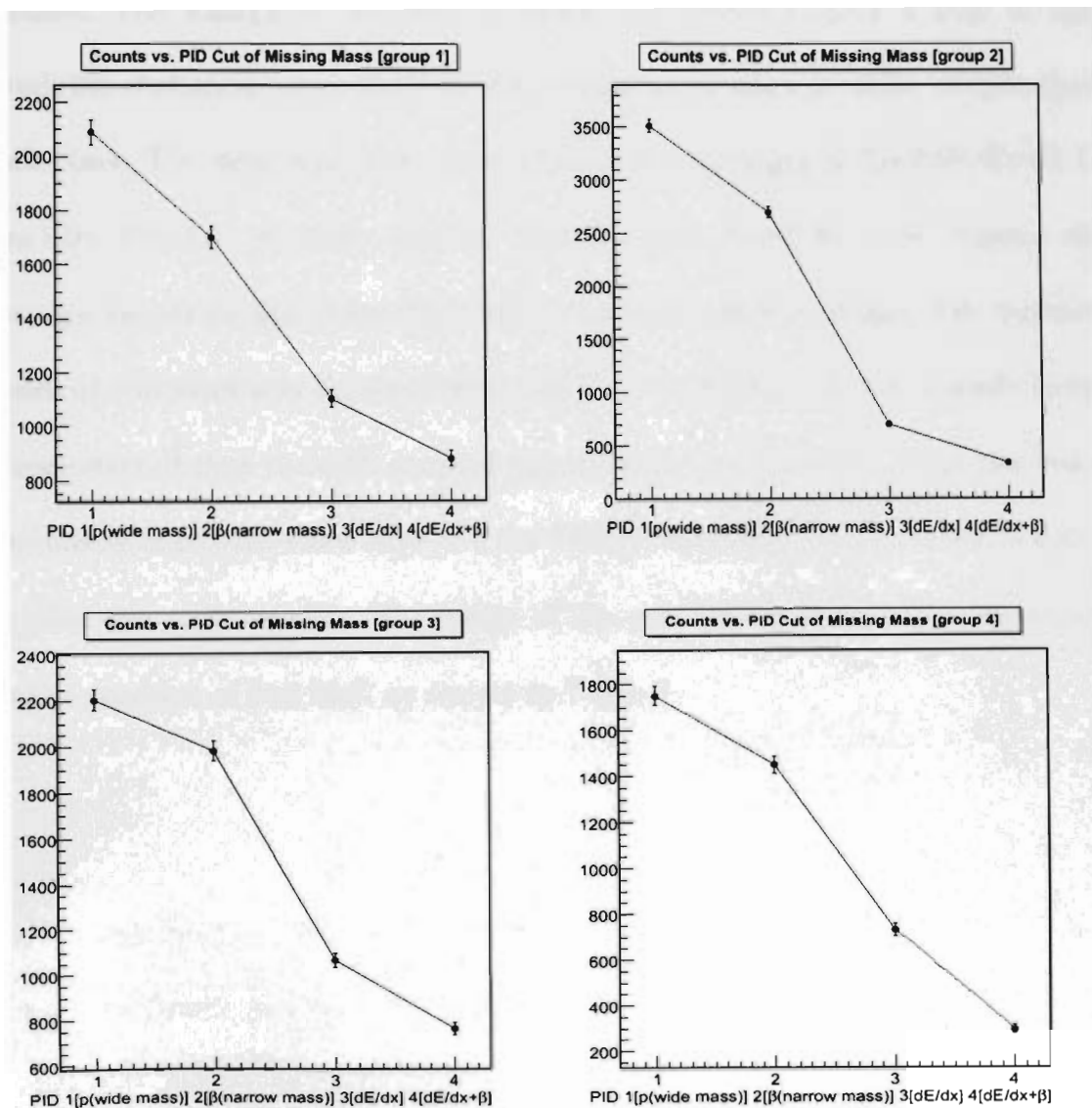

Figure 40: Missing mass entries for indicated PID technique.

The comparison was also utilized for the mising mass spectrums. The same procedure was conducted on groups of runs. The same phenomenon occurs in the spread in statistics when the use of light mass and beta cut were used, versus the dE/dx cut and flight time. This analysis verifed the large decrease in statistics with the combination of dE/dx and flight time hard cut.

The effect of the incoming photon energy range was also briefly studied. The energy of the photon beam was found to play a role in the available statistics, an indication of the number of kaon creation events that took place. The data was taken from photon beam ranges of $E\gamma_1$:$0.9 < E\gamma_1 < 1.1$, $E\gamma_2$:$1.0 < E\gamma_2 < 1.1$, $E\gamma_3$:$0.9 < E\gamma_3 < 1.0$ and $E\gamma_4$:$0.8 < E\gamma_4 < 0.95$ GeV. Figure 41 conveys events for the same PID, but for different photon ranges. The highest residual statistics was resolved from the $E\gamma_1$:$0.9 < E\gamma_1 < 1.1$. It has already been demonstrated that the PID method has an effect on statistics, thus the least amount of statistics were expected for PID (3) and PID (4). $E\gamma_2$ and $E\gamma_3$ seem to yield the same results. The range of $E\gamma_4$ was chosen due to the threshold for the reaction of 915 MeV as shown in Table 3.
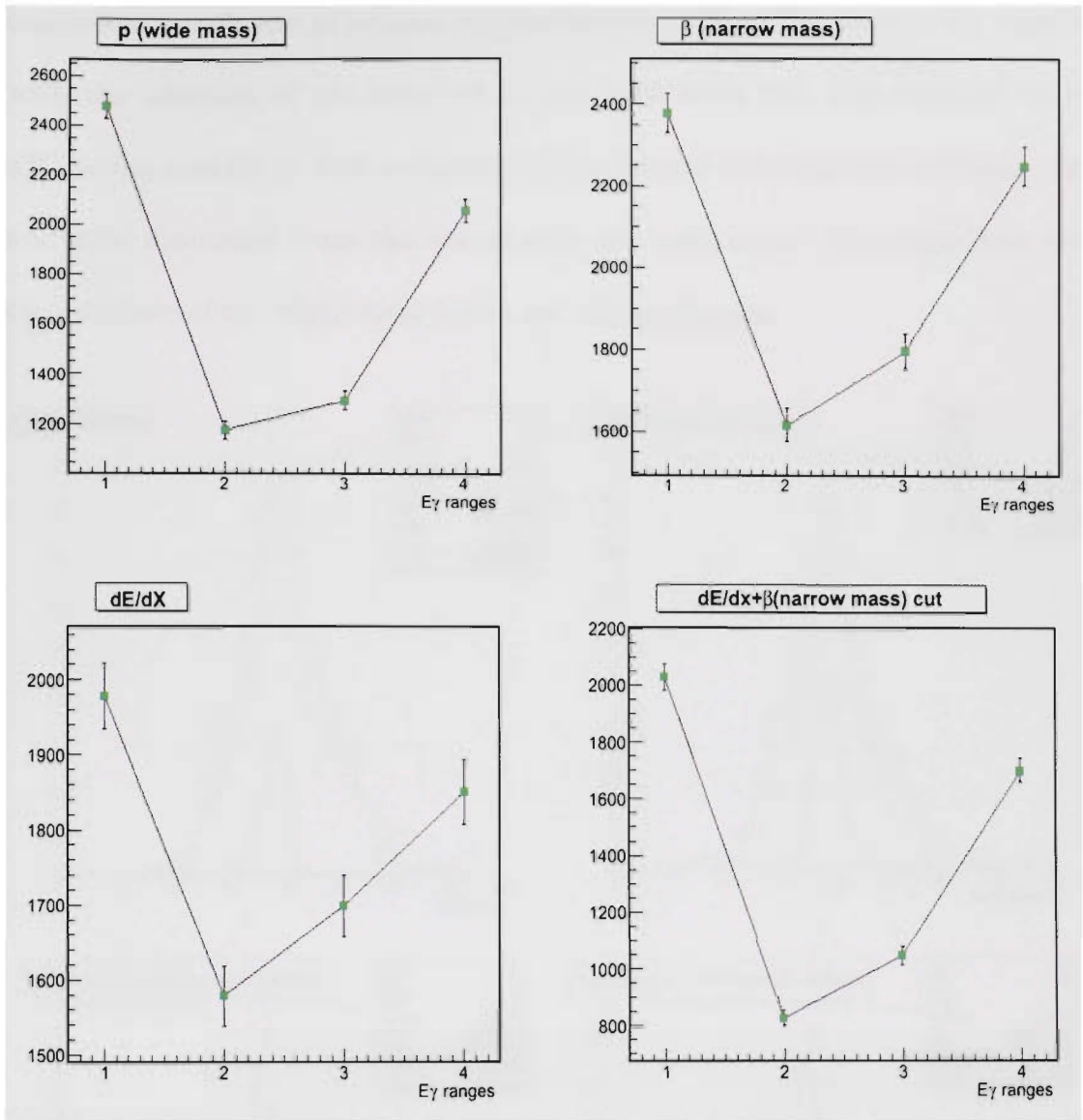
Figure 41: $\pi^+\pi^-$ invariant mass events in gamma ranges for varying PID technique.

It was verified that the combination of β and dE/dx resulted in the greatest loss in statistics, but the least background in the distribution. To reaffirm the statistical impact of hard cuts, each was placed in combination with the previous. The Figures 42 and 43 conveys the loss as each cut is added in

conjunction with the previous. Approximately 10% of the events are rejected with the addition of the beta cut to the light mass cut. The addition of the dE/dx cut results in 53% reduction of the events left from the previous cuts, and 42% discarded from the use of only the light mass. The slight loss with the addition of the flight time cut is not of significance.
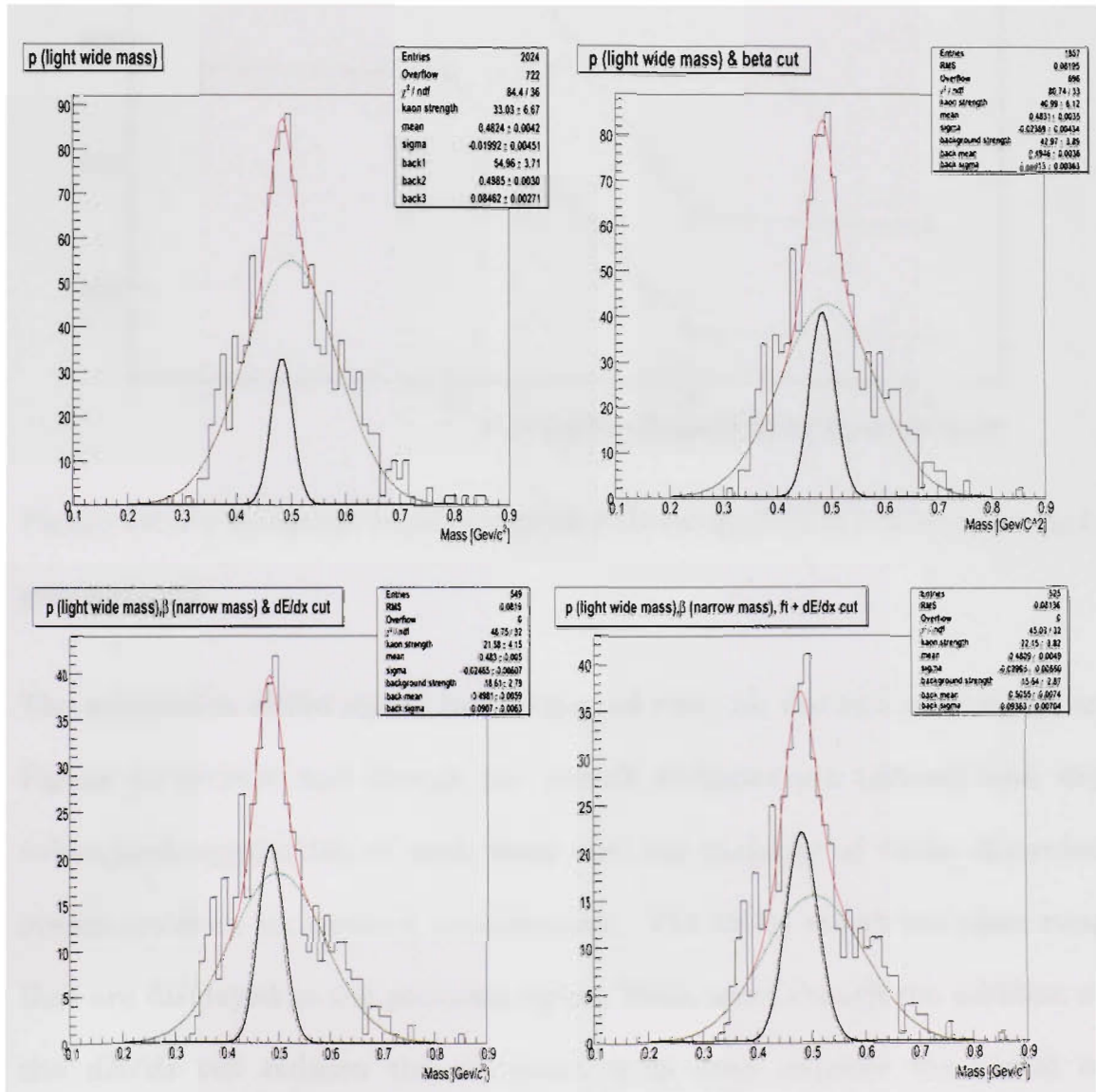

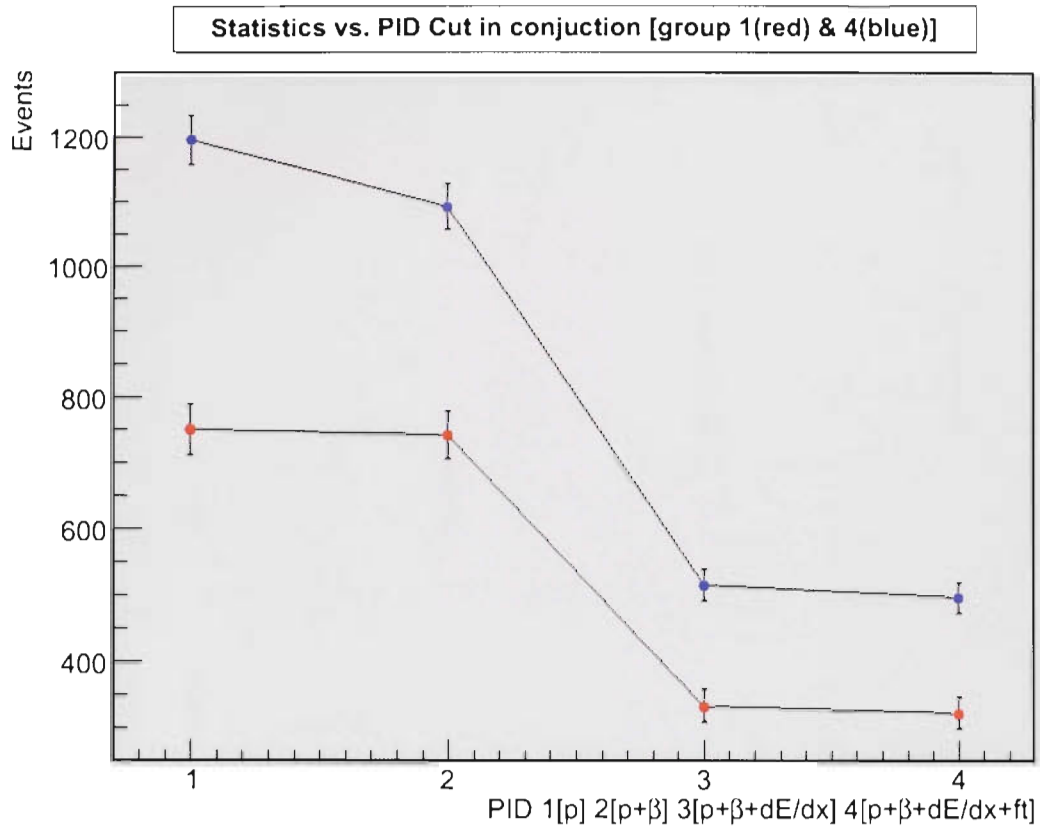Figure 42: Counts vs. mass for indicated cuts in combination

Figure 43: $\pi^+\pi^-$ invariant mass events vs. PID cut applied in combination on 2 grouped runs

The calculation of the signal to background ratio for the two runs shown in Figure 44 reveals that though the overall statistics are reduced with the subsequent application of each hard cut, the majority of these discarded events are from background contributions. The colors reflect the same runs that are displayed in the previous figure. Thus, even though the addition of the dE/dx cut reduces the statistics, it is does improve the signal to background ratio of kaon events resolved.
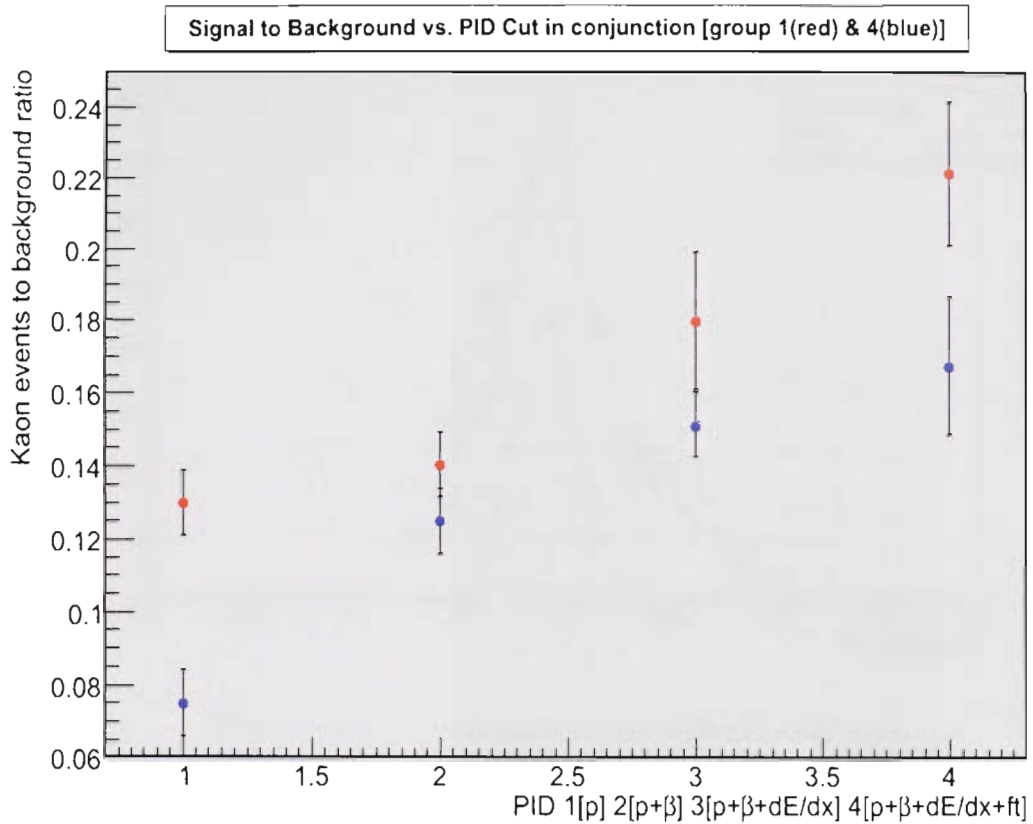
Figure 44: Signal to background ratio for indicated PID combinations on 2 grouped runs

Lastly, in the missing mass there was a tail that could be attributed to background of incorrectly identified events, or calibration errors. This is an indication that PID techniques should be incorporated simultaneously, in order to reduce the background. Figures 45 and 46 shows the invariant and missing mass with the combination of all hard cuts, light mass, dE/dx, beta, and flight time, again pointing to the resolution of the techniques applied simultaneously.
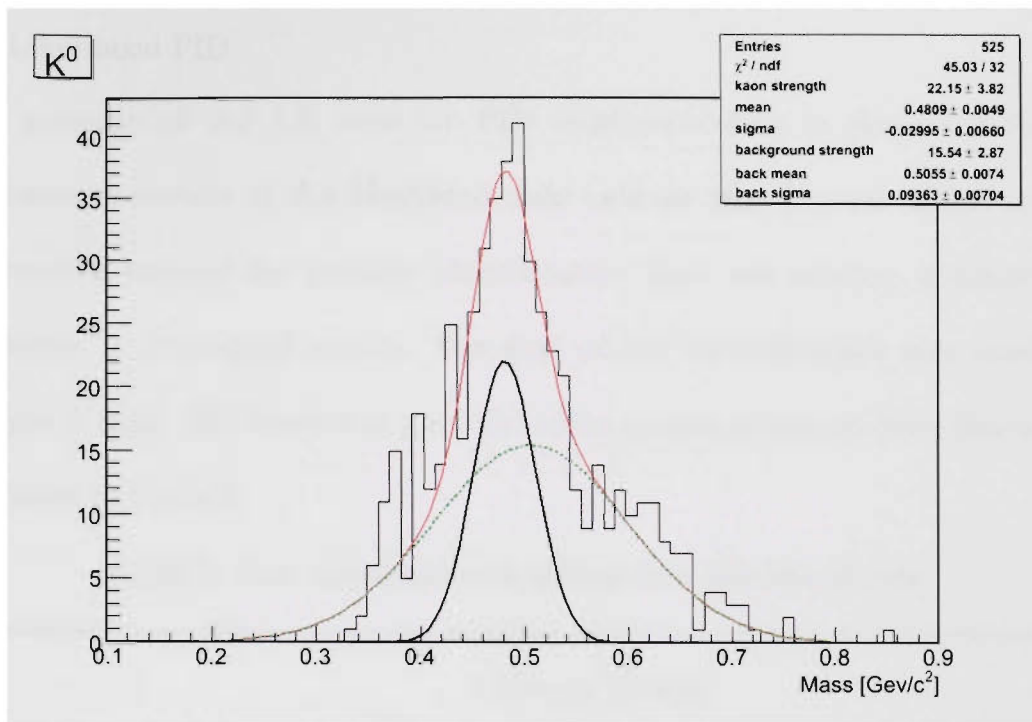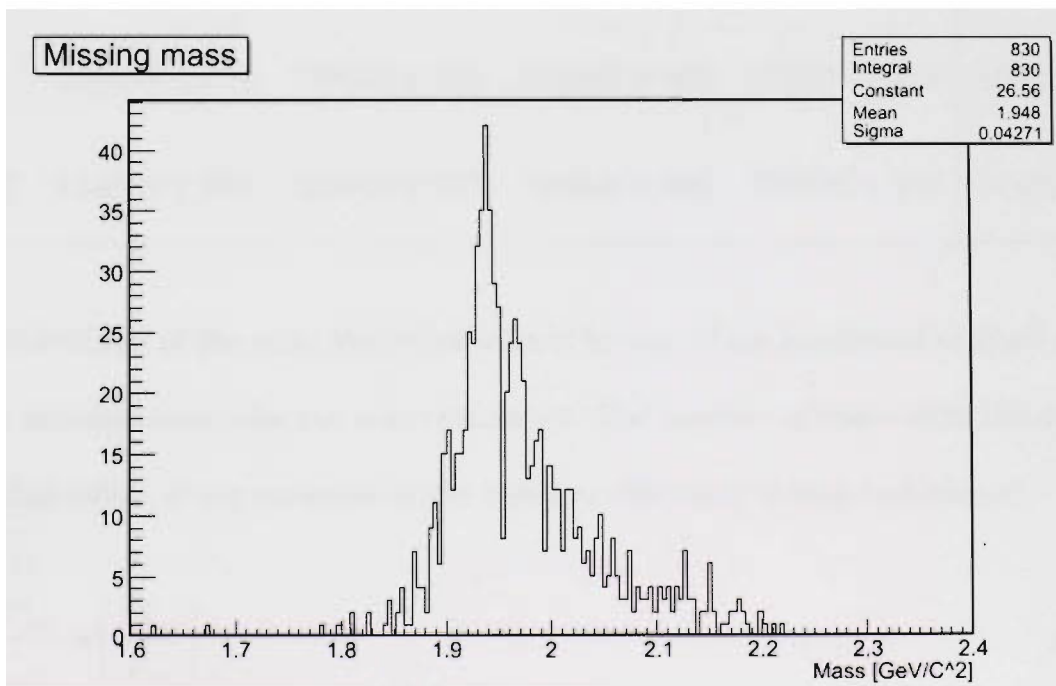
Figure 45: K^0 invariant mass with all hard cuts

Figure 46: Missing mass (Λp) from grouped runs with all hard PID cuts and a cut on kaon mass.

8.2. Likelihood PID

The outcome of the LE code for PID implementation is presented here. Preliminary results of the likelihood code indicate that the use of LE as an alternative method for particle identification does not produce a dramatic difference in statistical results. The first of the two LE codes was used to analyze 4 runs. The results of pion-identified events produced from this code are listed in Table 9.

Table 9: Pion identified events from first likelihood code

PID	π Events Yielded				
	1	2	3	4	Av.
β	163997 ± 404	140635 ± 375	159462 ± 399	172867 ± 415	159227 ± 798
LE	154534 ± 393	126400 ± 251	143666 ± 268	155392 ± 278	144998 ± 606

The average of the pion identified events by use of the likelihood method and the conventional beta cut was calculated. The number of interest is the ratio of this value, it is a measure of the relative efficiency of both techniques.

$$\frac{LE^{\pi}_{yield}}{\beta^{\pi}_{yield}} = \left(\frac{LE_{av}}{\beta_{av}} \right) \tag{33}$$

The associated error on this value is determined by,

$$\delta \frac{LE_{yield}^{\pi}}{\beta_{yield}^{\pi}} = \sqrt{\left(\frac{\partial}{\partial LE}\left(\frac{LE_{av}}{\beta_{av}}\right) \cdot \delta LE_{av}\right)^2 + \left(\frac{\partial}{\partial \beta}\left(\frac{LE_{av}}{\beta_{av}}\right) \cdot \delta \beta_{av}\right)^2} \,, \tag{34}$$

thus the ratio is

$$\frac{LE_{yield}^{\pi}}{\beta_{yield}^{\pi}} = \left(\frac{LE_{av}}{\beta_{av}}\right) = \frac{144998}{159227} = 0.910 \pm .003 \,. \tag{35}$$

The value of 0.910 implies that the conventional method would provide more pion events. However, the time of flight and energy deposition distribution from which the mean, most probable value, and sigmas were obtained were not more restrictive than normal efficient PID. It is believed that implementing these restrictions would have generated more background free distributions. Hence, the result of 0.91 is a promising result, pointing towards the obtainment of a ratio above 1.0 with these more precise restrictions.

The secondary code that was written was found to have a long processing time. It was decided to place a limit on the amount of events that was being analyzed at a time. The results of this method are listed in Table 10. A plot of pion-identified events versus the events available was created. The plots were fitted to a first order polynomial and the slope obtained. From the known slopes, the values of the pion identified events for all the events in the run can be approximated enabling calculation of the ratio of the total events identified as pion by the traditional and LE PID methods.

Table 10. Pion-identified events from second likelihood code

| Event Limit	π Events β PID	π Events LE PID
500	50 ± 7.07	34 ± 5.83
1000	117 ± 10.81	94 ± 9.69
2000	171 ± 13.07	272 ± 16.49
3000	186 ± 13.63	292 ± 17.08
4000	190 ± 13.78	298 ± 17.26
5000	191 ± 13.82	300 ± 17.32
6000	195 ± 13.96	302 ± 17.37
8000	206 ± 14.35	312 ± 17.66
9000	208 ± 14.42	392 ± 19.79
10000	214 ± 14.62	400 ± 20.00
15000	324 ± 18.00	500 ± 22.36
20000	711 ± 26.66	632 ± 25.13
30000	1266 ± 35.58	1038 ± 32.21
40000	1759 ± 41.94	1376 ± 37.09
50000	2224 ± 47.15	1744 ± 41.76
70000	3341 ± 57.80	2956 ± 54.36
90000	4414 ± 66.43	5178 ± 71.95
125000	6367 ± 79.79	6000 ± 77.45
150000	7483 ± 86.50	7436 ± 86.23
200000	10305 ± 101.51	9370 ± 96.79
250000	13040 ± 114.19	10356 ± 101.76
300000	19765 ± 140.58	16754 ± 129.43
350000	20673 ± 143.78	17040 ± 130.53
400000	25115 ± 158.47	23435 ± 153.08
450000	31654 ± 177.91	26373 ± 162.39
500000	41978 ± 204.88	32546 ± 180.40
600000	44547 ± 211.06	35980 ± 189.68
700000	48765 ± 220.82	45768 ± 213.93
1000000	70577 ± 265.66	66788 ± 258.43
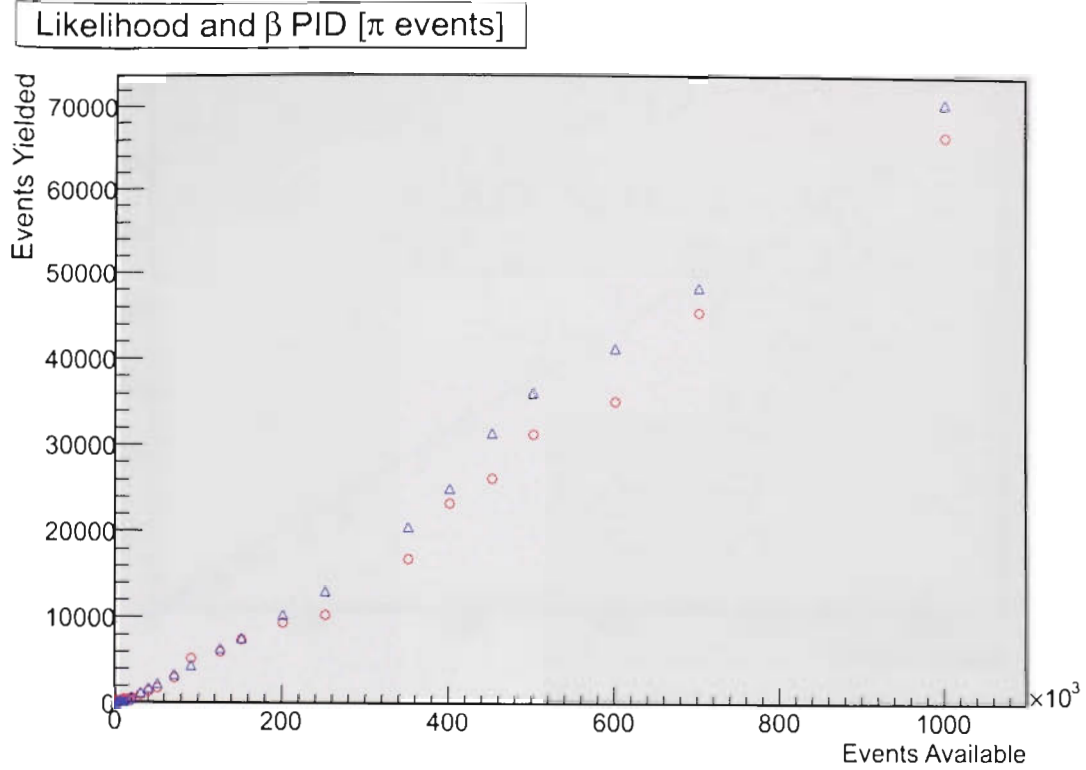
Figure 47: The pion-identified events of beta and LE PID from LE code 2

In Figure 47 the results in Table 10 are plotted, the β cut results are the blue triangles, and the LE results are depicted as red circles. The fits of pion events that were achieved via the use of a β cut and by the likelihood approach as the PID techniques are illustrated in Figures 48 and 49. The slopes obtained were $\frac{\Delta y_{\beta cut}}{\Delta x_{\beta cut}} = 0.0328$ and $\frac{\Delta y_{LE}}{\Delta x_{LE}} = 0.05619$ for the β cut and by the likelihood method respectively. The ratio of the extrapolated pion yield for 1.5×10^6 events, the total number of events in the run, was calculated to be as follows. $\frac{84281(events)}{94776(events)} = 0.89 \pm 0.05$
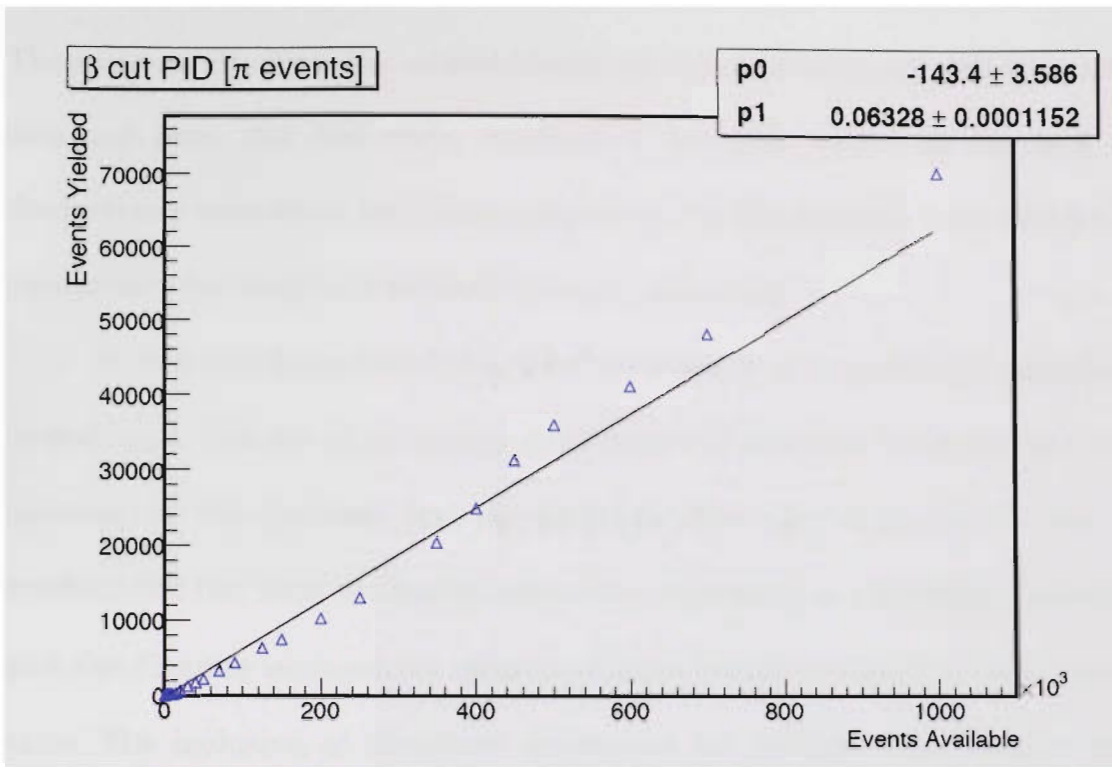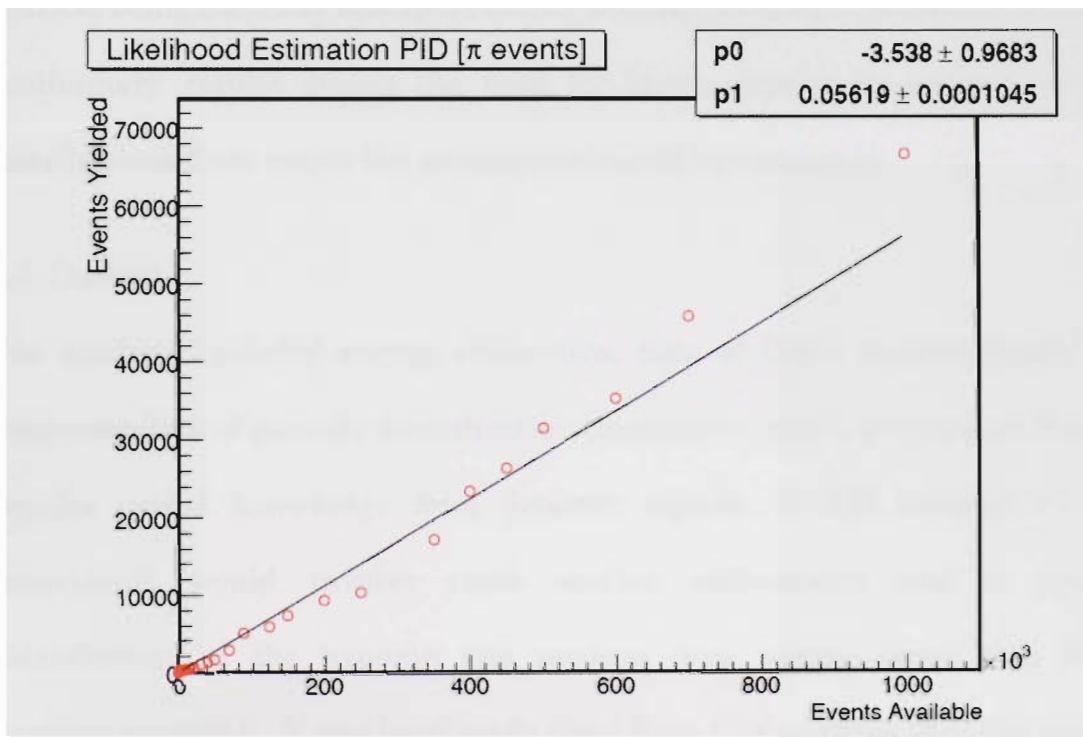
Figure 48: Pion identified events for β PID

Figure 49: Pion identified events for LE PID

The ratio results from the second likelihood code is consistent with the value obtained from the first code, however it too falls victim to the lack of distinctively restrictive limitations placed on the distributions from which the parameters for likelihood probabilities are calculated.

It has also been found that hard cuts result in a significant reduction in statistics. The use of an energy deposition cut as a lone tactic has the end outcome of the greatest loss of statistics. The use of the hard cuts in combination has been verified to reduce the ambiguity in a particle's identity, and significantly increase the number of kaon events in signal to background ratio. The inclusion of likelihood estimation for particle identification was also investigated, and preliminary results discussed. The probability of a particle being correctly identified can be accomplished by this method and the preliminary results denote the need for highly precise limitations on the distributions from which the parameters would be extracted.

8.3. Outlook

The analysis included energy calibration, time of flight measurements, an understanding of particle identification procedures, and a grasping of how to acquire useful knowledge from detector signals. A full analysis of the experiment would involve cross section calculations and a proper identification of the hyperon and nucleon final states, along with their coupling constant. It has been made clear from this analysis that the ability

to properly identify pions is well within the capabilities of any of the PID techniques discussed, but the background evident in the mass spectrums points to the need for a higher level of proton identification required to identify the lambda decay. The final state of the photoproduction process is of high interest because of the physics involved in the hyperon-nucleon interaction. Furthermore, the underlying importance of the strangeness physics was discussed, as it plays a fundamental role in understanding the structure of the matter. A continued investigation into the photoproduction process on a deuteron involving cross section calculations is likely the focus of my Ph.D. thesis.
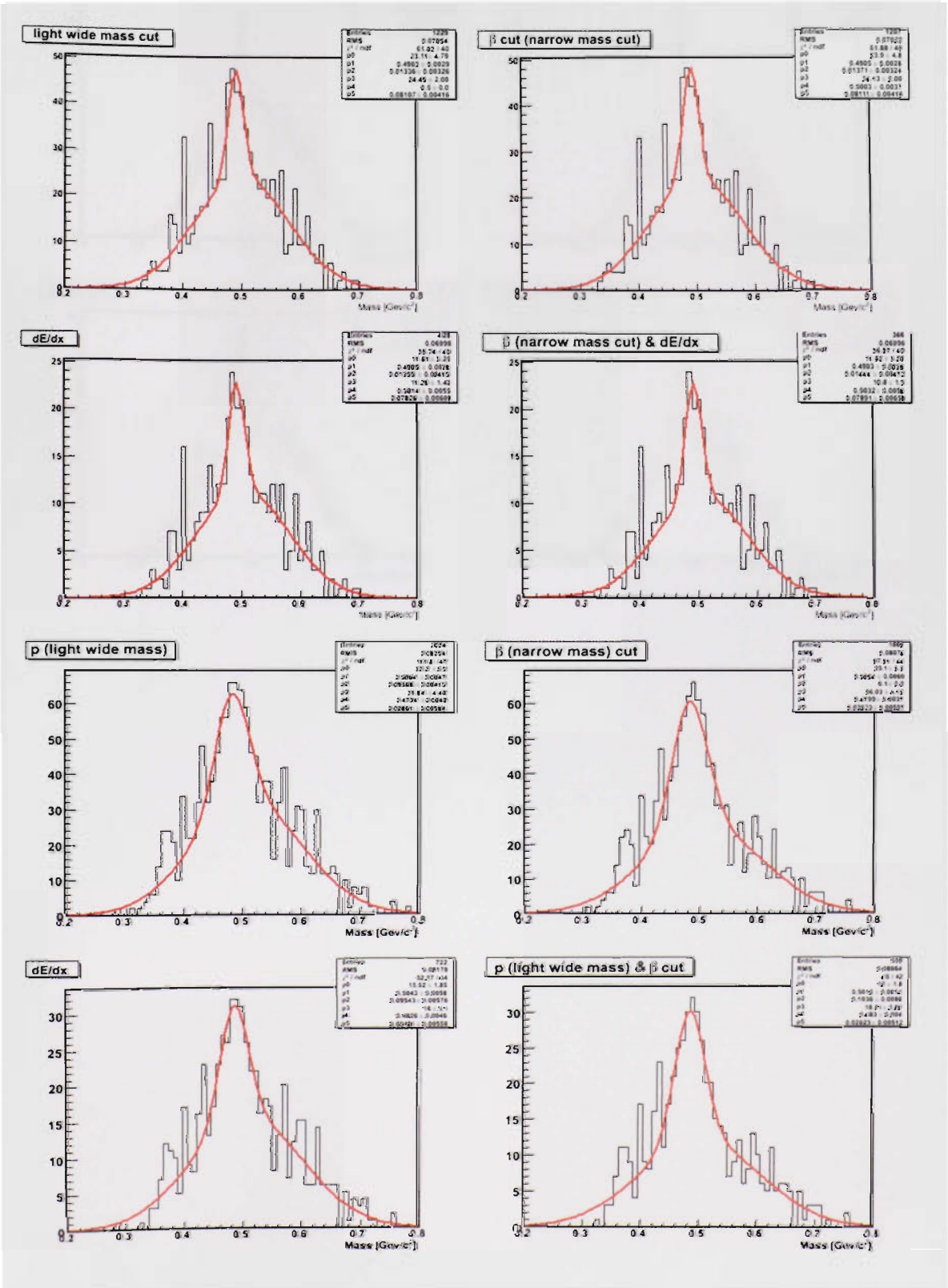
REFERENCES

[1] M. Gell-Man, "A Schematic model of baryons and mesons," Phys. Lett. **8** (1964) 215.

[2] R.P. Feynman, "High Energy Collisions," Phys. Rev. Lett. **23** (1969) 1415.

[3] T. Yan, "The Parton Model," Annual Rev. Sci. **26** (1976) 199-238.

[4] B. Povh *et al.,* Particles and Nuclei, 4th Edition (Springer-Verlag 2004).

[5] K. Tsukada *et al.*, Research Report of LNS, Tohoku University **38** (2005) 1.

[6] I. Hleiqawi, PH.D. Thesis, "K^0 Photoproduction and Electroproduction measured at CLAS," (Ohio University 2006).

[7] T. Mart, S. Sumowidagdo, D. Kusno, C. Bennhold, and H. Haberzettl, nucle-th/ 0008001 (2000).

[8] O. Maxwell, "Model Dependence in the Photoproduction of kaons from protons and deuterons," Phys. Rev. **C 70** 044612 (2004).

[9] T. Takahashi *et al.,* "Photoproduction of Neutral Kaons at LNS," Electrophotoproduction of Strangeness on nucleons and nuclei Sendai03, **198,** World Scientific Publishing Co. Pte. Ltd. (2003).

[10] T. Watanabe. *et al.,* "Photoproduction of neutral kaons on ^{12}C in the threshold region," Nucl. Phys. A. Vol. **721** (2003) 991.

[11] P. Bydzovsky, M. Sotona , O. Hashimoto, T. Takahashi , Kaon photoproduction on nucleon and deuteron. nucl-th/0412035v1 (2004).

[12] R. Nasseripour, PH.D. Thesis, "Measurement of single spin asymmetry and fifth structure function for the p(e,e'K+)Λ reaction with CEBAF large-scale acceptance spectrometer (CLAS)," (Florida International University 2004).

[13] F. X. Lee, T. Mart, C. Benhold, H. Harberzettl, L.E. Wright, "Quasifree kaon Photoproduction on nuclei," Nucl. Phys **A 695**, 237 (2001).
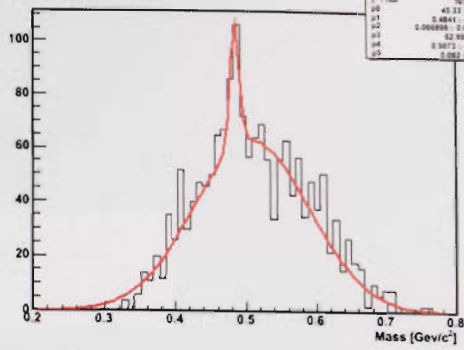
[14] R.M. Davidson and R. Workman. "Constraints on background contributions from $K^+\Lambda$ electroproduction," Phys. Rev. **C 67**, 052201 (2003).

[15] S. Mandelstam, "Determination of the Pion-Nucleon Scattering Amplitude from Dispersion Relations and Unitarity," Phys. Rev. **112** (1958) 1344.

[16] B. Carnahan PH.D. Thesis, "Strangeness Photoproduction in the $\gamma p \rightarrow K^0\Sigma^+$ Reaction," (The Catholic University of America 2003).

[17] A. Salam, K.Miyagawa, T.Mart, C. Bennhold, and. W.Glocke, "K^0 photoproduction on deuteron and the extraction of the elementary amplitude." nucl-th/0608053v1 (2006).

[18] C. Grupen, "Physics of Particle Detection," Instrumentation in Elementary Particle Physics, VII ICFA School, Istanbul, Turkey (1999).

[19] E. Nappi, "Charged Particle Identification via Ionization Energy Loss and Time-of-Flight Measurements," I ICFA School, Morelia Mexico.

[20] W.R. Leo "Techniques for Nuclear and Particle Physics Experiments," Springer-Verlag Berlin Heidelberg 1994.

[21] M. Sheaff , "Detectors for Particle Identification Time-of-Flight, dE/dx, and Transition Radiation," CP **536** Instrumentation in Elementary Particle Physics: VIII ICFA School.

[22] M. Hauschild, "Progress in dE/dx techniques used for particle identification, Nuclear Instrumentation & Methods in Physics Research," A **379** (1996) 436-441.

[23] H. Bischel et al., "Passage of Particles through matter," Phys. Lett B, **592** (2004) .

[24] L.D. Landau , J. Exp. Phys (USSR) 8 (1944) 201.

[25] C. Henderson, PH.D. Thesis, "Identified Particle Transverse Momentum Distribution from Au+Au Collisions at 62.4 GeV per Nucleon Pair," (Massachusetts Institute of Technology 2005).

[26] M.T. Rownan, "Particle Detectors," Phys. Lett. B, **592** (2004) 261.

[27] K. Futatsugawa, M.S.Thesis. (Tohoku University 2006).

[28] K. Tsukada, PH.D. Thesis, "Photoproduction of neutral Kaons on deuterons near the threshold region," (Tohoku University 2005) .

[29] Laboratory of Nuclear Science March 2007 Pamphlet.
http://www.LNS.tohoku.ac.jp.

[30] K. Tsukada *et al.,* "Photoproduction of neutral Kaons on the liquid deuterium target in threshold region," Phys Rev C **78**, 014001 (2008)

[31] T. Kawasaki Power-point presentation.
Tohoku University Experimental Nuclear Strangeness Group collaboration Meeting June 3, 2006 (private communication)

[32] S. Shende, PH.D Thesis, "Strangeness Photoproduction on the Deuteron Target," Academic Press Europe-Groningen 2007.

[33] http://en.wikipedia.org/wiki/image:photomultipliertube.svg

[34] G.E. Barwell, "On Certain Characteristics of Some Discrete Distributions," (Biometrika, 1960).